IN SITU TRIBOCHEMICAL CHARACTERIZATION OF NANOLUBRICANTS

A Dissertation

by

YAN CHEN

Submitted to the Graduate and Professional School of
Texas A&M University
in partial fulfillment of the requirements for the degree of

DOCTOR OF PHILOSOPHY

Chair of Committee,	Hong Liang
Committee Members,	Andreas A. Polycarpou
	Miladin Radovic
	Terry Creasy
Head of Department,	Ibrahim Karaman

August 2021

Major Subject: Materials Science and Engineering

ABSTRACT

Lubrication plays important roles in mechanical systems in motion. The challenge in understanding the characteristics of a lubricant under working conditions lies in its dynamic nature, and it is impossible to observe the target directly. The objective of this thesis research is to obtain better fundamental understanding of nanolubricants under shear. Specifically, a methodology that enables *in situ* detection of a rubbing pair is developed. Using this approach, the properties and performance of nanoluricants are studied. The resulting tribochemical products as tribofilms are investigated.

This research consists investigation in three aspects. The first is to develop *in situ* tribo-electrochemical techniques enabling basic study. An integrated tribotesting system combined a disc-on-disc tribotesting with electrochemical impedance measurement.

The second is to study the properties of working lubricants, their electrical and thermal properties. The electrical conductivity against the oil film thickness was examined. Results showed the non-ohmic behavior of a lubricating film in the hydrodynamic regime. Properties of lubricants and testing conditions are some of the factors affecting the conductivity. The study on thermal performance over a mineral oil and polyalphaolefin (PAO) were carried out. Results showed that thermal properties of lubricants depended on the shear and they were not constants as being known. This research revealed the potential existence of dynamic properties of a working lubricant.

The third is to investigate tribochemical interactions between nanolubricants and rubbing surfaces of a substrate. Using α-ZrP nanoparticles as additives, a nanolubricant produced a tribofilm with consistent electrical properties that reduced friction for 40% and wear 90%. Research results showed that under shear, a tribofilm consisting of pyrophosphate.

DEDICATION

To my family and friends.

ACKNOWLEDGEMENTS

I would like to thank my committee chair, Dr. Liang, and my committee members, Dr. Polycarpou, Dr. Radovic, Dr. Creasy, for their guidance and support throughout the course of this research. I would also like to thank Dr. Clearfield, Dr. Simon and Dr. Opperman for their kind help.

Thanks also go to my friends and colleagues and the department faculty and staff. I enjoyed the time at Texas A&M University because your kindness and help.

Thanks to my mother and father for their encouragement and my fiancée for her love.

Finally, thanks to my emotional supporting animal, Francesca, who firmly supported my emotion in this journey.

CONTRIBUTORS AND FUNDING SOURCES

Contributors

This work was supervised by a thesis (or) dissertation committee consisting of Professor Hong Liang, Professor Miladin Radovic, Professor Terry creasy of the Department of Materials Science and Engineering and Professor Andreas A. Polycarpou, of the Department of Mechanical engineering.

Part of the data analysis in Chapter III was provided by Dr. Mojdeh Rasoulzadeh of the department of mathematics in University of Alabama. The amphiphilic nanoparticles in Chapter V were provided by Xuezheng Wang of the department of chemical engineering. The Raman characterization in Chapter V was provided by Zehua Han of the Department of Physics. The Raman characterization in Chapter VI was provided by Alexander Sinyukov of the Department of Physics. The dog teeth in Chapter VI were provided by Bradley T. Simon of Small Animal Clinical Sciences.

All other work conducted for the thesis (or) dissertation was completed by the student independently.

Funding Sources

Graduate study was partly supported by T3 president's excellence fund. This work was also made possible in part by TTRF foundation.

TABLE OF CONTENTS

CHAPTER V TRIBOCHEMICAL INTERACTIONS IN NANOLUBRICANTS.........95

CHAPTER VI APPLICATIONS 123

CHAPTER VII CONCLUSION AND FUTURE RECOMMENDATION..................156

LIST OF FIGURES

Page

LIST OF TABLES

Page

CHAPTER I

INTRODUCTION [1]

In this chapter, the background information related to this research was introduced to better understand the subject matter. It consisted of three related parts. The first discussed the definition and applications of nanolubricants. The second focused on challenges of nanolubricants, such as the dispersion of nanoparticles and issues related to application. The third introduced the testing methods for tribological, electrical and thermal properties.

1.1 Nanolubricants

In mechanical systems, frictional loss is a factor in energy loss [1]. To reduce friction and wear, nanoparticles(NPs) have been studied and used as lubricant additives that have promising effects on friction and wear reduction in automotive[2,3], mining[4], and other industrial applications [5]. These lubricant with nanoparticle additives were called nanolubricants. We have recently reported that in the boundary lubrication region, the addition of nanoparticles can reduce friction coefficient for up to 70%, and wear volume for as high as 75%[5]. Nanoparticles of various compositions and sizes have

---

[1] Part of this chapter is reprinted with permission from "Dispersion of nanoparticles in lubricating oil: A critical review." By Chen, Yan, Peter Renner, and Hong Liang. Lubricants 7, no. 1 (2019): 7. MDPI; Part of this chapter is also reprinted with permission "Performance Characteristics of Lubricants in Electric and Hybrid Vehicles: A Review of Current and Future Needs. " By from Chen, Y., S. Jha, A. Raut, W. Zhang, and H. Liang. Front. Mech. Eng 6 (2020): 571464.

demonstrated certain degrees friction modifying and anti-wear effects. In our collection of recent papers, the majority of particles of sizes reported were 10-100nm (Figure I.1).

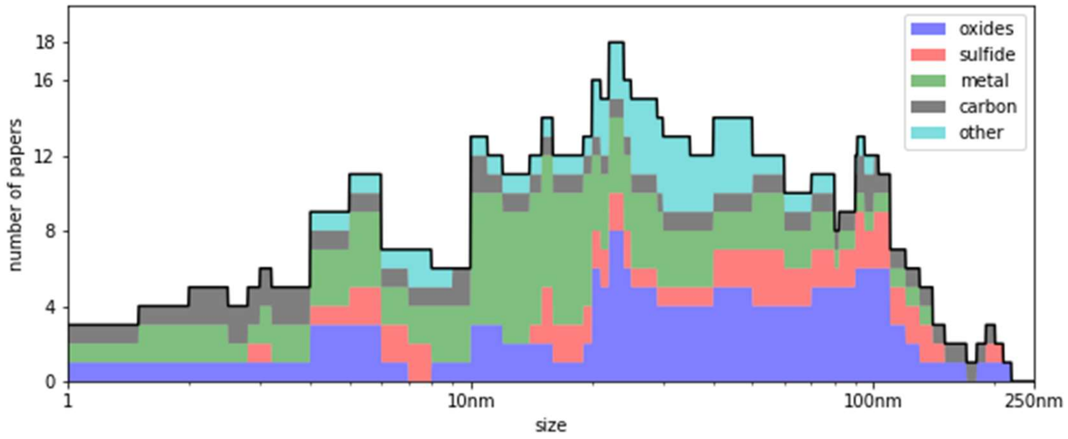

Figure I.1 The material and size of nanoparticles surveyed in this Chapter.

Nanoparticles of various compositions and sizes have demonstrated certain degrees of friction modifying and anti-wear effects. In the boundary lubrication region, the addition of α-ZrP nanoparticles reduce the friction coefficient up to 70%, and wear volume as high as 75% [1]. Such lubricants consisting of a base oil and dispersed nanoparticles emerged as a new class of nanolubricants [1,2]. α-ZrP functioned as a lubricant additive because it can generate a protective iron phosphate film through tribochemical reactions[1]. Such protective film was called a tribofilm[3,4].

Like other additives, the NPs can be adsorbed on the contacting surfaces. This adsorption is driven by Van der Waals's interactions between the NPs and the surfaces[1,5]. In some cases the adsorption of NPs can directly reduce the friction in the boundary lubrication regime and protect the surfaces from contacting[6,7]. However, with the tribochemical reactions the NP additive can have better tribological performance.

For some NPs such as metal oxides NP, there are no tribochemical "reactions" because the composition of the tribofilm they form has the same composition as the NPs. They are essentially sintered to the contacting surfaces by the tribological process[8–15]. There is also a report on tribochemically active oxide NPs such as Fe_3O_4. The metal elements can be reduced and/or oxidized via tribochemical reactions[16,17]. This oxidation reaction promoted by the oxide nanoparticles is essential to the chemical-mechanical polishing process[18–22]. In these reactions, the nanoparticle tribochemical reactions chemically wears the surface instead of protecting it. The overbased detergents are NP lubricant additives that can effectively reduce wear by forming a tribofilm[23,24]. This NP is also tribochemically inactive. The formation of its tribofilm is mechanical rather than chemical[24]. The capped metal NPs can reduce wear and friction without tribofilm formation[25]. In some cases such as copper NPs[26] and silver NPs[27] the tribofilm can form directly by mechanical cold welding. One exception to the capped metallic NPs is the dodecanethiol-modified Palladium NPs. The dodecanetiol capped Palladium forms palladium sulfide on the contacted surface when used as a lubricant additive[28]. The rare earth-containing nanoparticles can form iron oxide tribofilms through the oxidation-catalysis effect[29].

One of the most successful NP friction modifying additives, inorganic fullerene molybdenum disulfide (IF-MoS_2) has its friction modifying ability due to its tribochemical reactions. MoS_2 is known to be a solid lubricant as a powder or additive[30]. Under tribological forces, the IF-MoS_2 forms a tribofilm comprised of 2H-MoS_2 and chemically bonds to the iron oxide on the steel surface[31]. The mechanism of this reaction was proposed that the mechanical breakdown of IF-MoS_2 nanosheets can tribochemically bond to the iron/iron oxide[31]. The iron sulfide can also be found in the tribofilm formed by MoS_2 and WS_2 NPs[32,33]. The MoO_3 nanoparticles can tribochemically react with oleyfin polysulphide to form MoS_2[34,35]. The molecular dynamics simulation also shows that MoS_2 nanosheets were more stable between contacting surfaces compared to the amorphous phase [36].

For some NPs such as metal oxides NP, there are no tribochemical "reactions" because the composition of the tribofilm they form has the same composition as the NPs. They are essentially sintered to the contacting surfaces by the tribological process[8–15]. There is also a report on tribochemically active oxide NPs such as Fe_3O_4. The metal elements can be reduced and/or oxidized via tribochemical reactions[16,17]. This oxidation reaction promoted by the oxide nanoparticles is essential to the chemical-mechanical polishing process[18–22]. In these reactions, the nanoparticle tribochemical reactions chemically wears the surface instead of protecting it. The overbased detergents are NP lubricant additives that can effectively reduce wear by forming a tribofilm[23,24]. This NP is also tribochemically inactive. The formation of its tribofilm is mechanical rather than chemical[24]. The capped metal NPs can reduce wear and friction without tribofilm formation[25]. In some cases such as copper NPs[26] and silver NPs[27] the tribofilm can form directly by mechanical cold welding. One exception to the capped metallic NPs is the dodecanethiol-modified Palladium NPs. The dodecanetiol capped Palladium forms palladium sulfide on the contacted surface when used as a lubricant additive[28]. The rare earth-containing nanoparticles can form iron oxide tribofilms through the oxidation-catalysis effect[29].

One of the most successful NP friction modifying additives, inorganic fullerene molybdenum disulfide (IF-MoS_2) has its friction modifying ability due to its tribochemical reactions. MoS_2 is known to be a solid lubricant as a powder or additive[30]. Under tribological forces, the IF-MoS_2 forms a tribofilm comprised of 2H-MoS_2 and chemically bonds to the iron oxide on the steel surface[31]. The mechanism of this reaction was proposed that the mechanical breakdown of IF-MoS_2 nanosheets can tribochemically bond to the iron/iron oxide[31]. The iron sulfide can also be found in the tribofilm formed by MoS_2 and WS_2 NPs[32,33]. The MoO_3 nanoparticles can tribochemically react with oleyfin polysulphide to form MoS_2[34,35]. The molecular dynamics simulation also shows that MoS_2 nanosheets were more stable between contacting surfaces compared to the amorphous phase [36].

1.2 Challenge of Nanolubricnat

1.2.1 Dispersion of nanolubricant

Stable suspension of nanoparticles is essential for a usable lubricant. The key bottleneck for the application of nanolubricant remains to be the aggregation of nanoparticles in a base lubricant, due to their higher surface energy.

Stable suspension of nanoparticles is essential for a usable lubricant. The aggregation of nanoparticles in oil limits their ability to lubricate the contact area [37]. The MoS_2

nanoparticle can reduce update 75% of friction when mixed with lubricant oil. However, such reduction of friction requires ultrasonic dispersion immediately before testing[38,39], making the dispersion more complicated. Additionally, the low friction achieved by adding nanoparticles was lost without constant stirring of the oil[39] In field applications. Thus, investigating a robust method to disperse nanoparticles in lubricant oil is in great demand.

Two strategies have been used to form stable suspension of nanoparticles in lubricant oil. One strategy was changing the formulation of the lubricant oil by incorporating a certain amount of surfactant along with nanoparticles. The other was to modify or synthesis nanoparticles with amphiphilic chemicals or alkoxysilanes. Both methods modified the surface of nanoparticles by absorption or chemical reaction to form an organic layer.

Several characteristic techniques were used to examine the quality of dispersion. The dynamic light scattering (DLC) method was used to measure the hydrodynamic radius of nanoparticles. The DLC tracks the scattering of polarized light from the sample [40] and with this information calculates the radius of the nanoparticles. The increase of hydrodynamic radius can signal the particle aggregation. Several studies used UV-visible spectroscopy to track the sample's light absorption. The decrease of optical absorption inferred the aggregation and sedimentation of nanoparticles [41]. Sedimentation method, used by most of the studies surveyed in this paper, observed the aggregation and sedimentation by visual inspection of the sample. All those methods reported a stabilization time of the nanoparticle dispersion in lubricant. The stabilization time will be further discussed in later section.

The property of nanoparticles, the dispersion method, and resulting suspension are listed in Table 1. The stable time data were retrieved from either sedimentation observation or dynamic light scattering data. Each time represents the duration of stable nanoparticles dispersed in oil. For those have long shelf life, we do not discuss about them here. Reported stable times of greater than a month in this review will be regarded as reaching long term stability. If there was no stabilizing time given or no empirical proof of long-term stabilization, the stabilization time was marked as “Claimed”. All well-dispersed nanoparticle additives were either formulated with dispersants or by using surface modified nanoparticles. The tendency of nanoparticle aggregation in hydrocarbons appears universal, no matter the material type or shape of the nanoparticles.

Table I-1 The publication researched in this paper.

Particle	Size nm	media	Disperse Method*	Stability	Stable time
Oxides					
TiO2	2	liquid paraffin	SSM.	stable	months[42]
	5	liquid paraffin	SSM.	not reported[43]	
	10	liquid paraffin	SSM.	stable	Claimed[44]
	15	PAO Spectrasyn 4	SI-ATRP	stable	56 days[45]
	23	PAO	None	aggregated[46]	
	25	liquid paraffin	Silanization + Dispersant	stable	5 months[47]
SiO2	12	PAO	NIM	stable	2 days[48]
	15	Ionic liquid	None	aggregated[49]	
	23	PAO Spectrasyn 4	SI-ATRP	stable	56 days[45]
	23	PAO	SI-ATRP	stable	60 days[50]
	25	GMO	Silanization	stable	5 months[51]
	45	EOT5	None	not reported[52]	
	60	PAO 100	Silanization	stable	2 months[53]
	100	RO base oil	Silanization	stable	8 days[54]
	110	PAO	Silanization	stable	2 months[55]
	200	PAO	Silanization	stable	4 months[56]
	200	PAO	Silanization	stable	2 months[57]
ZrO2/SiO2	100	20# mechine oil	Other	stable	12 hours[58]
Al2O3/SiO2	70	liquid paraffin	Silanization	stable	3 months[59]
CuO	5	PAO	SSM.	stable	30 days[11]
	40	PAO 6	None	not reported[12]	
ZnO/CuO	40	vegetable oil	None	not reported[60]	
ZrO2	25	PAO 6	None	not reported[12]	
ZnO	20	PAO 6	None	not reported[12]	
ZnO/Al2O3	50	20# mechine oil	SSM.	stable	28 days[61]
Fe3O4	10	liquid paraffin	SSM.	stable	Claimed[62]
Fe2O3	30	500 SN basic oil	Dispersant	Stable	Claimed[63]
Al2O3	80	20# mechine oil	SSM.	stable	20 days[64]
Al2O3/TiO2	100	base oil	Silanization	stable	110 hours[65]
GO/ZrO2	5	liquid paraffin	Other	stable	48 hours[66]

*Abbreviations: SSM. Surfactant surface modification. NIM. Nanoscale ionic materials. SI-ATRP. Surface induced atomic transfer radical polymerization.

Table 1. cont.

Particle	Size nm	media	Disperse Method*	Stability	Stable time
Sulfide					
PbS	5	liquid paraffin	SSM.	stable	Claimed[67]
IF-WS2	65	PAO	None	not reported[68]	
	100	PAO	None	stable	hours[69]
	110	liquid paraffin	Silanization	stable	14 days[70]
	120	liquid paraffin	None	aggregated[71]	
WS2	7	PAO	SSM.	stable	6months[72]
	100	liquid paraffin	SSM.	stable	Claimed[73]
	200	liquid paraffin	SSM.	stable	1 day[74]
IF-MoS2	35	PAO/Hexane	None	not reported[75]	
MoS2	3	PAG	SSM.	stable	2 weeks[32]
	15	250X base oil	Dispersant	stable	Claimed[76]
	85	EOT5	None	not reported[52]	
	90	coconut /paraffin oil	SSM.	stable	2 days[77]
MoS2/TiO2	125	rapeseed oil	None	stable	2 days[78]
CuS	20	liquid paraffin	SSM.	stable	Claimed[79]
Metal					
Cu	5	liquid paraffin	SSM.	stable	months[42]
	9	500SN base oil	SSM.	stable	Claimed[80]
	15	liquid paraffin	SSM.	stable	Claimed[81]
	40	raw oil	Dispersant	not reported[82]	
	75	500SN base oil	Dispersant	aggregated[83]	
Carbon-coated Cu	65	PAO6	None	not reported[84]	
Ni	8	PAO	SSM.	stable	1months[85]
	20	500SN base oil	Dispersant	stable	Claimed[86]
	20	PAO	None	stable	hours[87]
Ag	4	liquid paraffin	SSM.	stable	months[42]
	4	PAO	SSM.	stable	hours[27]
	10	liquid paraffin	SSM.	not reported[88]	
	15	liquid paraffin	SSM.	stable	7 days[89]
Pd	2	liquid paraffin	SSM.	stable	Claimed[90]

*Abbreviations: SSM. Surfactant surface modification. NIM. Nanoscale ionic materials. SI-ATRP. Surface induced atomic transfer radical polymerization

Table 1 cont.

Particle	Size nm	media	Disperse Method*	Stability	Stable time
Carbon					
Graphene	N/A	liquid paraffin	Dispersant	not reported[91]	
	N/A	PAO 9	SSM.	stable	Claimed[92]
	N/A	SN350	SSM.	stable	6 hours[41]
	N/A	hexadecane	SSM.	stable	2 days[93]
	N/A	PEG400	NIM	stable	30 days[94]
Fullerene	10	mineral oil	None	not reported[95]	
Carbon nano-onions	4	PAO	None	aggregated[96]	
Carbon nano-horns	97	Mobil Pegasus 1005	Dispersant	stable	14 days[97]
Carbon nanotube	100	PAO	Dispersant	stable	24 hours[98]
Other					
CaCO3	20	500SN base oil	Dispersant	not reported[99]	
	40	PAO	SSM.	stable	Claimed[100]
	45	dodecane /decane	Dispersant	stable	Claimed[101]
Zinc borate	35	500 SN basic oil	Dispersant	stable	Claimed[102]
ZnAl2O4	95	Lubricant oil	SSM.	unstable[103]	
La(OH)3	30	liquid paraffin	None	Not reported[104]	
LaB	30	500SN base oil	Dispersant	stable	Claimed[105]
LaF3	6	liquid paraffin	SSM.	stable	Claimed[106]
	8	liquid paraffin	SSM.	stable	months[42]
BN	70	POE	Silanization	stable	10 days[107]

*Abbreviations: SSM. Surfactant surface modification. NIM. Nanoscale ionic materials. SI-ATRP. Surface induced atomic transfer radical polymerization

1.2.1.1 Fomulation of nanolubricant

In early research (before 2005), the common method used to study the effects of nanoparticles in lubricant was to disperse these aforementioned nanoparticles using a dispersants [63,76,83,86,91,99,102]. The dispersants used in those research including Aliquat 336 [86], Estisol 242 [47], oleic acid [47], sorbitol monostearate [63,102], etc. These dispersants were mixed with the nanoparticles and the lubricant oil to create a stable dispersion. In some cases, multiple types of dispersants were used simultaneously [47].

The mechanism of dispersant-stabilizing nanoparticles was absorption on the surface of the nanoparticle. Those dispersants were amphiphilic molecules which had both lipophobic and lipophilic functional groups. The lipophobic part can absorb on the surface of the nanoparticle, forming an organic layer[108]. This organic layer can sterically stabilize the nanoparticles. In some cases, the addition of dispersant lowered the effectiveness of nanoparticles[109].

Among the studies where only dispersant was used, none achieved a long-time stability. The stable time was either untested or less than a few weeks. The one which reached long-time stability (5 months) used a nanoparticle with silane surface modification [47]. Furthermore, the dispersion agent also changes the formulation of lubricant oil. The mechanism of dispersant-stabilizing nanoparticles was absorption on the surface of the nanoparticles. This absorption can happen on the surface of the tribological pairs where lubricant was used. In addition, the amount of dispersant added was more than the amount of nanoparticles in this method [76,86,102,105]. Because of this, the property of nanolubricant was altered. In some cases, the addition of dispersant lowered the effectiveness of nanoparticles [109].

The above-mentioned drawbacks rendered formulation with dispersant an unideal method to disperse nanoparticles in lubricant oil. Therefore, surface modification methods were needed to form a stable nanoparticle dispersion.

1.2.1.2 Surface modification

In recent years, methods of surface modification of nanoparticles as lubricant additives have seen many improvements. Figure I.2 shows the accumulated number of papers on different methods plotted against the publication year. Starting from surface modification methods, the surface silanization method was adopted to improve the dispersity of nanoparticles. The new and more sophisticated method (nanoscale ionic

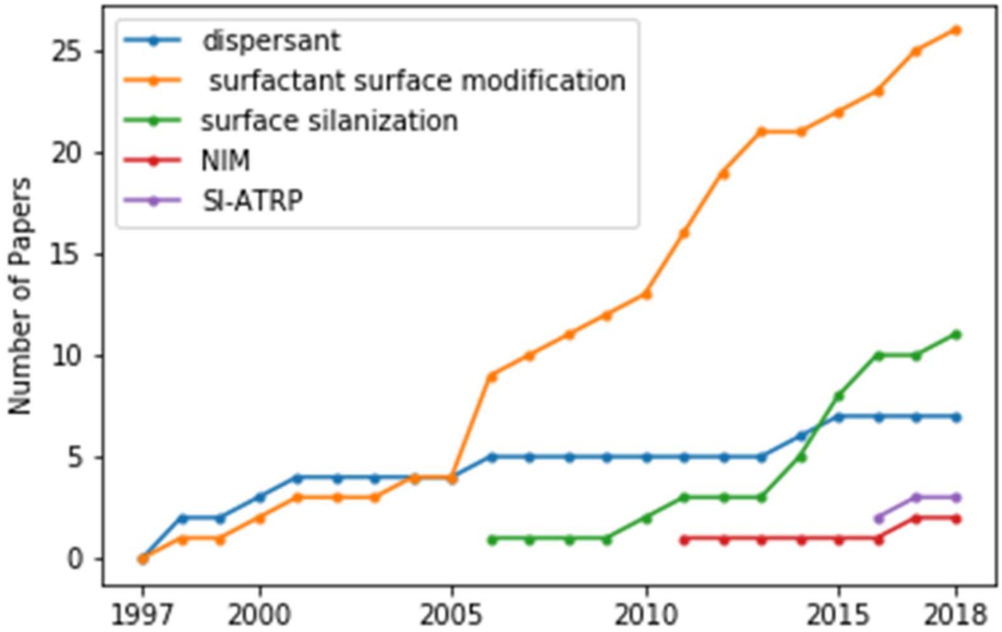

Figure I.2 The accumulated number of publications using different methods each year.

materials and surface induced atomic transfer radical polymerization) was developed and achieved a remarkable result. This chapter discusses those methods, specifically the processes those methods entail, the effectiveness of those methods and corresponding processes in achieving a stable dispersion.

Surfactant modification was one of the most widely used methods for nanoparticle dispersion (table 1). Instead of adding the surfactant to the lubricant oil as a dispersant, this method attaches surfactant molecules onto the surface of the nanoparticle. The formulation of lubricant oil was not changed to suit the need of nanoparticle dispersion.

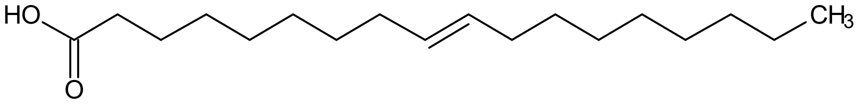

Oleic Acid

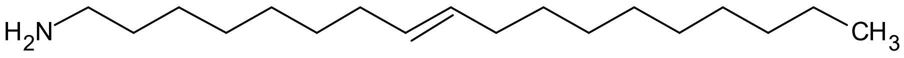

Octadecylamine

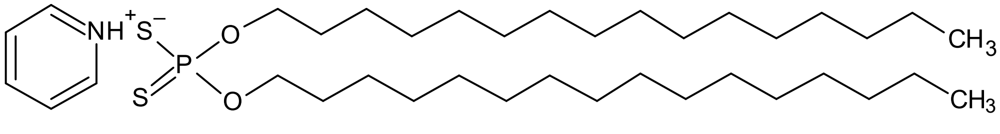

pyridinium di-n-hexaoctyldithiophosphate [PyDDP]

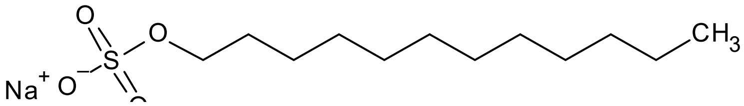

Figure I.3The chemical structure of some surfactants used in surfactant surface modifications.

The surfactant modification method uses the surfactant with functional groups that can react with nanoparticle surfaces. Some examples of those surfactants are shown in **Figure I.3**. Each of these surfactants have an active group and a long alkyl chain which contain about 15 carbon atoms. These surfactants were used to directly modify nanoparticle surfaces. This was performed by mixing nanoparticle, solvent and surfactant at an elevated temperature for a certain amount of time. The nanoparticle needs to be well dispersed in this solvent, or the surface modification process will be impeded [110]. Different nanoparticles and surfactants have different reaction mechanisms. For example, The carboxyl group in carboxylic acid can react to the hydroxyl group on the oxide nanoparticles through esterification [44,92,111,112], while the cationic surfactant can ionically bond to the surface of nanoparticles [42,81,85,113,114].

Treating the metal oxide nanoparticle surface first with acid or oxidant can enhance the binding between nanoparticles and surfactant, thus enhancing the dispersibility of nanoparticles [110,115]. Without these treatments, part of the surfactant does not chemically bond to the surface of the nanoparticle [111,112], and can be dissolved into the lubricant oil when the solubility of the surfactant in the oil is high [112]. However, these treatments cannot effectively modify metal sulfate nanoparticles [77]. The metal sulfate nanoparticles have the best performance as a friction modifying additive [1]. Due to lack of hydroxyl group, however, modifying surface with amine or carboxylic acids was difficult. The sulfate nanoparticles modified with surfactant resulted in dispersions with low stability [77].

To solve above mentioned problem, another modification method was developed. Instead of modifying nanoparticles, this method uses a surfactant to modify the precursor of nanoparticles first, then forming nanoparticles with surfactant pre-attached. The tungsten sulfide nanoparticle synthesized using this method achieved remarkable dispersion stability in both room temperature and low temperature conditions [72]. This method can also synthesis other kinds of metal sulfide. However, their dispersion stability in lubricant and the tribological impact is still unknown [116].

The dispersion stability of the surfactant modification method also closely linked to the size of the nanoparticles. Nanoparticles under 10nm in size shows better stability of dispersion by using surfactant surface modification method [32,42,72,74,77,89]. This result can be explained by classical steric stabilization theory, which is discussed in the next chapter.

1.2.1.4 Silanization

The surface silanization method is almost exclusively applicable to metal oxides and metal nanoparticles with surface oxidations. This method uses alkoxysilanes to modify the nanoparticle surface. **Figure I.4** presents a few examples of alkoxysilanes used in the stabilization of nanoparticles in lubricant [42,53,55,57,59,64,107]. Like surfactant, alkoxysilane molecules have a functional group capable of reacting with nanoparticle surfaces (Si-CH3), and a functional group that can stabilize the nanoparticles in oil. Surface silanization process can graft not just alkyl functional groups but also other functional groups like the amino group or the epoxide group.

Typical treatment of TiO_2 or SiO_2 nanoparticles was mixing the alkoxysilanes and nanoparticles in solvent under base environment and elevated temperature [42,53,55,57,59,64,107]. Two chemical processes would occur during the surface silanization process: forming of Si-O-Metal bonds on a nanoparticle's surface through hydrolysis and condensation of silane alkoxy groups, and the oligomerization between two alkoxysilane molecules [117–119]. These two competing chemical processes created a structure on the surface layer that had a complex conformation (**Figure I.5**). Studies surveyed in Table 1 used silanes with a three silanes functional group and long reactions under aqueous condition. Under this condition, a thick interlinking layer formed [118]. However, even with this layer the nanoparticles functionalized with the amino group still had poor stability compared to the nanoparticles functionalized with alkyl chains in lubricant oil [57].

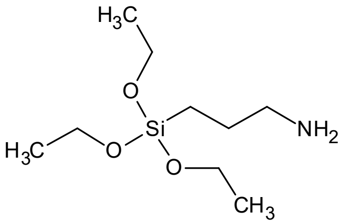

(3-Aminopropyl)triethoxysilane [APTS]

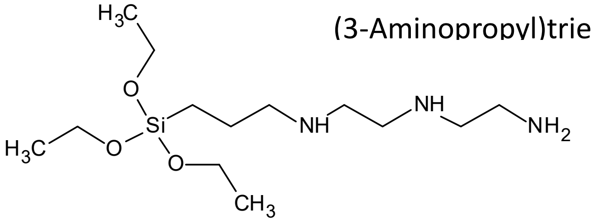

N1-(3-Trimethoxysilylpropyl)diethylenetriamine [DETAS]

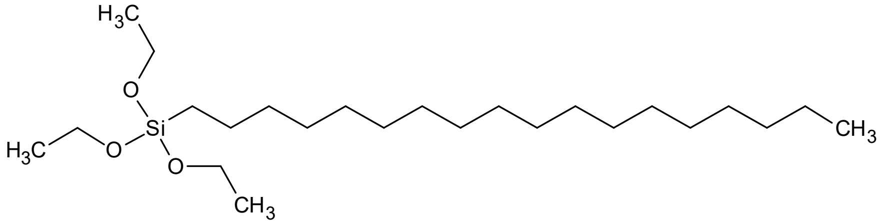

octadecyltrimethoxysilane [ODTES]

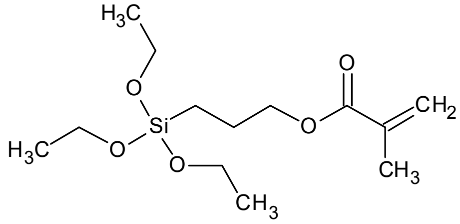

3-Methacryloxypropyltrimethoxysilane [A174]

Figure I.4The structure of silanes used to modify the surface of nanoparticles.

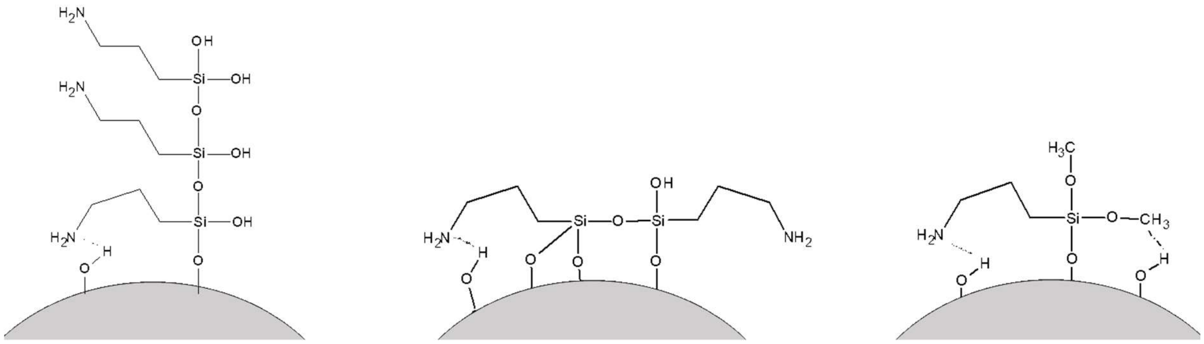

Figure I.5 The Structure of APS treated silica nanoparticle surface

For nanoparticles that have little or no surface hydroxyl group, it was difficult to directly use silanes to perform surface modification. The IF-WS_2 treated with ODETS could be stabilized in liquid paraffin for less than one week [70], but similar sized silica nanoparticles could be stable for more than 4 months [57].The methods to mitigate this problem were surface oxidation [107,115] or coating the surface of nanoparticle with silica [120].

Even though nanoparticles with long alkyl chains grafted on its surface can form more stable dispersion in lubricant oil, the alkoxysilanes with long alkyl chains were not used by most of the research reviewed. This was likely because the price of those types of alkoxysilanes were more expensive compared to amino silanes such as APTEOS or DETAS.

A two-step functionalization method was developed to solve this problem. The first step of the modification was the grafting of alkoxysilanes with an amino group. The alkoxysilanes of choice were APTEOS [54,121] or DETAS [53,55] because they have amino groups. The second step was the usage of carboxylic acid surfactant such as lauric acid [54] or stearic acid [53,55,121] to bond with the amino group. This method can graft long alkyl chains on the silica surface without using expensive ODTES. The benefit of long alkyl chains is discussed in the next chapter. This method can result in a thicker grafted layer with a good affinity to the lubricant oil.

In contrast to the surfactant surface modification, all the nanoparticles which used surface silanization were larger than 10nm size. The particle surfaces modified by surfactant had the curvature being influenced by the grafting density of silane [122]. The large curvature of small nanoparticles could limit the reaction between alkoxysilane and a hydroxyl group, reducing the repulsive force between particles [122]. Additionally, almost all the papers reviewed used an excessive amount of silane in the surface modification process. However, this practice may lead to irreversible aggregation of nanoparticles when small nanoparticles were used [123]. The importance of grafting density is also discussed in the next chapter.

1.2.1.5 Other methods

Some recent work reported the adaption of silane modification method to develop nanolubricants based on surface-induced-atom-transfer-radical polymerization (SI-ATRP) and nanoscale ionic material (NIM).

The surface-induced-atom-transfer-radical polymerization method can graft a long chain polymer on the surface of nanoparticles [45,50,124,125]. Instead of using long chain molecules on the nanoparticle surface, this method uses silanes to graft the initiator and then uses this initiator to react with monomers, forming a polymer on the surface [45,50]. This method can graft polymers with more than 100 c-c bonds [45], an order of magnitude higher compared to the results with the surfactant modification or surface silanization methods. This method also achieved a remarkable dispersion stability. The TiO_2 and SiO_2 particle treated with this method can stay stable over a large temperature range (-20C to 140C) for a long period of time (>2 months) [45,50].

The method nanoscale ionic material employed a two-step surface modification process. The first step of the surface modification was tethering an ionic corona by surface silanization and ion exchange. The second step was linking an organic counter-ion to the surface [48,126]. This formed a liquid-like material that could be dispersed into both polar and non-polar solvents [94].

Essentially, those two methods further altered the nanoparticles’ physical and chemical properties. They should be regarded as forming of new nanomaterials instead of simply a method to achieve suspension.

1.2.1.6 Evaluation

The methods discussed above have different effectiveness and reliability. In Figure I.6 the reported minimum stabilizing times were plotted, each marker representing one report on the stable time of one nanoparticle dispersion.

According to this aggregated data, surface modification was undeniably more effective compared to dispersing nanoparticles without surface treatment or formulating the oil with dispersant. Among the surface modification methods, the surface silanization method appears more reliable.

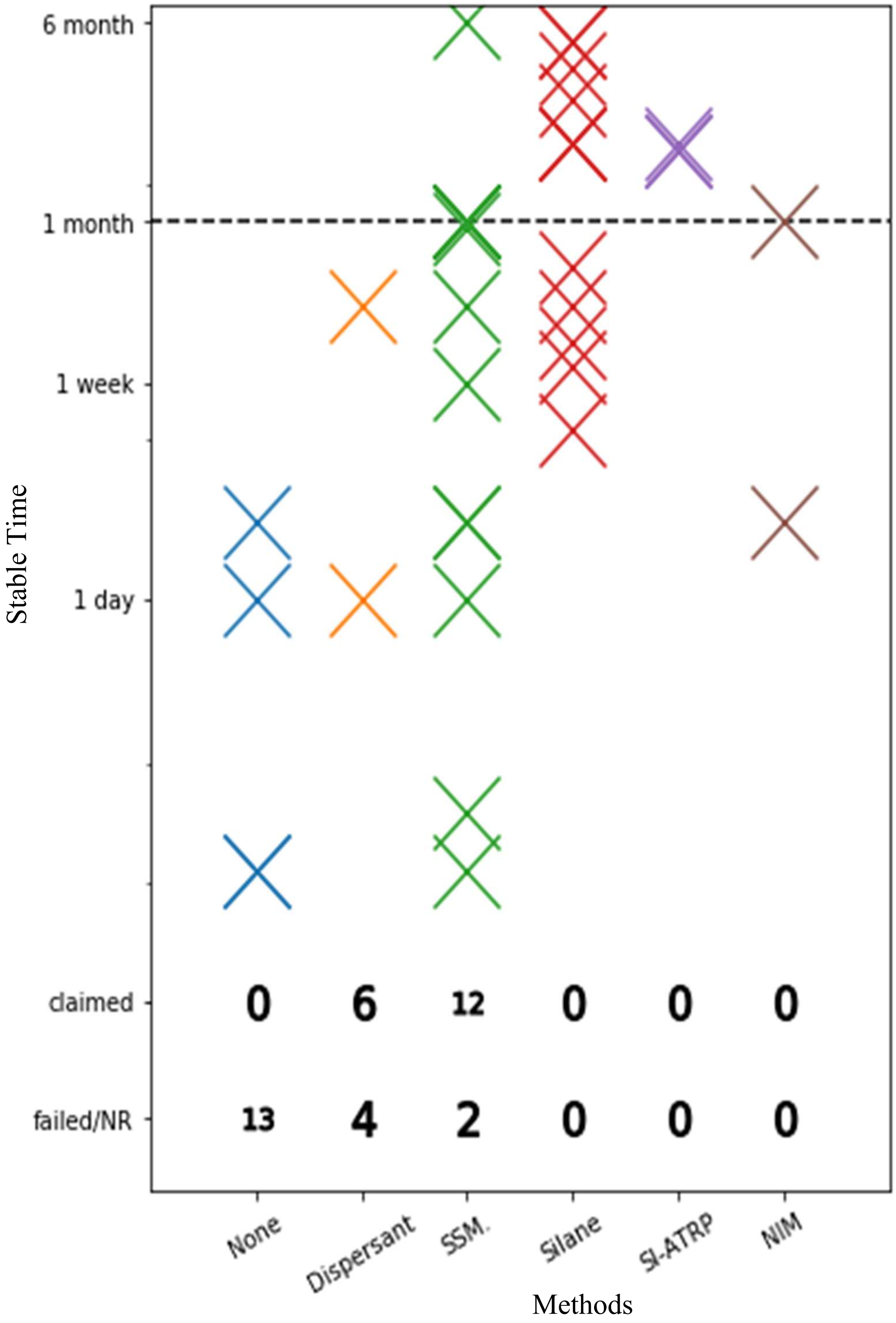

Figure I.6 The stable time for different method from surveyed studies in table 1. Every marker represents one least stable time reported by the papers.

From the data, it appeared the method that can graft a dense layer of alkyl chain on the nanoparticle surface has the best dispersion stability.

1.2.2 Use of nanolubricant in high pressure applications

Due to its high surface area of nanoparticles, the nanolubricant has high potential to be used in high pressure applications. Two of such application was introduced in this section. The first application is using the nanolubricant to prevent galling. The second application is using the nanolubricant to prevent tooth damage. These two seemingly wildly different topics shared the same tribological condition: wear under high pressure and low entrapment speed.

In industrial applications such as oil and gas exploration, metal forming, and machine elements like air bearings, one of the most common failures is galling. [127–130]. Metals are known to be galled under severe contact conditions. In particular alloys containing face-centered cubic crystal structure, such as those in austenite stainless steel or aluminum alloys, are susceptible to galling failure [131]. Galling is known as an extreme form of adhesive wear, often characterized by the protrusions formed above the original surface[132]. In Figure I.7, a 3D rendering of galled surface shows the typical feature of galling damage. Slow sliding speed, high contact pressure, and inadequate lubrication are often associated with galling. Galling can be in the forms of cold welding, instant seizure, and breakage of components, [133] that are catastrophic.

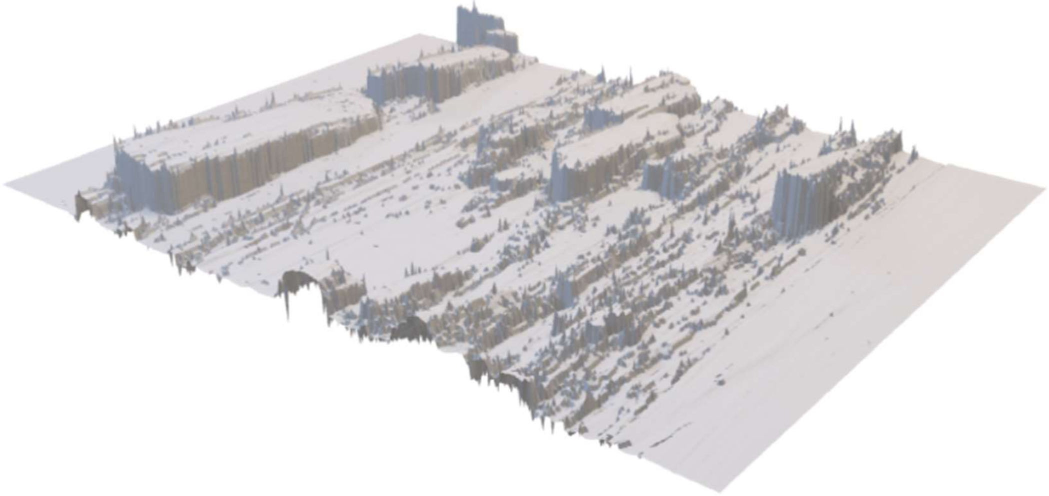

Figure I.7 The characteristic a galled surface rendered in 3D.

One of the most common methods to mitigate galling was providing grease lubricant to the rubbing surfaces. Lubricating grease is a semi-fluid lubrication agent consisting of thickening agent, lubricant oil and additives[134]. In a grease, lubricating oil was kept inside a thickener by van der Waals force[135], and release under shear[134]. The thickening agent can be soaps[136], polymers[134], even carbon nanotube[137]. Commercial anti-galling grease typically containing additives that are known to have an anti-galling effect. Those anti-galling additives including lead or copper flakes, solid lubricants such as graphite, metal fluoride or organic additives[138,139].

Tooth enamel is the hardest and most dense structure in the mammalian body. It serves to protect the interior of the tooth from the normal flora of the oral cavity and other harmful substances [140,141]. Although it is the hardest tissue in humans and animals [142–145], it can suffer damage from mechanical forces[146–151] and acidic solutions[152–155]. In dogs, the enamel layer is significantly thinner than in humans[156] and more prone to excessive wear and damage. This type of wear can result in dentin and pulp exposure causing significant oral pain, tooth loss, or periarticular and pulpal infections[157,158], leading to deterioration in quality of life and, in extreme cases, to be life threatening[152,159,160].

Recently, remineralization of damaged tooth enamel was presented as an alternative method to traditional dental operations[161–163]. These researchers utilized the bio-mineralization process that naturally presented in the dental environment[164–166]. Precursors to the nano-particle hydroxyapatite were used to form the hard enamel tissue in vitro or in vivo[162,166]. Some examples of the precursors are casein phosphopeptide-stabilized amorphous calcium phosphate[167–169]; amelogenin with fluoride[170], and polydopamine with hydroxyapatite (HAP)[162]. Unlike traditional dental treatments, this method repaired teeth with materials that were almost identical to the teeth themselves. However, like the natural biomineralization process, using the remineralization method required significant time to take effect[161,162,166]. This is a major limitation to the clinical application of this approach.

1.3 Methods to evaluate lubricating oil performance.

Experimentally evaluate the lubricating oil is essential. The tribological test for the lubricating oil simulated the working condition of contacting moving parts. Combining with physical property test such as rheological test and resistance test, the property of a working lubricant can be measured. One of the most common configurations of tribotesting used pin-on-disc or ball-on-disc configuration. They used a pin or bearing ball to push against a revolving disc while recording the friction force. The tribotesting method used such configuration can be used to evaluate tribological properties such as anti-wear properties or lubricity[171,172].

Previous studies on probing the electrical properties of materials during contact have been focused on the measurement of contact resistance[173–176] or the nature of an oil film[177–180]. Experiments have been conducted by probing the direct current conductivity or alternative current conductivity of a tribopair. The contact resistance was obtained through the DC current resistant; the film thickness was obtained by analyzing the AC current resistant [177,179]. In order to simultaneously measure the thickness of a lubricating film and the electric resistance, we used an approach to impose the impedance measurement on friction monitoring.

Tests on the lubricant electric damage can be performed on the motor or in lab-controlled conditions. To test the performance of a lubricant in real life conditions, motor bearings powered with inverter can be tested in simulated rigs. The bearing current and wear can be directly measured[181] with a simulated set up. In those experiments, a voltage that simulate the voltage from an inverters was applied though the bearing to simulate the working conditions inside EV/HEV. The experiment can also be performed on the actual motors inside an EV/HEV. By using the inductive measurement on the electric motors, the so-called hardware in the Loop (HiL) set up provides more accurate measurement and can integrate into EV/HEV.

The most common experimental method for measuring the thermal conductivity of a lubricant was called the transient hot-wire method[182]. This method is illustrated in Figure I.8 (a). The transient hot-wire experimental set-up was simple to perform and has high accuracy. This method used a Pt or Ni wire which was sealed inside a cylindrical pressure vessel filled with lubricant. The wire was heated up for a short amount of time electrically, and its temperature was monitored simultaneously by its electric resistance. The thermal conductivity and the thermal capacity of the lubricant can be calculated from the temperature change of the wire. Essentially, this measurement set up can be modeled as an axisymmetric thermal transportation problem. It has an additional advantage when used to characterize lubricants, as the lubricant thermal properties are highly correlated with its pressure, and the pressurized transient hot-wire method is relatively easy to achieve.

For small quantity lubricant measurement, a laser flash method can be used for measuring the thermal diffusivity[183]. This measurement system was illustrated in Figure I.8 (b).This system used a laser to heat up the lubricant and optically measure the temperature change. Instead of an axisymmetric rod, this method models the system as an infinite sized slab. The laser heats up an infinitely thin layer of lubricant, and the temperature change thus can be fitted with a function of thermal diffusivity and thermal capacity. This method has an advantage when used for small batch experiments as it only requires tiny amount of lubricant.

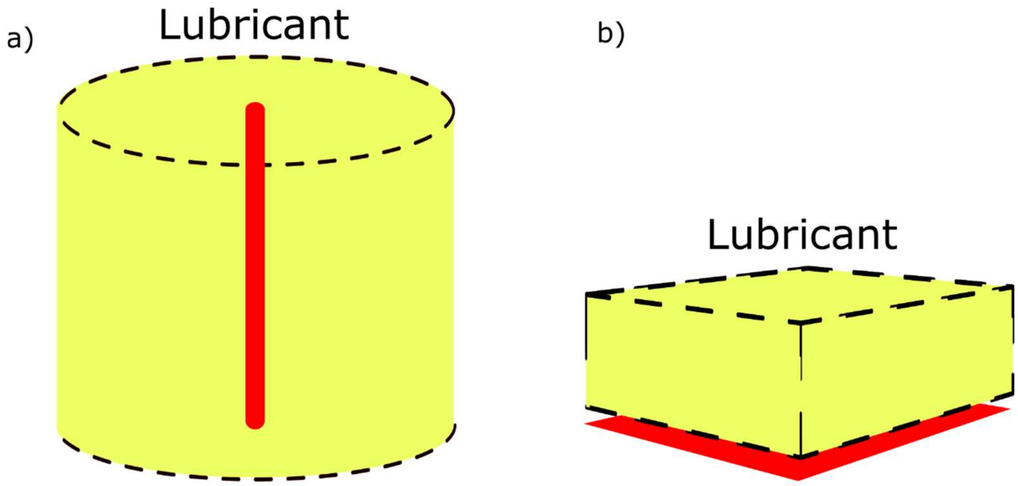

Figure I.8 measurement of lubricant thermal properties with a) transient hot-wiremethod and b) laser flash method. The yellow color indicates lubricant, and the red is the heat source.

In summary, testing a lubricant’s thermal property requires a controlled heat source and an accurate temperature monitoring system. The system accuracy and precision depended on a simple and easy to model measurement set-up. Both transient hot-wire method and laser flash method used the thermal transportation equations with reduced dimensions. The laser flash method has an advantage to testing small quantity lubricant.

CHAPTER II

MOTIVATION AND OBJECTIVES

Based on discussion in Chapter I, there is lack of effective approaches probing the tribological systems leading to understanding of tribochemical interactions. The objectives of this research are to:

1) develop novel approaches to investigate mechanisms of tribochemical and tribological interactions of nanoparticles - lubricants, and nanoparticles – substrates;
2) develop understanding in dynamic properties of lubricants, such electrical and thermal properties;
3) gain understanding in mechanisms of tribochemical interactions.

To fulfill the research objectives, novel *in situ* tribo-electrochemical testing methods on lubrication and nanolubricants will be developed. Additionally, the data processing procedure for this testing method will be created. The validation of the method will be studied with conventional lubricating oils and a synthesized nanolubricant. This research includes three areas of investigation, as shown in Figure II.1. To enable fundamental investigation, an integrated approach is used to conduct *in situ* measurement using pin-on-disc configuration combined with electrochemical impedance measurement   Using this method, experiments were conducted on amphiphilic α-ZrP nanolubricant in order to gain understanding in tribochemical interactions. The new knowledge was used to generate surface protective tribofilms, on two applications, tooth enamel and metals.

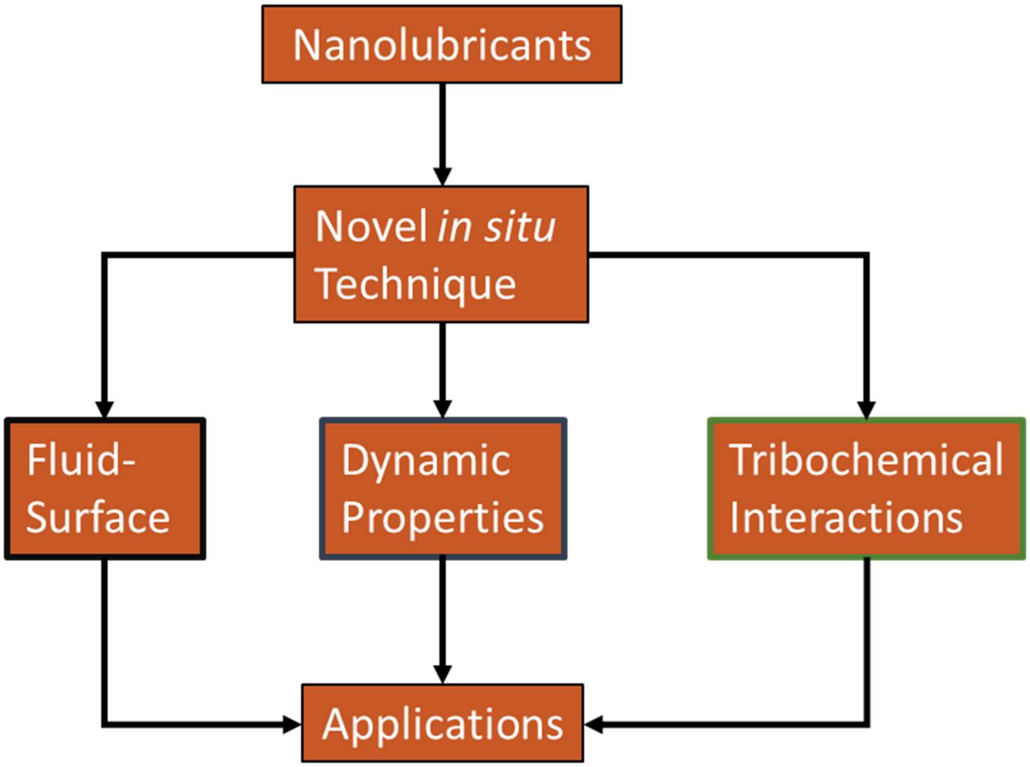

Figure II.1 Flow chart of the proposed research

This dissertation has seven Chapters. Chapter I introduced the basic concept and challenges in nanolubrication. Chapter II presented the motivation and objectives of the research. Chapter III investigated the fluid-surface interaction both experimentally and theoretically. Chapter IV discussed the dynamic properties of working lubricant with the development of the *in situ* technique. Chapter VI investigated the tribochemistry properties of the nanolubricant and how it was discovered by the tribo-electrochemical technique. Chapter VII discussed the applications of nanolubricant tribochemistry. The final Chapter gave the conclusions and recommendations of this research.

CHAPTER III

FLUID-SURFACE INTERACTIONS[2]

In this chapter, the issues of fluid-surface interactions were addressed. First, a testing method was developed to characterize the fluid-surface interaction. This was accomplished by building a new apparatus to evaluate the fluid drag in local movement. Second, the physical interactions between nanoparticles and base oil were discussed. A guideline for nanolubricant development was generated.

3.1 Characterization of fluid-surface interactions

3.1.1 The interactions between a fluid and a solid surface

Interfacial properties and performance at a liquid-solid boundary play important roles in lubricant science. Those properties however could not be characterized adequately through methods discussed earlier. This is more so when the length scale is reduced to nanometers[185,186]. Various interfacial interactions could occur resulting in an interfacial liquid layer.

Understanding the behavior of a fluid at a small length scale is important for various applications such as nano-sized pores[186,187] i.e. in membranes, shale formations, small confinement in bearings[188], and etc. The boundary between a liquid and a solid

---

[2] Part of this chapter is reprinted with permission from parts of “Nanofluidic Behavior at the Fluid-Solid Interface." by Chen, Yan, Yuan Yue, Mojdeh Rasoulzadeh, and Hong Liang. "Materials Performance and Characterization 8, no. 1 (2019): 538-550. The full paper can be found in [184].
Part of this chapter is also reprinted with permission from "Dispersion of nanoparticles in lubricating oil: A critical review." By Chen, Yan, Peter Renner, and Hong Liang. Lubricants 7, no. 1 (2019): 7. MDPI;

is beyond a steady boundary at the micrometer length scale[185,189–191]. There are many experimental techniques to study boundary slipping. There are many examples, surface force apparatus(SFA)[192,193], modified surface force apparatus [194,195] acoustic measurement[196], and others[190]. Those also had drawbacks in the measurement and characterization of liquid-solid interaction. The SFA method constrained a small amount of liquid between a ball and a flat surface, the ball was connected to an actuator and an optical displacement sensor. During measurement, the force response was recorded. This configuration could control the amount of liquid in its confinement, but produced a complex liquid flow field which was difficult to analyze. Also, the confined liquid between the ball and the flat surface was squeezed in the vertical direction, thus the effects of surface tension would affect the test result[190]. The acoustic measurement produced a simple shear flow using a quartz crystal oscillator, but without the direct measurement of force and displacement, solving the relation between the dynamic response of the crystal and the liquid-solid interaction was difficult[190].

The research presented in this chapter investigates an alternative method to probe the liquid-solid interaction in micrometer to nanometer scale through a harmonic oscillator coupled with the liquid-solid interface. With an apparatus capable of measuring applied force and its displacement, the fluidic behavior will be probed by the dynamic response of the harmonic oscillator. It will be presented that this method will produce a speed field in the fluid that is confined dynamically at the interface. A simple prototype device with preliminary results will be discussed.

3.1.2 Induced oscillatory motion

The dynamic behavior of an incompressible viscous liquid can be described by the Navier-Stokes equation and continuity equation[197]:

$$\frac{\partial \boldsymbol{u}}{\partial t} + (u \cdot grad)u = -\frac{1}{\rho} grad\, p + \nu \Delta u, \tag{1}$$

$$\frac{\partial \rho}{\partial t} + \rho\, div(u) + u \cdot grad\rho = 0, \tag{2}$$

where ρ is the mass density of the fluid, p is the fluid pressure, ν is the kinematic viscosity, $\boldsymbol{u}$ is the fluid velocity and t is time. Consider a rigid solid half space fully in contact with an incompressible fluid half space, in which the movement of the solid is constrained to move one dimensionally, parallel to the contacting surface in the x direction. Due to symmetry all parameters will depend on coordinate x and consequently the mass and momentum conservation equations can transform to equation[197,198]:

$$\frac{\partial u}{\partial t} = \nu \frac{\partial^2 u}{\partial z^2}, \tag{3}$$

where z is the direction normal to the interface toward fluid, u is the horizontal component moving speed of the fluid. This equation has the exact same form as the equation of diffusion, which can be solved analytically.

When the speed of a solid is $u_{solid} = u_0 \exp(i\omega t)$, equation (3) can be solved for the speed of a fluid. The resulting speed as the real part[197]:

$$u = u_0 \exp\left[-z\sqrt{\frac{\omega}{2\nu}} + i\left(z\sqrt{\frac{\omega}{2\nu}} - \omega t\right)\right]. \tag{4}$$

At distance $\delta = \sqrt{2\nu/\omega}$ towards the fluid, the amplitude of the fluidic speed is reduced by $1/e$ (e is the base of the natural logarithm) of that at the interfacial boundary speed. Such distance can be used as the layer thickness of the boundary. The relation between frequency and fluid speed is plotted in Figure II.2, where the x axis is the angular frequency and y axis is the distance normalized by $\sqrt{2\nu}$. The grey solid curves indicate in which positions the fluid has the same speed at different angular frequencies and the dotted solid line indicates where the speed of fluid decreased to $1/e$,$1/e^2$ and $1/e^3$ of interface speed. The colored lines plotted the speed of fluid in different angular frequencies, which were marked by the grey dotted line underneath them. As shown in this figure, the majority flow field is dynamically confined in the space closed to the interface. For instance, a fluid with a viscosity of 1 cP, δ will be smaller than $100\mu m$ when the angular frequency is larger than 100Hz.

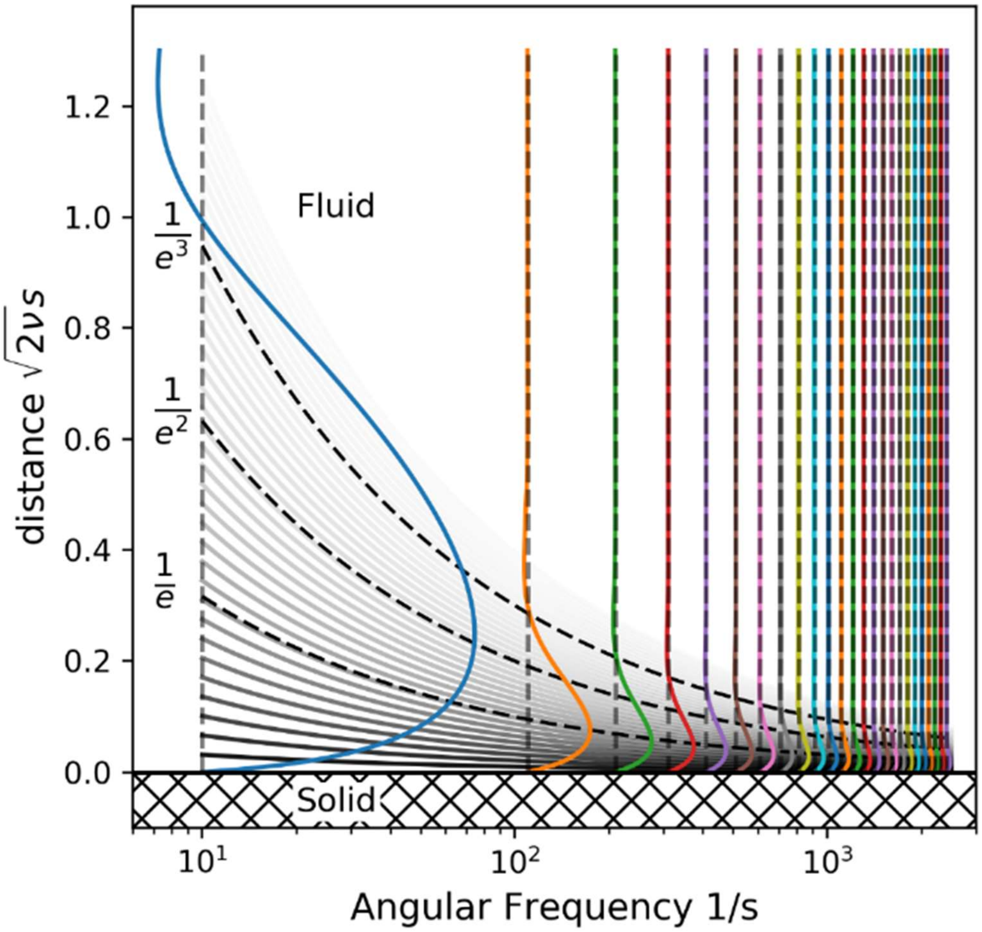

Figure III.1 The amplitude of speed field around an oscillatory surface. The solid lines' gradient indicating the relative amplitude of speed to the solid. Dotted lines indicate the distance where amplitude decreased 1/e, 1/e^2 and 1/e^3. The colored lines indicate

Detecting fluid oscillation at a small scale is important for the practicality of this design. The purpose of this research is to probe the fluidic behavior in small movement. If the movement of the oscillator was comparable with the size of the contacting surface, the fluid movement will deviate from previous calculation. It has been known that direct measurement was difficult. One feasible approach was to measure the interfacial shear strain induced by the fluid. The strain of viscous fluid was $\tau = \rho\nu\ (\partial u/\partial z)$. Here we propose a modified harmonic oscillator, shown in Figure III.3, as a working system. In the figure the harmonic oscillator has a spring constant K, damping constant λ and mass m are coupled with a fluid tangentially along with the interface in which the area is A. The previous discussion had fluid in contact with an infinite large half-space, but in the model shown in Figure 3, the liquid-solid interface has a finite area. This will change the flow of fluid because of the existence of the edge. However, the dynamic response of this finite interface can be estimated by the response of an infinite interface. A stress acts on a finite interface with an area A is equivalent to that acts on an infinite half space with a slightly larger area A_e. This slightly larger area can be estimated by moving the edge of the certain area by a distance of $\sqrt{\nu/2\Omega}$ [197]. This larger area A_e was called effective area of contact.

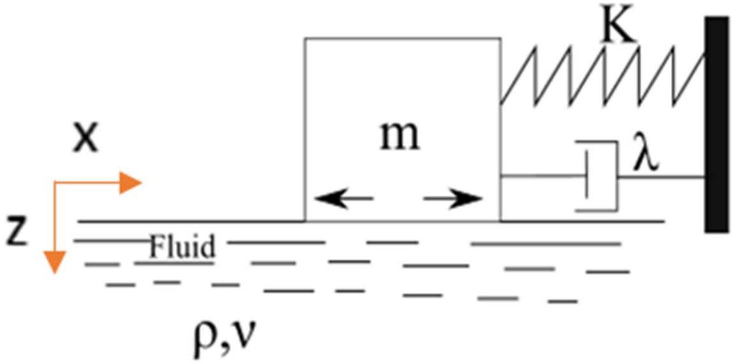

Figure III.2 The modified harmonic oscillator: a classical harmonic oscillator confined in one dimensional motion, in contact with a liquid surface parallel to its direction of motion.

The equations of motion shown in figure III. 3 can be expressed as:

(5)

$$m\ddot{q}(0,t) + \lambda\dot{q}(0,t) + Kq(0,t) - A_e\rho\nu\left(\frac{\partial^2 q}{\partial z\partial t}\right)_{z=0} = F_0\cos(\omega t),$$

where $q(z,t)$ is the position of fluid in horizontal direction, $\dot{q}$ and $\ddot{q}$ are derivatives of $q(z,t)$ with respect to time. A_e is effective area. The last term on the left-hand side is the shear forces exerted by fluid to the surface. Note that

$$\frac{\partial \mathrm{q}}{\partial \mathrm{t}} = \mathrm{u}, \qquad \frac{\partial^2 \mathrm{q}}{\partial \mathrm{t}^2} = \frac{\partial^3 \mathrm{q}}{\partial \mathrm{z}^2\,\partial \mathrm{t}}, \tag{6}$$

The solution of the equation (5) at $z = 0$ is a simple triangular function. Thus, assuming the movement is confined in one frequency, the equation of motion can be rewritten as:

$$\left(m + A_e\rho\sqrt{\frac{\nu}{2\omega}}\right)\ddot{q_0} + \left(\lambda + A_e\rho\sqrt{\frac{\omega\nu}{2}}\right)\dot{q_0} + Kq_0 = F_0\cos(\omega t), \tag{7}$$

with $q_0 = q(0,t)$. The long time solution to this equation is:

$$q_0 = C\cos(\omega \mathrm{t} - \phi), \tag{8}$$

where,

$$C = \frac{F_0/m_e}{\sqrt{(K/m_e - \omega^2)^2 + \omega^2\gamma^2}}, \tag{9}$$

$$\gamma = \frac{\lambda_e}{m_e}, \tag{10}$$

$$\phi = \tan^{-1}\left(\frac{\lambda_e\omega}{K - m_e\omega^2}\right), \tag{11}$$

$$\lambda_e = \lambda + A_e\rho\sqrt{\frac{\omega\nu}{2}}, \tag{12}$$

$$m_e = m + A_e\rho\sqrt{\frac{\nu}{2\omega}}. \tag{13}$$

In an underdamped system, the amplitude around nature frequency is very sensitive to damping constant.

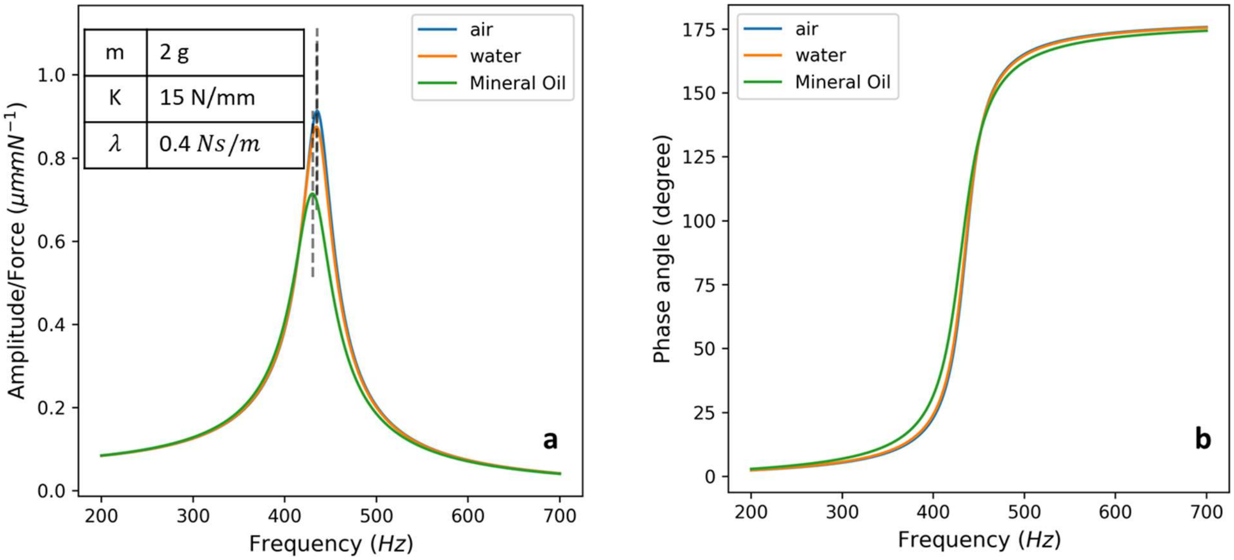

Figure III.3 The calculated amplitude(a) and phase angle(b) of proposed system in different frequency.

Consider a system with a spring constant of 15 N/mm, mass $2g$, damping constant $0.4N \cdot s/m$ and contact area 2 cm^2, we calculated the vibration and phase angle of air, water, mineral oil and results are shown in Figure III. 4. The viscosity of water was 1 mm^2/s and the density $1g/ml$. That of oil was 65 mm^2/s and the density $0.85g/ml$

.

A fluid has two effects on the oscillator. The first is a subtle frequency shift and second the change of amplitude around the natural frequency. This phenomenon could be interpreted as follows: The mass of fluid close to the oscillator moves along with the oscillator and changes natural frequency. The energy dissipation into the fluid increases damping thus lowering the amplitude. It is notable that these two effects still hold even if the behavior of fluids deviates from classical hydrodynamics. For example, if the movement of the oscillator is small, boundary slipping could occur. This means the speed of fluid at the interface is not the same as the speed of solid at the interface[28,30]. But the energy dissipation and the mass of fluid dragged by the solid still exist. This means that a liquid behaved in interface differently from that in its bulk following classical fluid dynamics. Direct probing would provide insight from the fluidic property.

3.1.3 Instrument design and experimental procedure

3.1.3.1 Prototype configuration

The previous section presented an abstract model to test the interfacial properties of the liquid. To validate the model, a prototype was built. The design of this prototype can be found in the published journal paper[184].

3.1.3.2 Fluidic measurement

Calibration was performed before testing fluids. There are several unknown parameters inthe configuration: the capacitance to displacement ratio of displacement sensor, the load-to-current ratio of load transducer, the mass, spring constant and damping constant of the harmonic oscillator. Those parameters were not independent to each other, if two of the parameters were known, the others could be calculated by curve fitting the experimental result. The displacement sensor and the spring constant of the harmonic oscillator were chosen to be calibrated. The displacement sensor was calibrated first. The instrument was mounted firmly on a rig. A micrometer mounted on the same rig was attached to the moving part of the harmonic oscillator. It actuated and measures the displacement of the oscillator. Then, an AC voltage of 5kHz 10V was applied to the sensor. The micrometer located the harmonic oscillator in different positions, and the output voltage of the displacements sensor was recorded. The relationship between output voltage and the displacement sensor was calculated. Then, the spring constant of the harmonic oscillator was calibrated. The instrument was flipped so that the moving direction of the harmonic oscillator was perpendicular to the ground. Different weight was hung on the oscillator and the resulting displacement was recorded. The spring constant was then calculated from the result.

The fluid evaluation was performed after the calibration process, the harmonic oscillator was excited by an AC current with different frequencies with the same amplitude at

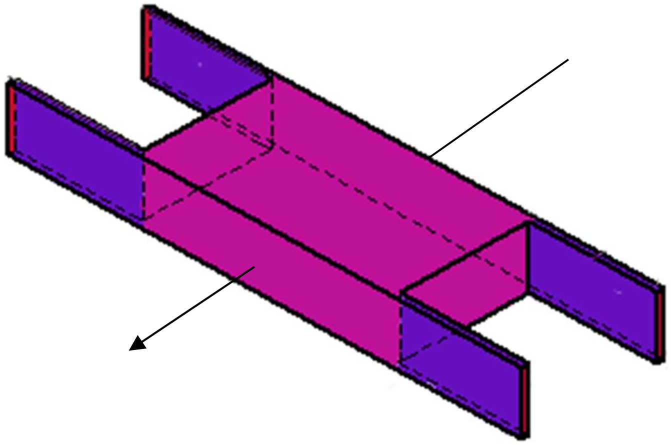

Figure III.4 Supporting leaf springs. The blue colored section was the springs, and the purple colored was the oscillator. Springs was connected to the frame at the locations colored red. The arrow shows the moving direction.

0.12A. The range of test frequency was 200Hz to 700Hz. The result of displacement and applied force were recorded for 10ms.

The first test was performed with no fluid in contact with a glass slide. The only subject interacts with test system was air. This test was also used to determine remaining oscillator parameters: mass, damping constant and force to current ratio. The resulted force to current ratio was 0.06 N/A, oscillator parameters were shown in Figure III. 6. Following this test, two specimens were put under the glass slide subsequently. They are de-ionized water, and mineral oil (Sigma-Aldrich 330760). A clean plastic beaker was put under the glass slide before each test. These liquid specimens were injected into this beaker until the liquid surface was just in contact with the glass slide. The surface was checked by the naked eye to make sure there was no visible curvature around the liquid-solid contact and no visible bubble between the slide and liquid. The thickness of liquids under the contact surface was more than 3 mm. This gave a sufficient distance between contact and beaker bottom. After the test with de-ionized water, the underside of the glass slide was cleaned and left air dry before testing on mineral oil.

The parameter of the oscillator calculated from the calibration process and experiment on air was shown in the table inside Figure 6 by assuming only linear damping happened when the instrument in contact with only air.

3.1.4 Fluid behaviors

3.1.4.1 Fluidic response to vibration

After the experiment, the pseudo-steady fluidic response to the vibration was calculated. the frequency vs. amplitude/force of three different experiments is graphed in Figure 6a, with the testing force of $77 \pm 4mN$. The general trend of this result shows of a typical under-damped oscillator behavior as expected. Because the damping from the fluid is scaling with the frequency, the amplitude was not changed significantly before the natural frequency. The vibrational amplitude of mineral oil and the air was very close in small frequencies. Near the natural frequency of the oscillator, it produced the highest amplitude to force value. In this region, damping constant has a significant impact on the vibrational amplitude. As expected, the oscillator in contact with air has highest value, while water and mineral oil will suppress the amplitude of the oscillator to different extent.

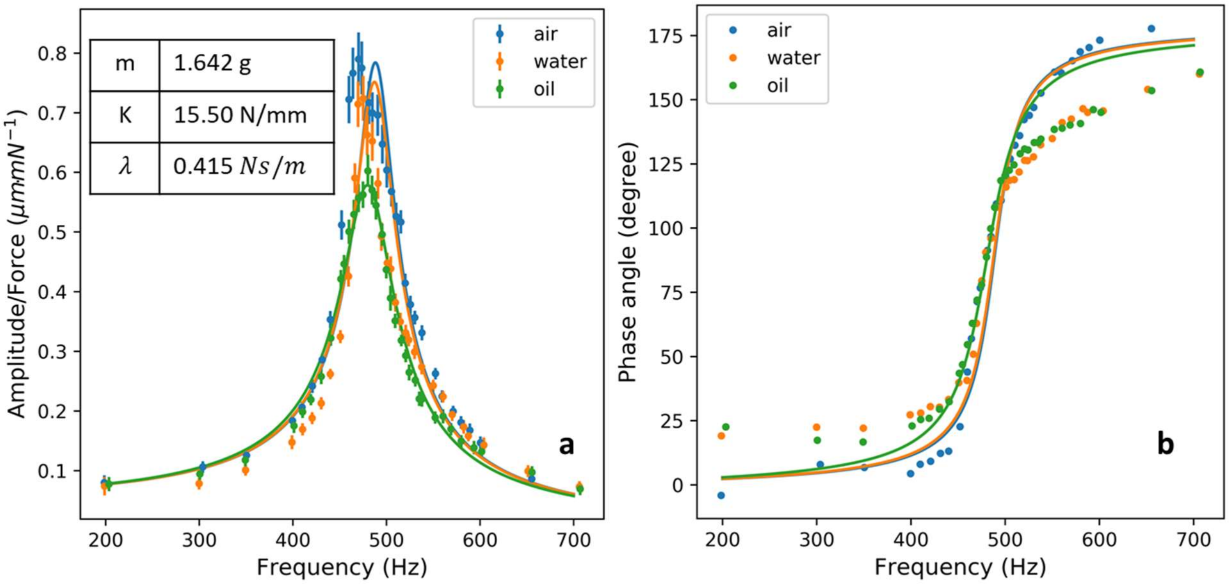

Figure III.5 The measured value of amplitude and phase(a) and phase angle(b) with air, water and mineral oil. Solid line is the calculated value.

To compare the experimental result with Newtonian fluid, calculated Newtonian amplitudes and phases from three fluids are plotted as solid lines in figure 6 using the literature value of mineral oil ($\nu = 65\ mm^2/s\ , \rho = 0.862 g/ml$ from manufacture specification) and the deionized water ($1\ mm^2/s,\ \ 1g/ml$) [199]. Compare to the experimental result, the amplitude value result was fairly accurate with only the data from testing water and air shows a slight frequency shift, as if the mass of the oscillator decreased with increasing damping. This was expected because both deionized water and mineral oil are simple fluids that do not react with silica test surface. However, the shape of the response curve deviated from what we expected in two ways. Firstly, the phase angle of the water and oil contact deviated from classical response when the frequency was below 450Hz and higher than 500Hz. Additionally, both the shape and the natural frequency of system when in contact with water or air were slightly shifted left. These phenomena indicated that the fluid-solid interaction was more complicated than the classical model we proposed before. The physical significance of these new phenomenons is discussed in the published paper[184].

3.1.5 Summary

This research presented an alternative and simple method to probe the fluid-solid interface enabling the study of nanofluidic behavior. A working prototype device was developed, and initial testing showed that this method was suitable for studying fluidic mechanical properties.

The system can be further improved in terms of flexibility and ease. A dedicated driver circuit and control system will reduce the time required for testing and data processing.

Additional displacement transducer on vertical direction movement can also make many other types of tests using the same principle possible. With those improvements, more complex fluidic systems can be investigated, such as nanofluids.

3.2 The interactions between nanoparticles and base oil

3.2.1 The theory of nanoparticle-nanoparticle, nanoparticle fluid interactions

The dispersion of nanoparticles can be explained by colloidal theories, theories which study the mixture of dispersion and dispersant [200]. The mechanically dispersed particles studied in colloidal science ranged between 1nm and 1000nm in size, a range which overlaps the size of nanoparticles.

In colloidal theories, the tendency in aggregation of nanoparticles was determined by two factors: the interaction between nanoparticle and solvent, and the interaction between nanoparticles. The study of the first interaction resulted in the Brownian motion of nanoparticles. The thermal agitation in the solvent has an energy of $K_b T$, where K_b is Boltzmann constant and T is temperature. This thermal agitation was shown to push the nanoparticles to move randomly in the solvent [201]. The second interaction resulted in the attractive and repulsive forces between two particles [201]. Stable dispersion formed when the thermal agitation overcame the force between particles.

Three major interactions occur between nanoparticles and are explained by two different colloidal theories. The DLVO (Derjaguin and Landau 1941, Verwey 1948) theory was a pioneering and most influential theory. It explained the dispersion stabilization through attractive van der Waals forces and repulsive screened electrostatic forces [201]. The theory of steric stabilization was developed later to explain the “protected” particles, e.g.

the particles with absorbed or grafted large molecules [202–204]. This theory argues that a grafted molecule generates a repulsive force when another particle approach it. In both theories the attractive force is long-ranged while the repulsive force is short-ranged. The combination of these forces generates a potential well, and the stabilization is achieved when the thermal energy is larger than the potential well depth.

The polarity of lubricants renders electrostatic stabilization difficult in lubricant oil. Although polarity is a complex physical chemical property, in the context of colloidal dispersion the dielectric constant (ϵ) can be used to measure polarity. In organic media with $\epsilon \leq 5$, the ionic concentration is neglectable. The electrostatic interaction is weak even when nanoparticles have surface charge [205,206]. Most lubricants' dielectric constant were around 2.5 [207], far lower than the dielectric constants of water or other polar solvents (**Figure III. 7).** Thus, the surface charge of nanoparticles cannot improve dispersion in the lubricant oil. In some of the surveyed publications, ζ-potential (surface potential) was characterized and used to reflect the dispersion stability [55,57,58]. However, it was incorrect to prove dispersion stability using this characterization because surface potential contributes little to the particles' interactions in lubricant oil. Thus, nanoparticle dispersion in lubricant oil needs steric stabilization to reach long time

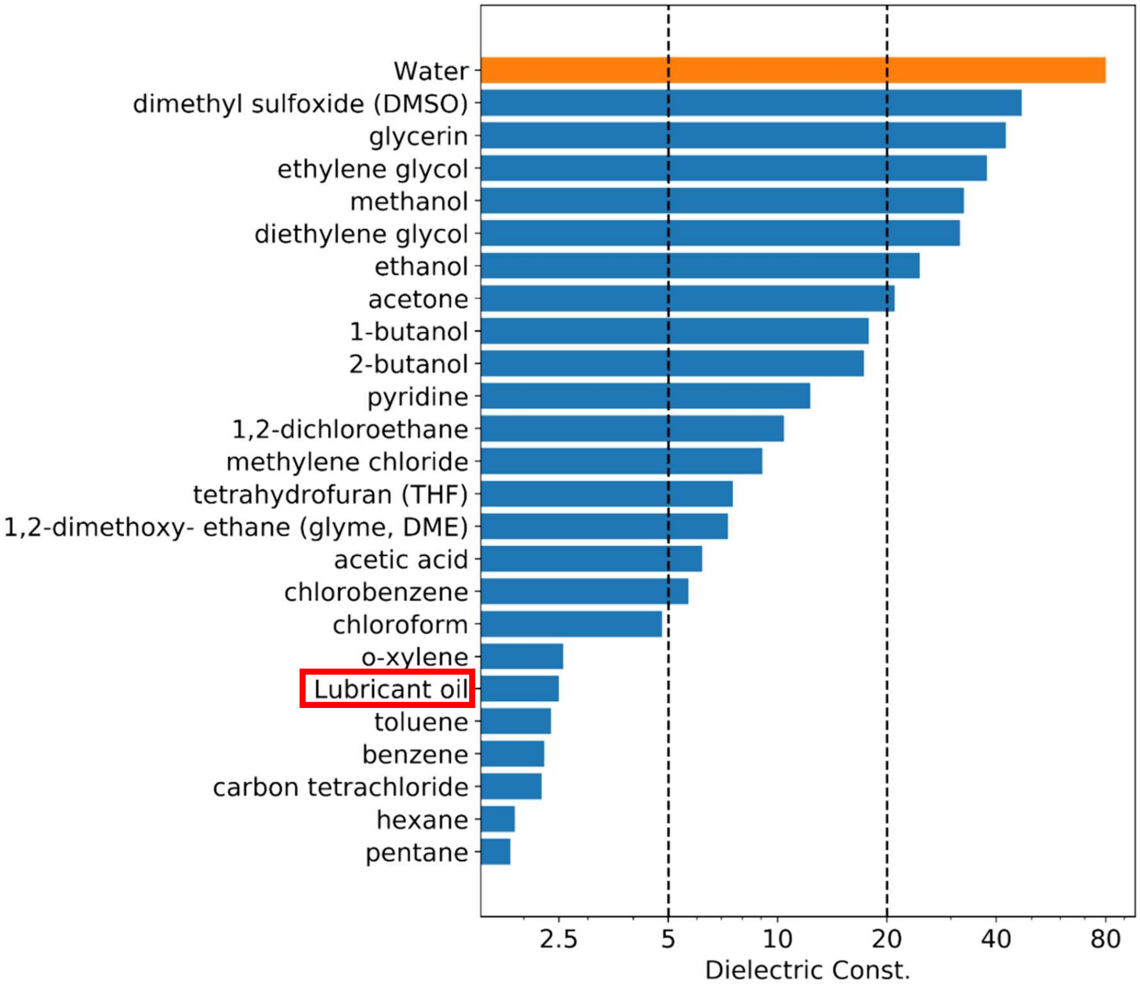

Figure III.6 The dielectric constants of selected solvents.

stability. In the next section, the analysis of suspension is conducted using the steric stabilization theory.

3.2.2 Steric stabilization

Steric stabilization was established by the balance between two forces: the van der Waals attractive force and the elastic steric force [202–204,208]. Although van der Waals force was complex in nature, a simplified form by Hamaker was used when analyzing colloidal systems [209]. Assuming the size of the nanoparticle was small, we use London van der Waals potential [209]:

$$V_{vdw}(z,R) = -\frac{A}{6}\left(\frac{2R^2}{z^2-R^2}+\frac{2R^2}{z^2}+\ln\left(\frac{z^2-4R^2}{z^2}\right)\right)$$

Here z is the distance between two particles' centers, R is the radius of the particle and A is the effective Hamaker constant. The effective Hamaker constant can be approximated by the Hamaker constant of the particles and the medium [201]:

$$A = \left(\sqrt{A_{particle}} - \sqrt{A_{medium}}\right)$$

The nanoparticles had a Hamaker constant of $10^{-20} - 10^{-19} J$ [210] and the organic media had a Hamaker constant normally about $10^{-20} J$ [211–213]. For example, the Hamaker constant of Silica in vacuum was $6.35 \times 10^{-20} J$[210]. Compared to inorganic compound, the metals had a larger Hamaker constant $22 \times 10^{-20} J$ [214]. Their Hamaker constants also increased with decrease of size [215,216]. The Hamaker constant of a 5nm sized Ag nanoparticle was $34 \times 10^{-20} J$[216], larger than that of bulk material. Thus, an effective Hamaker constant of $10^{-20} - 10^{-1}\ J$ was used to analyze the van der Waals attraction in lubricant oil.

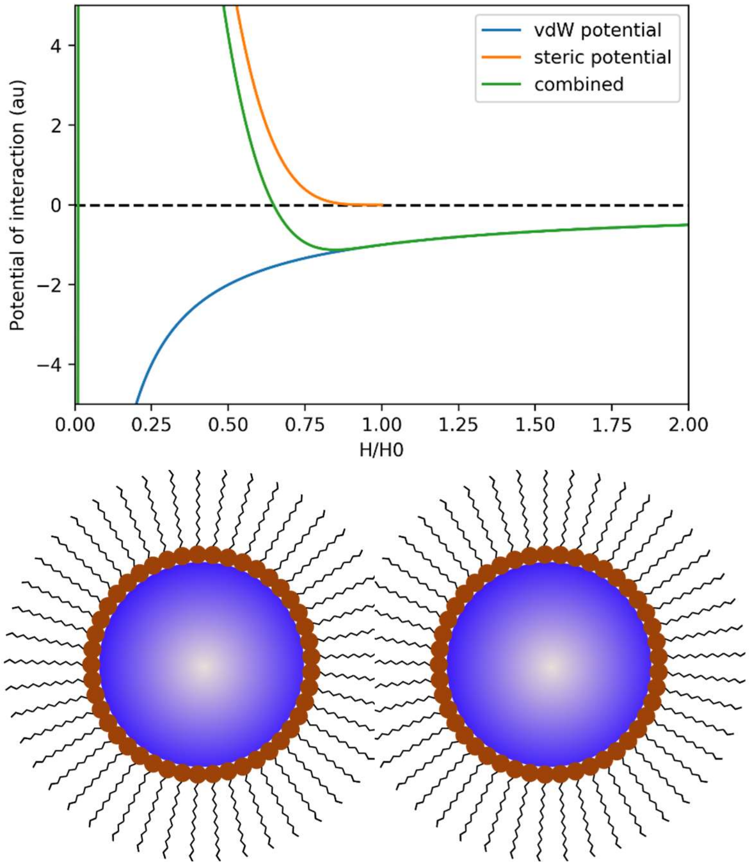

Figure III.7 The model of steric repulsion

The repulsive force originates from the deformation of the absorbed or grafted surface layer. When two particles with surface grafted layers approach, the surface layer deforms, and the conformation of the grafted molecule changes (**Figure. III. 8**). This leads to the change of the free energy and the repulsive force [204]: $f = \frac{d\Delta F}{dH}$, here, f is the repulsive force, ΔF is the free energy of the surface layer, and H is the height of this polymer layer. In small deformations, the elastic potential between two approaching particles are (modified from [204] eq. 54):

$$\Delta V_{steric} \cong \frac{f}{2} \left(\frac{H_0 - H/2}{r}\right) \Delta F(H/2) \qquad when\ H < 2H_0$$

Here, f is the density of grafted chains, H_0 is the thickness of the grafted layer, r is particle radius, ΔF is the free energy of one molecule, and H is the distance between particles. A potential well appears when van der Waals potential and steric potential are combined . If the thermal agitation is larger than this potential well, a stable dispersion can be expected.

A qualitive analysis on eq.3 leads to the major factor influencing steric stability: the size of the particles, the thickness of the surface layer, the density of grafted chains, and the free energy of the grafted chains. These factors are discussed in following sections.

3.2.3 Size effects

The theorietical analysis from the previous chapter indicates that when the same surface modification is used, a reducuction in the size of nanoparticles will decrease the attractive van der Waals force and increase the repulsive steric force. The result from the surfactant surface modification best illustrates this size effect. In Figure 9, the stable time of 7 different research articles using a similar surfactant surface modification method were plotted against the size of the nanoparticle used in their research. It appears the nanoparticles with a size smaller than 10nm has a better stability compared to the nanoparticles with a size larger than 10nm.

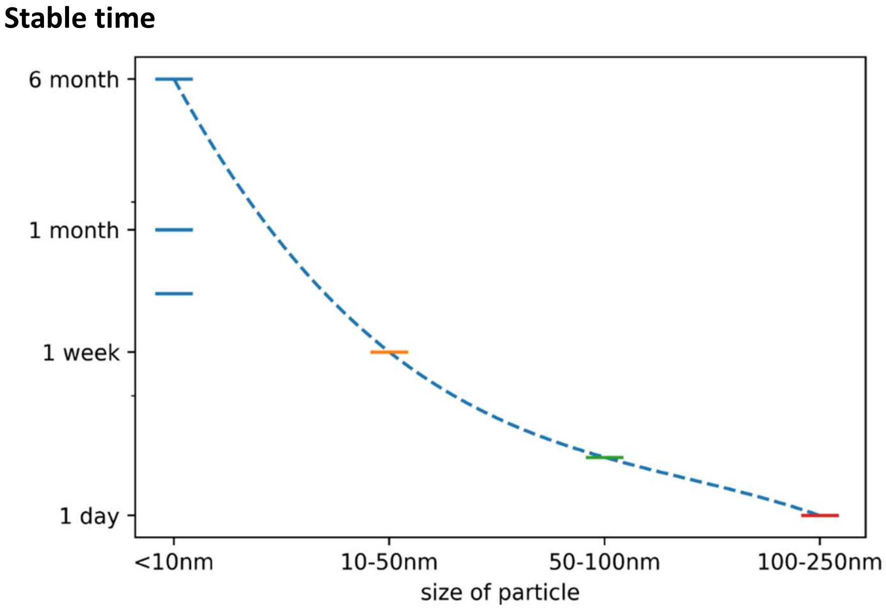

Figure III.8 The nanoparticle size and nanoparticle dispersion stability in 10 research using surfactant surface modification.

A simple estimation based on colloidal theory can explain this phenomenon. The potential well of the steric stabilization was correlated to the size of interaction particles. There was no elastic steric force beyond the thickness of the surface polymer layer. Thus, one minimum of the potential energy was around the thickness of the surface layer. The value of this minimum was smaller than the value of van der Waals potential. Only consider these two factors (surface layer thickness and van der Waals potential), an upper limit of the nanoparticle that can be stabilized by a surface layer of thickness H_0. The estimated upper limit of a nanoparticle was the root of R in:

$$V_{vdw}(H_0, R) - k_b T = 0$$

The surface layer thickness H_0 of surface modification by surfactant was about 3nm [217,218]. The estimated upper limit was plotted in **Figure III. 10**. This estimation is in agreement with the literature surveyed in this paper (**Table 1**).

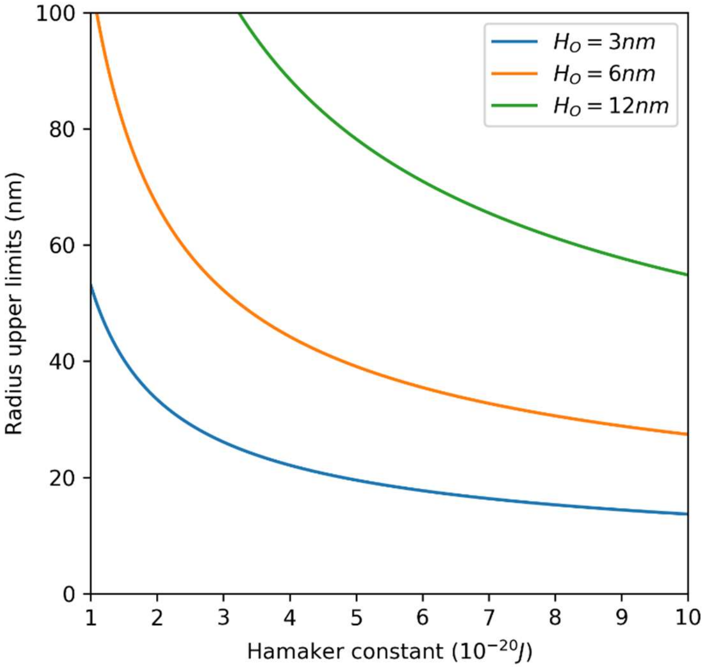

Figure III.9 The upper limit of nanoparticles that can be stabilized with grafted layer thickness of H0. The blue line can be used for surfactant surface modification.

However, from **Figure III. 9**, the nanoparticles with a radius less than 200nm still have poor stability. Both the van der Waals and the steric forces need to be considered to explain this [204]. In **Figure III. 11**, the potential of particle-particle interaction was plotted against the distance between two particles. All three figures were based on the nanoparticles with the same parameters except the particle radius. The steric potential was calculated using models proposed in reference [204]. In this figure, the potential was normalized by the free energy of the surface molecule layer, and distance was normalized by the thickness of the grafted layer under θ conditions. The only different parameter in those three calculations was the diameter of the nanoparticle. With the increase of nanoparticle size, the total repulsive force decreased until it totally vanished.

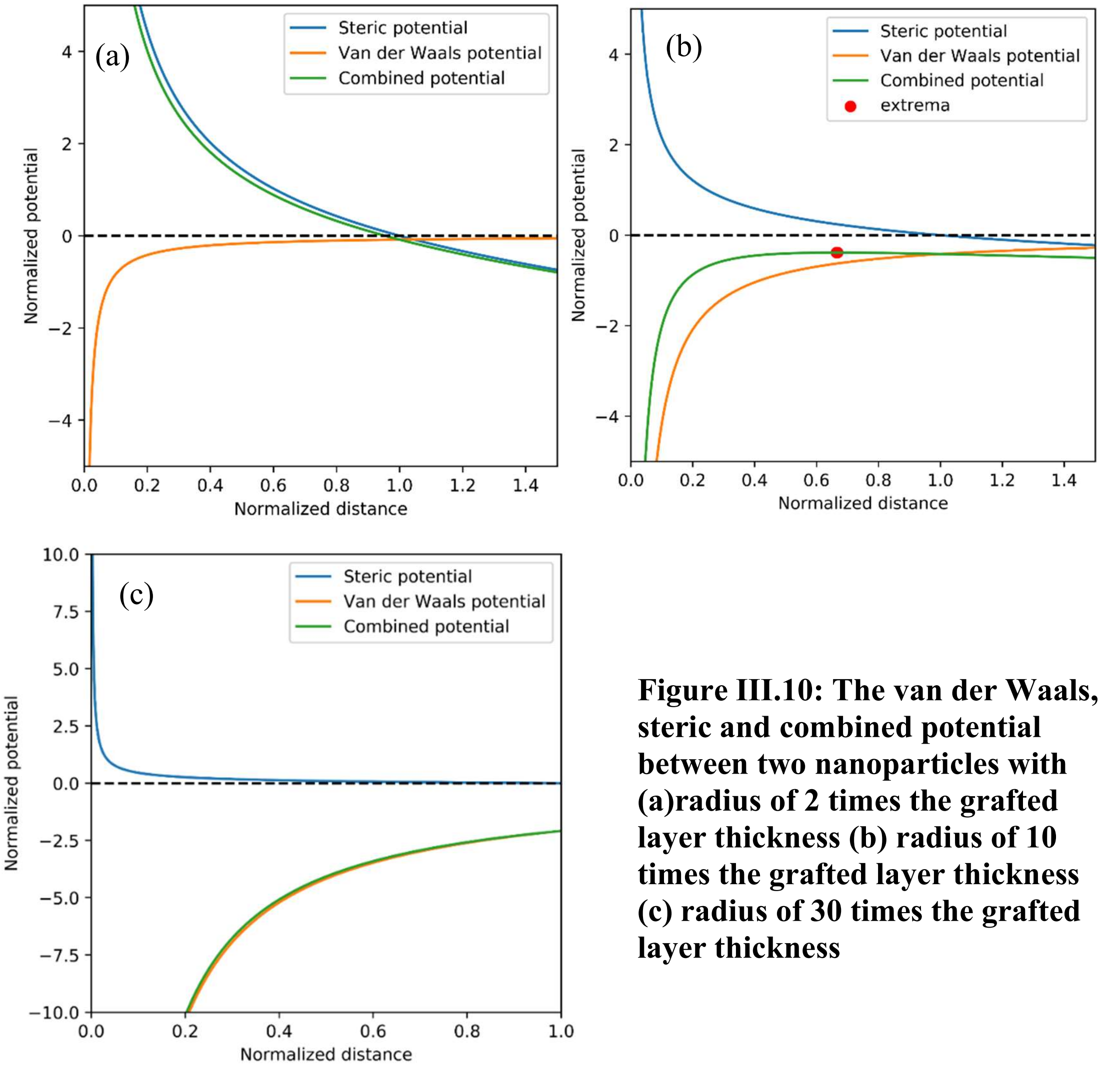

Figure III.10: The van der Waals, steric and combined potential between two nanoparticles with (a)radius of 2 times the grafted layer thickness (b) radius of 10 times the grafted layer thickness (c) radius of 30 times the grafted layer thickness

3.4 Grafted surface layers

The properties of the grafted layer can influence the ability of nanoparticles to disperse in organic media [55,57,112,217]. For the same nanoparticle, a change in the grafting density, the thickness of the surface grafted layer or the free energy can change the strength of the repulsive force (Eq.4).

The effectiveness of the surface modification method requires a sufficient grafting density. In the case of surfactant surface modification, an increase in the concentration of surfactant used has a positive impact on the dispersion stability [111,112,217]. When the nanoparticle reacted with the surfactant in the solvent, if the nanoparticle was aggregated and did not fully react with the surfactant, its re-dispersity was impeded [110].

This is the reason why surface silanization was suitable for nanoparticles lager than 50nm size. The previous chapter explained that the high curvature of nanoparticles smaller than 30nm led to poor grafting density of silane. This poor grafting density caused the low steric repulsion force, and the dispersion stability reduced.

The same reason caused nanoparticles modified with silane to provide overall satisfactory dispersion [53,55,57,59,64] compared to nanoparticles modified with surfactant [42,74,77,85,89,103]. Both silane and surfactant can react with the hydroxyl group to form a bond with the nanoparticle surface [111,112,217,219,220]. Unlike surfactant, silane can fully react with the hydroxyl group on the surface of nanoparticles. In the case of silica nanoparticle treatment, the research using oleic acid surface modification of the hydroxyl group did not fully react even with the excess amount of reactant [111]. In contrast, the silica nanoparticles modified with silane coupling agent had almost no hydroxyl group left after the reaction [219].

Moreover, the conformation of the grafted layer changed when the surface density increased [221]. The grafted layer had a “mushroom-like” conformation when the grafting was low but changed to “brush-like” with a high grafting density[221]. This resulted in a higher $\Delta F(H)$ value in Eq.4, increasing the steric repulsive force.

The free energy of the grafted molecule chain also changed by its interaction with solvent. Steric stabilization was far more effective when the dispersant was a good solvent of the molecules grafted on the nanoparticle [203,204]. A good solvent could also expand the grafted layer beyond the θ-condition, resulting in a thicker layer with a higher interaction force [204]. The nanoparticles grafted with the alkyl group shows better stability compared to nanoparticles grafted with the amino, phenyl or carboxyl groups [53,55]. This is due to the high-solubility alkyl group in the hydrocarbon lubricant [112]. Even changing the property of the end group of the grafted layer can alter the nanoparticles’ dispersion ability. The Fe_3O_4 modified with the excess amount of oleic acid can disperse well in a non-polar solvent, but not in a polar solvent. Changing the end group of oleic acid to oleate would reverse the dispersion behavior, resulting in a good dispersion in polar solvent instead of non-polar solvent [217].

From Eq.3 and previous analysis on particle sizes, the thick surface layer was beneficial to the stability of nanoparticles. The study on TiO_2 with amine surfactant found that increasing the number of carbon atoms in grafted surfactant from 3 to 12 increased the dispersity in a non-polar solvent [110]. However, both the surfactant surface modification method and the surface modification method resulted in a surface layer with similar thickness [119,217]. The only method which had significantly thicker surface layer was the SI-ATRP method. This method could graft the longest chain on the surface of nanoparticles [45,50]. This explained the high stability of nanoparticles modified by this method. Even in temperatures lower than -20 Celsius, the nanoparticle dispersion could stay stable for more than 2 months [45,50].

3.3 Summary

Nanoparticle and fluid interaction. The dynamic nature of boundary slipping under a simple flow profile was measured with the prototype. With the limitation of the current instrument configuration, some interesting conclusions can be drawn. It showed that the boundary slipping took place in mineral oil and water with a flat surface. In the range of this testing, this slipping phenomenon did not dissipate energy, which is physically very probable, because boundary has no heat-capacity, and energy has no place to dissipate to. The fluid keeps a memory of all the shear forces exerted by the solid and as a consequence the fluid-solid interaction will be more complicated than the case in which the shear generated by solid can be dissipated.

Nanoparticles in a base oil. Theoretical analysis predicted that steric stabilization plays important roles in lubricating oils, more than other methods due to their non-polar nature. Stabilization can be provided by formulating oil with a dispersant or by modifying nanoparticles to form a surface organic layer. However, the use of dispersant was limited because it hindered the friction modifying ability of nanoparticles. To obtain good suspension, a long alkyl chain on the nanoparticle's surface with sufficient grafting density and thickness-to-size ratio are essential. Because of this, there were various techniques to disperse nanoparticles of different sizes in a lubricant. For particles with sizes under 50nm, using surfactants to modify a nanoparticle's surface can provide a good dispersion. For oxide particles larger than 10nm, surface silanization has a clear advantage because of its higher grafting density and ability of two step functionalization.

CHAPTER IV

PHYSICAL PROPERTIES OF WORKING LUBRICANTS[3]

In this chapter, the physical and thermal properties of working lubricants were tribologically evaluated. In order to probe the properties *in situ*, a new test apparatus was configured. The research described in this chapter has potential applications in electrical vehicles.

4.1 Physical properties

4.1.1 The electrical properties of lubricating oil

Rapid development in advanced technologies such as electrical vehicles and robots demands better *in situ* probing the performance of lubricants. [222–228].To date, understanding in properties of lubricants has been based on individual and standard measurements of fluidic performance such as viscosity,[229–231] film formation, [177,179,232] and frictional responds under shear[233,234]. The physical properties of lubricants, such as electrical conductivity, have not been well studied. One key reason is the lack of tools to probe a lubricant in working conditions.

Here we report an integrated approach to measure frictional behavior of lubricating oils while probing their physical properties. The electrical conductivity of lubricants was investigated *in situ*. We have previously conducted tribo-electrochemical study on mechano-oxidation of metals[18,21,235–237]. We are able to probe the oxidation and

---

[3] Part of this chapter is reprinted with permission from "Tribological Evaluation of Electrical Resistance of Lubricated Contacts." By Chen, Yan, and Hong Liang. Journal of Tribology 142, no. 11 (2020).

subsequent removal of surface materials. In the present work, we investigate the behavior of lubricating oils.

4.1.2 The measurement methods for lubricant physical properties

Two lubricants used in this study are light mineral oil (330779 Sigma-Aldrich) and commercially available engine oil (SAE 5W-30 PENNZOIL PLATINUM). The viscosity was measured at room temperature using an AR-G2 rheometer. The material used to fabricate two discs were E52100 steel from Mcmaster Carr.

We built a triboelectro system that measured the impedance of a lubricant while the friction was monitored. The configuration of this system is illustrated in **Error! Reference source not found.**. The system consists of a disc-on-disc metallic pair that were connected to an instrument with impedance measuring capability. The upper circular disc was stationary. A normal force was applied on the disc, while the lower disc rotated. The contact area was $17.80mm^2$. Impedance was measured at the frequency of 1MHz and a constant 1mV peak to peak voltage with a DC bias of 0.5mV. This system enabled *in situ* monitoring the thickness and electrical resistance of lubricants simultaneously.

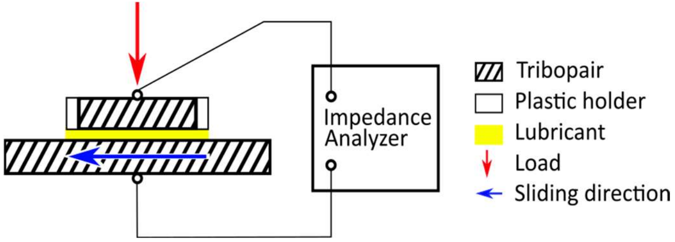

Figure IV.1 The configuration of electro-tribotesting system. The tribopair was connected to a tribometer and an impedance analyzer. The tribometer applied the load on the upper disc through an omnidirectional joint. The lower disc rotated under a controlled speed.

The thickness and resistance were obtained through a calculation based on impedance data. In the present study, the tribopair was considered as a capacitor and a resistor in parallel. The capacitance term was assumed fully contributed by the oil film which has a dielectric constant of 2.1[207]. Here was the formula of calculation:

$$R = \frac{1}{Re\left(\frac{1}{Z}\right)} \qquad (1) \qquad\qquad t = A\frac{\epsilon\epsilon_r}{Im(\frac{1}{Z})/\omega} \qquad (2)$$

where R is the resistance, Z is the measured impedance subtract the impedance of the shorted measuring system $Z = Z_{measured} - Z_{short}$, A is the nominal area of contact, $\epsilon\epsilon_r$ is the dielectric constant, ω is the angular frequency of the applied voltage. Re and Im takes the real and imaginary part of a complex number, respectively.

In order to obtain properties of the lubricating oil, the impendence measured was super imposed on the Stribeck curves, i.e., the friction against a grouping of $\frac{speed \times viscosity}{Load}$, as the Sommerfeld grouping[238] .

The precision of this measuring system can be inferred from the shorted system impedance. The standard deviation of the shorted measurement system was ~0.05Ω for both real and imaginary part of the impedance. The percision of film thickness measurement was dependent on the real part of measured impedance and film thickness. The analytical solution to that is difficult, but we can estimate this by Monte Carlo simulation method. The $Z_{real} = 10, 100, 1000\Omega$ was simulated with total 200 simulated experiments:

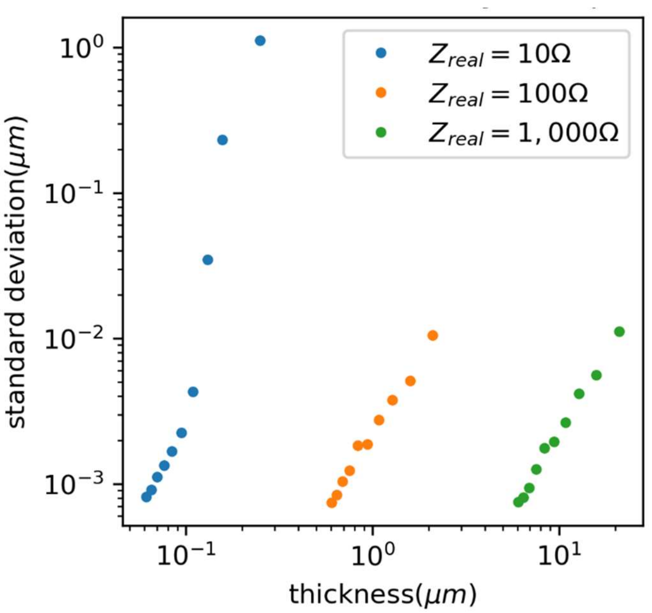

Figure IV.2 The Monte Carlo simulation on system precision.

The range of this measuring system was limited by the current measuring capability of our instruments. The high impedance can cause the current too low to detect. This instrument can measure 60pA current, thus it can detect maximum impedance of $16M\Omega$.

4.1.3 The stribeck curve of resistivity and oil film thickness

To evaluate the lubricating performance, Stribeck curves were generated using the coefficient of friction against the grouping parameters, as shown in FigureIV. 3. There are two curves shown in the figure. The upper (blue) is that of the mineral oil and the lower (orange) the engine oil. For both curves, three lubrication regimes can be identified, boundary, mixed, and hydrodynamic lubrication. Under a high load and low speed, the boundary lubrication was characterized by the high coefficient of friction. In this regime, the friction force was generated from the contacting asperities on opposing

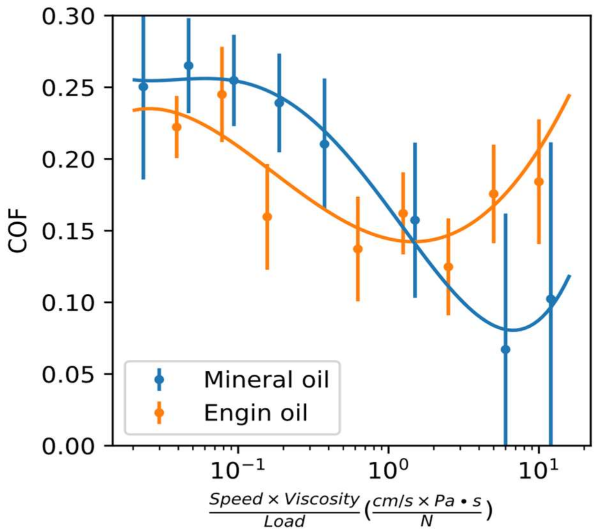

Figure IV.3. The Stribeck curve of two lubricants studied. The y-axis was the coefficient of friction and the x-axis was the dimensionless Summerfield number (S). The error bar in the plot shows the standard deviation of the measured friction coefficient.

surfaces[239]. With increased speed and lowering of normal load, the oil film started to form, resulted in a lower COF. On the right side of the plot, the hydrodynamic regime was reached with a complete oil film formed between to contact surfaces. The mineral oil data have high standard deviation at high grouping parameters, this is due to the combined effect of low frictional force and high speed. However, because the high number of data points collected (~6,000), it is still a good measurement of coefficient of friction. Here the commercial engine oil has lower coefficient of friction in the boundary lubrication regime indicating its effectiveness in protecting contacting surfaces.

The impendence during tribotesting was studied to obtain physical properties of a lubricant. Based on the measured impedance, the oil film thickness was calculated using equation (2). The electrical resistance was obtained using equation (1), Results are imposed on the Stribeck curve shown in Figure IV 3 and new results are shown in Figure VI 4. Figure VI. 4a is the measured oil film thickness under different speed and loading conditions. Figure VI. 4b is the electric conductivity of the lubricant against corresponding value. The mineral oil in high grouping parameter shows high standard deviations, this may be due to the high entrapment speed. According to Figure VI. 4a, the film thickness of both oils is similar. When a film is formed, as labeled by the dashed line, the engine oil seems to provide a bit thicker film that than that of mineral oil. Commercial lubricants are known to compose various additives that might be responsible for this. Details will not be discussed here. According to our data, the thickness of the oil film is well below $1\mu m$ in boundary lubrication regime and $10\mu m$ and thicker in otherwise. In Figure 3b, the electrical resistance also showed similar behavior at boundary lubrication regime. This figure also has one datapoints with a seemingly large error bar, it is caused by the log scaling of the y-axis. Interestingly, after an oil film was formed, the electric resistance was increased in a quadratic manner while the film thickness increased linearly

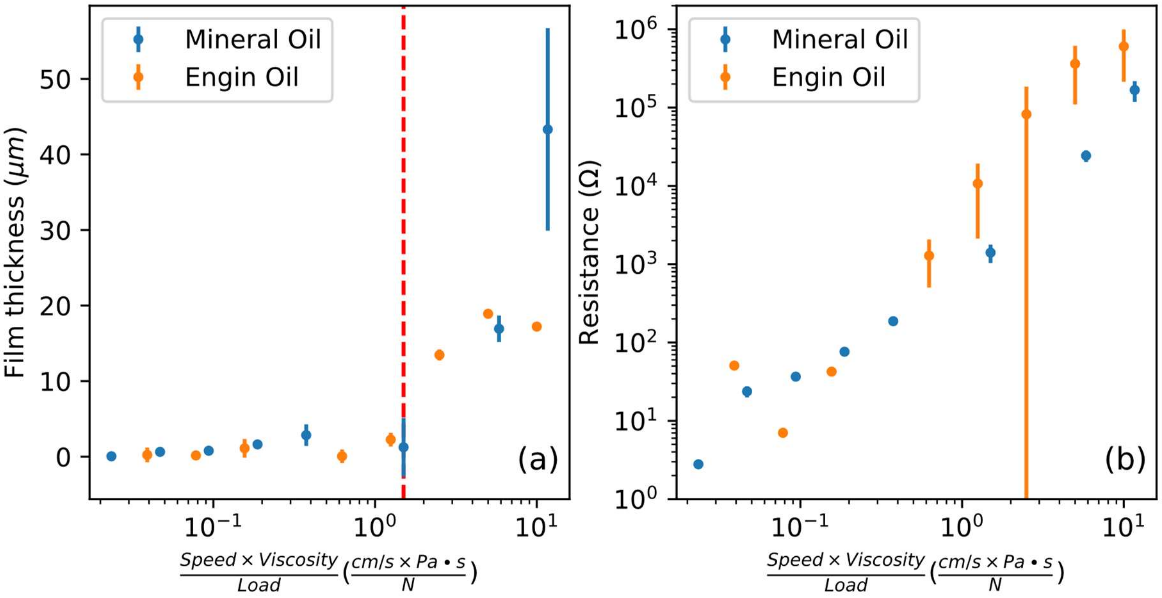

Figure IV.4.a) The calculated oil film thickness from electric impedance as a function of the grouping number of the Stribeck curve. b) The calculated resistance of lubricants as a function of the grouping number of the Stribeck curve. In both plots, the error bars are the standard error of the collected data.

against Sommerfeld grouping(Fitting the function $\log(R) = C_1 + C_2 \log(S)$, for mineral oil $C1 = 6.25 \pm 1.2$, $C_2 = 1.96 \pm 0.75$; for engine oil $C_1 = 8.68 \pm 1.18$, $C_2 = 2.28 \pm 0.88$) This indicated that the electric conductivity of the oil film under shear is not a simple ohmic behavior. The non-linear quadratic function of conductivity against the grouping under shear is intriguing. The correlation between those two measured quantities can be seen when they are plotted against each other in Figure IV 5. According to Figure IV 5, The film thickness in the boundary lubrication regime was less than $1\mu m$. The resistance was about 10kΩ when a complete film was formed. Once an oil film was formed, the thickness reached $20\mu m$ for engine oil and $40\mu m$ for mineral oil. For mineral oil the resistance increases exponentially to around 100kΩ. The mechanisms of such behavior are currently unknown. Previous study using numerical simulation reported that electrical tunneling between opposing surface asperities caused the non-linear increasement of conductivity when oil film was thin enough[240,241]. Our results seem to be beyond the scale of the previous study. In our case, the non-Ohmic behavior took place only after a film is formed where the film thickness reached beyond 10 μm. There are several questions raised from our results. Why does a lubricating film behave this way? How and why do two lubricants differ? We will report of our findings in near future.

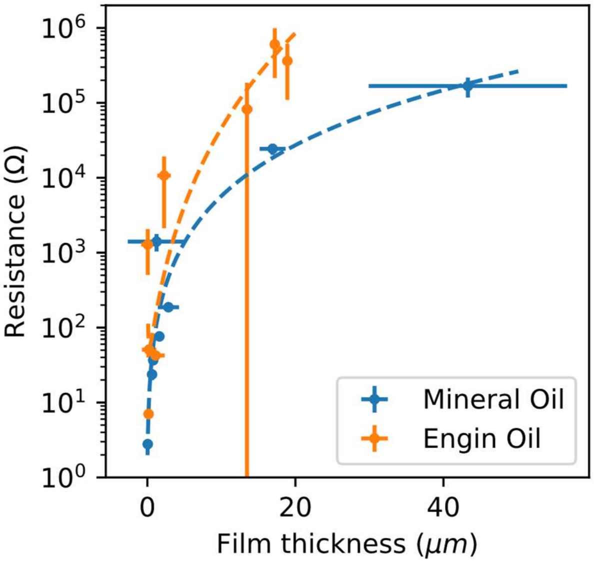

Figure IV.5. The electrical resistance is plotted against oil film thickness. There two distinguished regions: the linear relation at the lower left region and non-linear upper right.

4.2 Thermal properties

4.2.1 The thermal conductivity of lubricating oil

Recent advancement in electric vehicles (EV) requires lubricants with more or alternative properties [222,223,225,242]. Among these properties, thermal conductivity is one of the most important. Thermal conductivity is the ratio of thermal flux and thermal gradient[243]. It represents the efficiency of thermal energy flowing through a fluid. Thermal conductivity in EV lubricant is important because using high thermal conductivity lubricant can improve the efficiency of EV. The efficiency of electric motors used in electrical and hybrid vehicles have low efficiency when the temperature is high[244]. Therefore, a lubricant with higher thermal conductivity can improve the efficiency of electric motors. The thermal conductivity of the lubricating oil used in the drivetrain also impacts the overall thermal management of the vehicle[245,246]. The thermal conductivity can also influence lubricant performance, especially for high-slip and high-load conditions[247,248]. Having a desirable performance in such conditions is essential to EV which have high acceleration. However, there still lacks an effective method to measure the thermal conductivity of lubricating oil in its working condition. The measurement of thermal conductivity of a working lubricant is challenging. The recreation of tribological condition can be difficult. Some lubricants under a tribological contact can be subjected to pressures up to a few GPa [249]. High-pressure thermal conductivity was reported to be achieved by a measurement method called transient hot-wire method[182,250,251]. This method used a metal wire which was submerged in a pressurized lubricant. The temperature of the wire was increased by passing an electric current through and monitored via resistivity. An optical method called flash method was used to measure non-pressurized lubricating oil[252]. This method used a laser to heat up a small quantity of lubricant, while monitoring optically the thermal diffusion. However, none of these methods measured the thermal conductivity of a lubricating oil shear under high pressure. Despite prior effort, to date direct measurement of the thermal properties of a lubricant under shear has not been possible.

To probe the thermal conductivity of a working lubricating oil, the electrical response of contacting surfaces is essential. This electrical response measurement has been used to track tribochemical reactions and oil film thickness in prior works. The early study of both experimental contact mechanics[240,253] and tribochemical kinetics of tribofilm formation[173,175,180] was accomplished utilizing direct current (DC) resistant measurement. Use of high-frequency alternating current (AC) resistance measurement was later developed to measure lubricating oil film thickness under a ball-on-disc setup[177,180]. The impedance measurement has also been successfully implemented to monitor the tribochemical process of chemical mechanical planarization[18,21,235,236]. Our previous work on this subject measured the electric impedance of a disc-on-disc contact. Based on that measurement, the oil film thickness can be measured *in-situ* [254]. By combining this electric measurement of oil film with temperature control, the thermal conductivity can be inferred from the dimensional analysis.

To further investigate the thermal property of lubricating films, we configured a new thermally controlled tribotesting device. It measured the thickness of a lubricating film while imposing a thermal gradient into it. This thermal gradient was monitored with a thermocouple and correlated with the oil film thickness. A model to relate the measured quantity to the thermal conductivity of the lubricating film was proposed.

4.2.2 Testing the thermal property of lubricating oils

Two lubricants was used: light mineral oil (Sigma-Aldrich, St. Louis, MO) and PAO oil (Tesla, Palo Alto, CA). Both liquids were untreated before the test. The mineral oil was selected because it has a simple alkenes structure and is used as both lubricant and cooling oil. The PAO oil was selected because it has been widely used as a base oil for formulation. These oils are ideal candidates for our baseline study in this research.

All experiments conducted in this research used an integrated test system consisting of a modified tribometer (CSM Instruments, Needham, MA) and an electrochemical workstation (Gamry, Warminster, PA). This system was configured as an electrically and thermally monitored disc-on-disc tribotesting device (Figure IV.6). This system has one tribopair consist of two discs made from E52100 steel (Mcmaster-Carr, Atlanta, GA). The upper disc could move freely in the perpendicular direction. During experimentation, the lower disc rotated with a controlled speed and a force was applied on the upper disc with a dead weight. Detailed description of the system can be found in our previous publications[254].

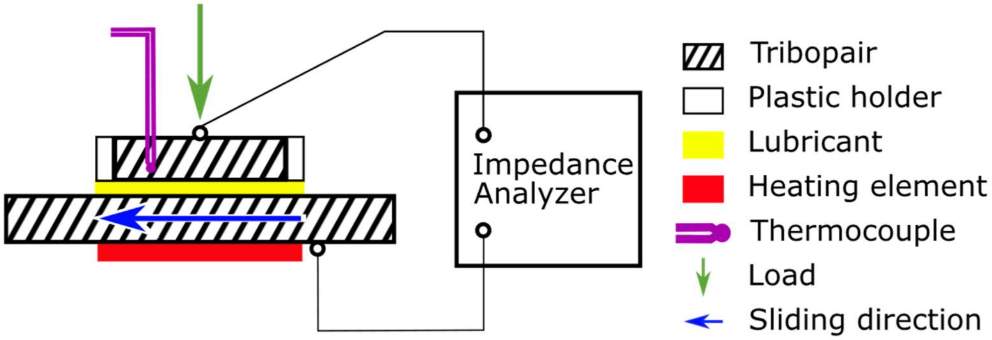

Figure IV.6 The setup of the measuring system. The Load was controlled with a dead weight. Thermocouple was attached on the tip of the lower

Temperature was controllable during experiments. A heating element was attached underneath the lower disc. During the experiment, the temperature of the lubricant was evenly increased by heating the element. This temperature increment was monitored using a thermocouple attached to the upper disc. The position of this thermocouple was about 0.5mm above the edge of the upper disc. In experiments, the temperature range was controlled from room temperature to around 320K. The temperature range was limited by the plastic materials used to construct this system.

The electrical impedance of this tribopair was monitored with an impedance analyzer. Impedance is a concept analogous to resistance under direct current but works in the alternative current. In this configuration, the electrical impedance was caused by the capacitance and resistance of the lubricating film formed during the tribotest. This capacitance and resistance can be calculated from the measured impedance. In all experiments, the impedance was measured at 1MHz. Based on the measured impedance, the lubricant film thickness can be calculated[254].

4.2.3 Lubricating performance against impedance

At a fixed temperature, the impedance of this system remains constant. Figure IV.7 shows the directly measured impedance at room temperature. This shows impedance value was unchanging when the temperature was fixed. Without temperature change, the electric response of the contacting surface was relatively stable.

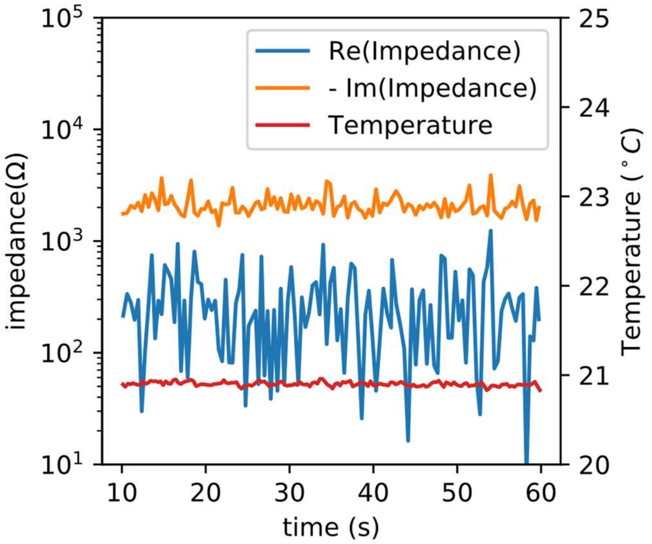

Figure IV.7 Figure 2. The measured impedance between contacting surfaces under isothermal condition. Both the real and imaginary part of the measured value did not increase or decrease with time.

In contrast to the isothermal condition, the change of temperature alters the electronic property of the oil film. To illustrate this, Figure IV.8 plotted the capacitance calculated from three different experiments under the same condition (1cm/s and 1N load). These three data sets all indicated that the capacitance of the tribopair was increased with the increase of temperature.

The impedance reflects the thickness of a lubricating film. In our recent study, it was found that the increase in capacitance was caused by the thinner oil film[254]. The tribopair in the testing system essentially formed a capacitor that was separated by the oil film. The capacitance was inversely proportional to the thickness of the oil film. It means that when the oil film became thinner, the capacitance would increase. This increment in capacitance was then measured using our system. By measuring this impedance versus temperature, the oil film thickness change was obtained.

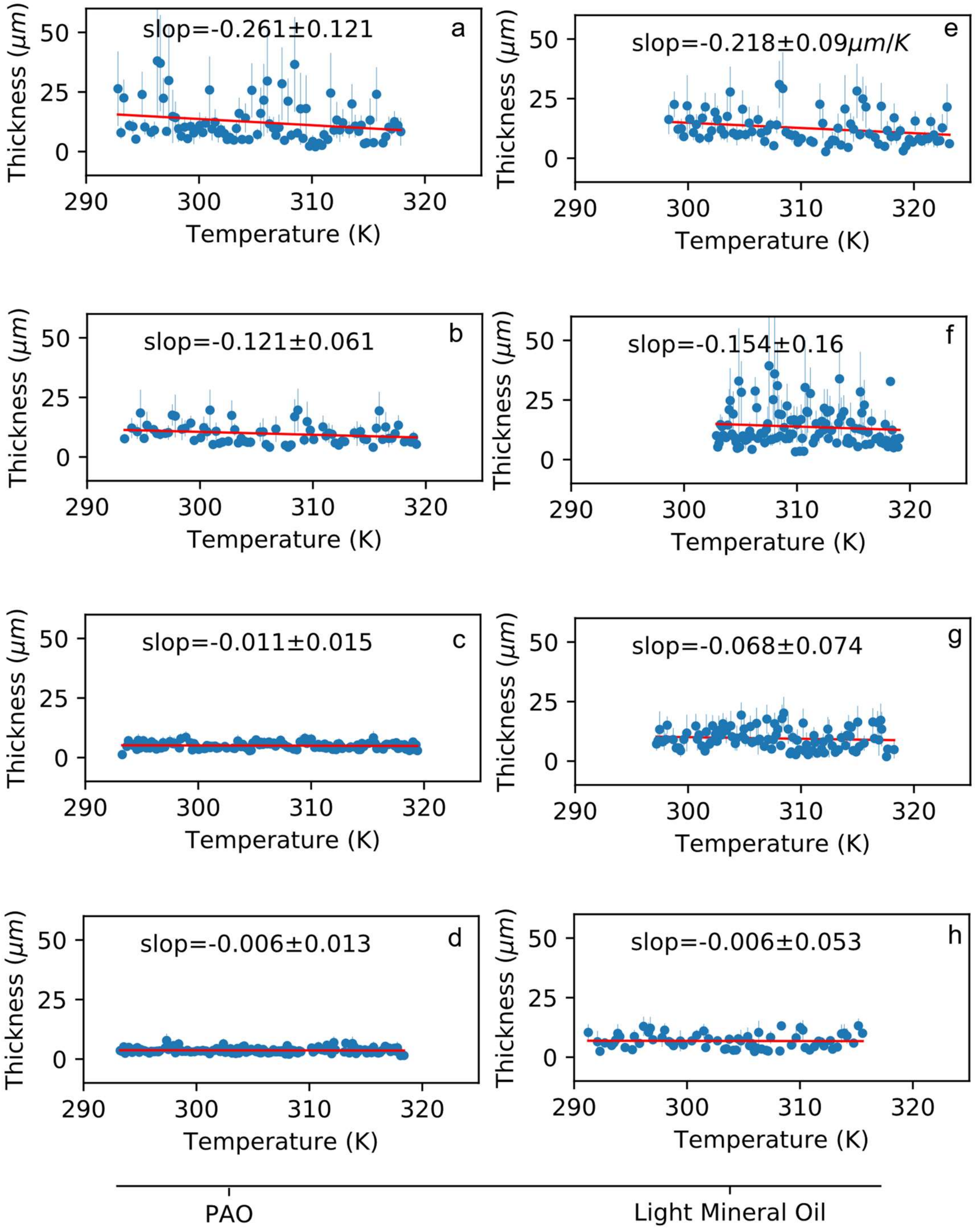

Figure IV.8 Figure 3. the oil film thickness vs. temperature of PAO(a-d) and mineral oil(e-h). The speed over load values of experiments are: a,e: 25cm/Ns; d,f:50 cm/Ns; c,g: 100 cm/Ns; d,h:200 cm/Ns

4.2.4 Effects of temperature on oil film thickness

The temperature and oil film thickness were proportionally correlated. In Figure IV. 9, the calculated oil film thickness was plotted against the measured temperature. Both the PAO and mineral oil film thickness decreased with the increase of temperature. These decrements were correlated with the Sommerfeld value. It appears that the thicker oil film that was generated under higher speed/load was more susceptible to change its thickness when the temperature rises. In order to characterize this correlation between temperature and oil film thickness, linear regression was performed on each data set. These linear regression results showed that there is a clear correlation between the change rate of film thickness and the Sommerfeld grouping value.

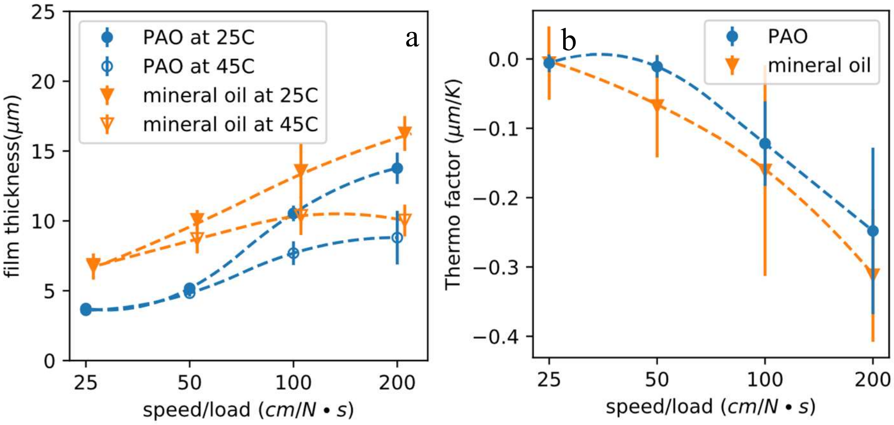

Figure IV.9 a) the oil film thickness vs. speed/load at two different temperatures. Both the value and the standard error in this plot was based on linear regression results. b) the measured slop (thermal factor) of the oil film thickness.

4.2.5 A new thermal factor

To understand our measurement, we correlated the Stribeck curve, the oil film thickness, and the changing temperature. In Figure IV 9, the oil film thickness of two lubricants at two temperatures was plotted against the Sommerfeld grouping. The film thickness at 25℃ was increased linearly with the increment of Sommerfeld grouping value. The film thickness at 45℃, however, shows a different trend, i.e., increasing gradually with the Sommerfeld grouping value.

In accordance with common Stribeck curves, the coefficient of friction increased with the oil film thickness. In figure IV 10, the Stribeck curve of the coefficient of friction was plotted against the Sommerfeld grouping value. Both lubricants show the increase of the coefficient of friction with the Sommerfeld grouping. Compared to PAO, the mineral oil, which has a thicker film, shows a high coefficient of friction. Both mineral oil and PAO were in the elastohydrodynamic regime to the hydrodynamic regime in all experiments.

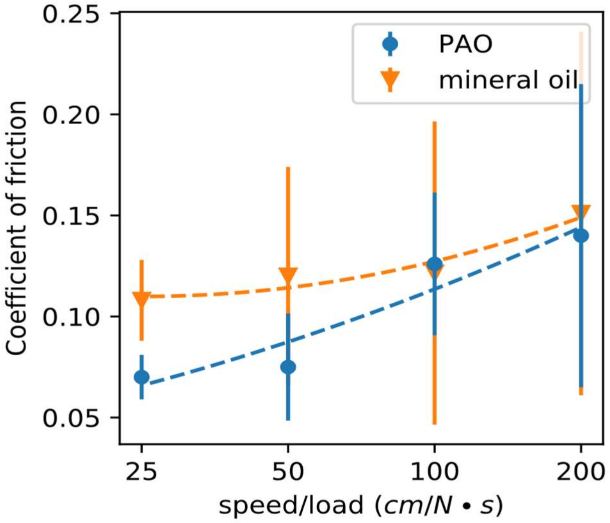

Figure IV.10 The coefficient of friction plotted against the Sommerfeld grouping (Stribeck curve). The dotted line shows a quadratic fit.

4.2.4 Dynamic thermal conductivity of a lubricant

A fluid dynamic simulation of the experimental system shows a constant pressure gradient under the upper disc. This simulation was based on a simplified 2-dimensional model. In this model, the fluid flowed between two parallel plates. The ratio of the plate's length and the distance between those two plates was 10 to 1. The fluid on the right side of the plate was ejected into the plates with the same speed as the upper plate. Using the SIMPLE algorithm with fipy software[255], this model's pressure field can be simulated. This pressure field was plotted in Figure IV.11. This simulation indicated under the upper disc, there is a constant pressure gradient along the flow direction.

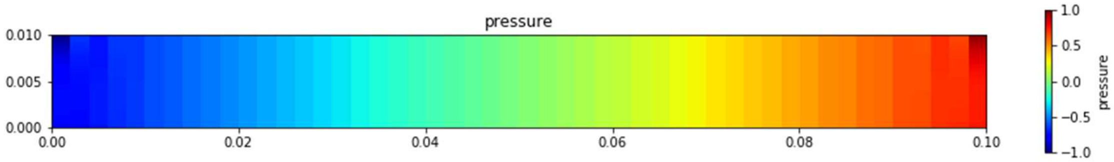

Figure IV.11 Figure 6. The simulated pressure field in a 2-dimentional model. The value of the pressure was normalized to from -1 to 1.

Based on this information, a relation between the film thickness D and the lubricant's viscosity was derived. A simple film thickness model can be calculated based on the assumption that there is a constant pressure gradient under the contact. Based on the Navior-Stocks eq. the flow between two parallel plates can be expressed as:

$$\frac{\partial^2 v_x}{\partial y} = -\frac{1}{\mu}\frac{\partial P}{\partial x} \tag{1}$$

where x, y is the location along and transverse the plan of contacting discs, P is the pressure, μ is the viscosity of fluid and v_x is the fluid speed along the x-axis. We can simplify this equation a bit by defining G = $\frac{\partial P}{\partial x}$.

It is known that the upper plate moved at a speed of v_0 with the lower plate stationary. Another observation is that because the liquid is squeezed into the gap between two plates, there should be a relationship:

$$v_x = -G\frac{1}{\mu}(y^2 - D^2) \tag{2}$$

where D is the gap between the plates, $v_x(0) = V, v_x(D) = 0$.

Assuming the pressure gradient under the pin is the same number, the force and pressure gradient can be related to:

$$F = 4\int_0^R (\int_0^{2\sqrt{R^2-z^2}} Gx\,dx)dz \tag{3}$$

Evaluating this function gives:

$$F = 4\int_0^R 2G(R^2 - z^2)dz \tag{4}$$

$$F = 4GR^3 \tag{5}$$

Combining equation (5) and equation (2)results in the relation:

$$D = 2\sqrt{\frac{R^3\mu V}{F}} \tag{6}$$

where R is the radius of the upper disc, V is the entrapment speed, and F is the load. Applying this equation to the experimentally measured results, the apparent fluid viscosity under the contact was calculated (Figure IV.12). The viscosity calculated from the data at 25C matches the viscosity of the lubricant. However, the viscosity at a higher temperature (45C) shows a dependency between the Sommerfeld grouping and apparent viscosity, indicating there are other factors influencing the oil film thickness.

All the analyses above assumed the thermal gradient was non-existent inside the oil film.

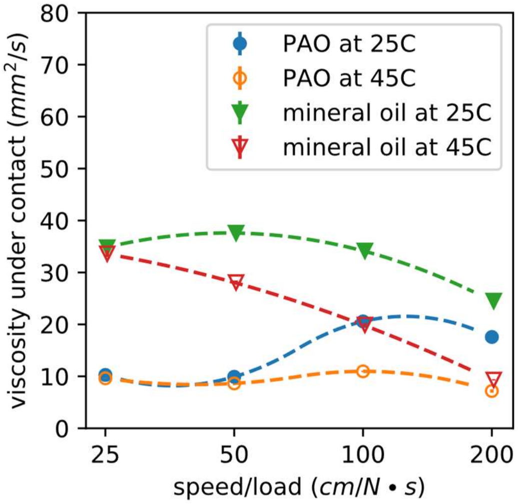

Figure IV.12 The calculated viscosity under the contact using eq. 6.

The film thickness can be considered to be a function of both viscosity and temperature gradient. Thus, eq. 1 can be rewritten as:

$$D = 2\sqrt{\frac{R^3 \mu V}{F}} + C_1/\nabla T \tag{7}$$

where C_1 is the factor relating thermal gradient to the measured film thickness. It is also known there is a thermal factor (TF) measured from the change of film thickness:

$$D = 2\sqrt{\frac{R^3 \mu V}{F}} + TF \times T \tag{8}$$

Comparing these two equations, the T and C_1 have the same dimension. Based on the dimensional analysis, the two factors are possibly connected. If such a connection is valid, that relation can be:

$$TF = A/\nabla T \tag{9}$$

where A is a scaling factor.

With this guessed relationship, an estimation of the thermal conductivity can be achieved. In figure IV 13, the thermal history of all the experiments was plotted against the experiment time. All experiments followed the same thermal history. The thermal flux can be roughly estimated with this data by considering the lower part of the upper disc was under the adiabatic condition:

$$q = \frac{dT}{dt} \times \frac{C_{steel}}{V_{steel}\rho_{steel}} \tag{10}$$

where q is the thermal flux, C_{steel} is the specific heat of steel, V_{steel} is the volume of the adiabatic region, and ρ_{steel} is the density of steel. The upper disc was held in a plastic holder. The low thermal conductivity of plastic combined with the short time validated the assumption of the adiabatic condition. This equation leads to a thermal flux of $1.71 \times 10^5 Js^{-1}$. According to Fourier's law, the temperature gradient is the function of film thermal conductivity:

$$q = -k\nabla T \tag{11}$$

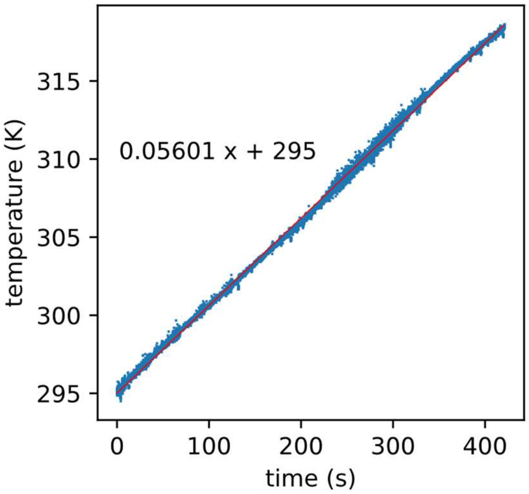

Figure IV.13 The measured temperature of all experiments was plotted against time. Red line shows a linear fit.

We know that the thermal conductivity of mineral oil should be around 0.136 W-m/K, and the thermal factor we measured is at $-0.3 \times 10^{-6} mK^{-1}$. Thus, we can do an order of magnitude estimate to guess there is a relationship between thermal gradient and thermal factor:

$$\nabla T = 0.1/TF \tag{12}$$

Then the apparent thermal conductivity can be estimated with:

$$k = -10TF\ q \tag{13}$$

To understand the thermal behavior of a lubricant, the data shown in Figure IV.9 was analyzed, and the dynamic thermal conductivity against the ratio of surface speed and the applied load was calculated. Results are shown in Figure IV 14. The plots have a similar shape to a Stribeck curve. In comparison with the Stribeck curve obtained at the same condition, it shows that at around 25 cm/N.s a fluid film was achieved, and the lubrication was confirmed to be in hydrodynamic lubrication regime. Yet the PAO has lower friction (Figure IV.13a) and lower dynamic thermal conductivity. This is understandable because of the additives in PAO as a base lubricant. When oil film is thicker toward to the right of Figure IV.10 (a and b), the friction and dynamic thermal conductivity both increases. In dynamic thermal conductivity, the difference in PAO and mineral oil is un-distinguishable. This is believed to be the general nature of organic molecules in both oils.

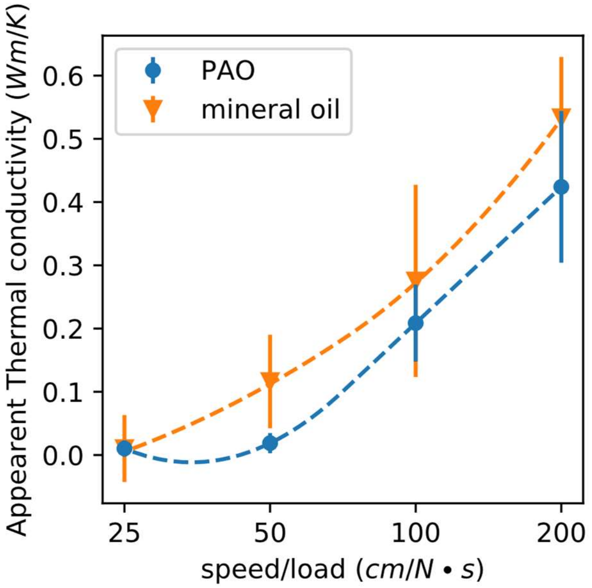

Figure IV.14 The approximated dynamic thermal conductivity plotted against the Sommerfeld grouping.

Now the question is why the dynamic thermal conductivity increases with the increase in the thickness of the oil film. This phenomenon was observed for both oils. Currently, it has been accepted that the thermal conductivity of lubricants depends on the molecular weight and molecular diffusivity of the lubricant[256]. It is also known that applying a high pressure can increase the thermal conductivity of the lubricating oil[257]. This means at the same speed, lower load led to lower thermal conductivity. Our results showed that the dynamic thermal conductivity increased with the Sommerfeld grouping number. On the other hand, the thicker the oil film the more conductivity it seems. There are several reasons for this, although currently not known. The molecules in an oli display augmented diffusivity under shear [258]. The nature of fluids, linear or turbulent flow [259] could affect the heat transfer of a fluid[260]. The molecular structure of the fluids themselves is expected to affect thermal conductivity as well. These will be investigated in future.

Another question arose as to why the PAO displayed lower dynamic thermal conductivity than that of mineral oil at around 50 speed/load. It can be attributed to PAO having higher molecular weight or lower molecular diffusivity. Since the most probable explanation was the mineral oil had a higher bulk modulus (1.3GPa) compared to PAO (1.2GPa)[261]. The speed of sound, e.g., the speed of a phonon that carries the thermal energy, is higher in the mineral oil [262]. Thus, mineral oil has a higher thermal conductivity when oil film was fully formed.

4.3 Summary

In this chapter, the feasibility to measure the thickness and electrical properties of lubricating oils using a tribo-electrochemical approach was proved. A specific configurate was developed to measure friction, electrical resistance, and oil film thickness simultaneously. Results indicated that both engine oil and mineral oil behave Ohmically during boundary lubrication regime. Once a hydrodynamic lubricating film is formed, the electrical resistance as a function of film thickness became non-linear indicating the change of film property.

This new integrated system was then configured to measure the thickness of a lubricating oil with temperatures ranging from 295K to 320K. The *in situ* characterization was achieved by electronically measured impedance value, resulting the knowledge of thermal properties of lubricants during tribotesting.

Results showed that impedance measurement could be used to study the thermal behavior of lubricants. Using the dimensional analysis method, the term dynamic thermal conductivity was discovered by comparing the correlation between lubricant film thickness, temperature, and thermal conductivity. Our results showed that PAO had lower dynamic thermal conductivity compared to mineral oil. The reason is not currently known. The dynamic thermal conductivity increased with the Sommerfeld grouping number. This could be attributed to the structures of molecules in oils, augmented molecular diffusivity under increased shear, and the nature of fluids. The mechanisms will be investigated in the future.

CHAPTER V

TRIBOCHEMICAL INTERACTIONS IN NANOLUBRICANTS

This chapter addressed the tribochemistry of nanolubricant. First, a short review of tribochemistry including tribochemistry kinetics was provided. Then, a novel nanolubricant's tribochemical property was studied with the *in situ* impedance method. This nanolubricant's synthesis and tribochemical process was studied.

5.1 Tribochemical reactions in lubricants

5.1.1 A brief history of tribochemistry

Additives are essential components in high-performance lubricants[1,138,263]. The best way to prevent wear and reduce friction is to separate the contacting surfaces in moving parts. Fluidic forces can carry out this separation at sufficiently high speeds and low loads, or with a tribochemically formed film[3]. The tribochemically active additives can separate the surfaces in the boundary lubrication regime by forming solid or viscous thin films[3,264]. These tribochemical reactions can significantly improve the overall performance of a lubricant. In some conditions it can even make macroscale superlubricity possible[265,266].

Products induced by tribochemical reactions due to additives develop a thin film called the tribofilm[3,4]. This tribofilm was first found in zinc dithiophosphates(ZDDP)[4]. Initially, ZDDP was used as an anti-corrosion additive in lubricating oil[267]. It was later found that lubricant with ZDDP added to it produced a thin film on lubricated surfaces. This thin film increased the wear resistance of lubricated surfaces despite its mediocre friction behavior[268]. Later, other additives that could also tribochemically form thin films with different tribological behaviors were found[1,24,269,270]. In Figure V.1, the development of a few widely reported additives was shown chronically.

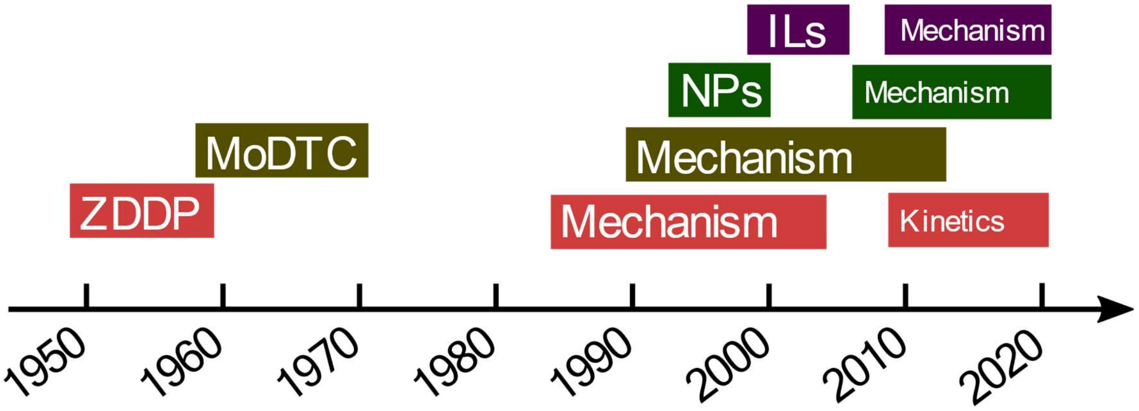

Figure V.1 The development of tribochemically active lubricant additives, their reaction mechanisms and uunderlying thermal dynamic principals.

Understanding tribochemical reactions has evolved since the 1980s (Figure V.1). ZDDP was the first lubricant additive whose tribochemical process was studied. The importance of tribological conditions was also discovered in early reports. From the late 1980s to 1990s, new surface characterization methods greatly improved the understanding of tribochemical reaction mechanisms. This also improved the understanding of other tribochemically active lubricant additives such as molybdenum dithiocarbamate (MoDTC). In the 2000s, the popularization of molecular dynamics methods further improved the elucidation of tribochemical reaction mechanisms. The development of two novel lubricant additives, ionic liquids and nanoparticles, also occurred in this decade, although their reaction mechanisms were not studied until the 2010s. During this time, the kinetics of tribochemical reactions also started development.

However, that research mostly focused on the reactions of ZDDP. Tribochemical reactions of lubricant additives were also studied in a case-by-case manner. To date, no universal principles or reaction routes have been proposed for all the tribochemically active lubricant additives. By reviewing the tribochemical process of these lubricant additives, their common features can be summarized. The result of this review will help the development of more effective lubricant additives.

5.1.2 The thermodynamic aspects of tribochemistry

Thermodynamic principles are the foundation of understanding chemical reactions. The term Gibbs free energy is commonly used to determine if a reaction is possible at a controlled pressure. This term can be used to analyze the tribochemical reactions of lubricant additives since they are under a controlled contact pressure. When the Gibbs free energy change of a reaction is negative, the reaction is considered spontaneous. The analyzation of Gibbs free energy (ΔG) often breaks it down to two parts: the change of entropy (ΔS), and the change of enthalpy (ΔH)[271]:

$$\Delta G = \Delta H - T\Delta S$$

Here the change of enthalpy can be interpreted as the energy change due to the alteration of chemical bonds or material structures. The change of entropy represents the energy penalty for making the system more ordered under a certain thermal agitation (a more detailed and physically strict interpretation can be found in many thermal dynamic textbooks). This equation states that at a fixed pressure, a reaction is possible when the thermal energy released by changing the chemical structures and atomic orders exceed the energy of thermal agitation. In Figure 2, an example of Gibbs free energy of ZDDP and tribofilms was plotted[272]. It shows the Gibbs free energy of polyphosphoric tribofilm is lower than ZDDP. This means the reaction of tribofilm formation is thermodynamically possible.

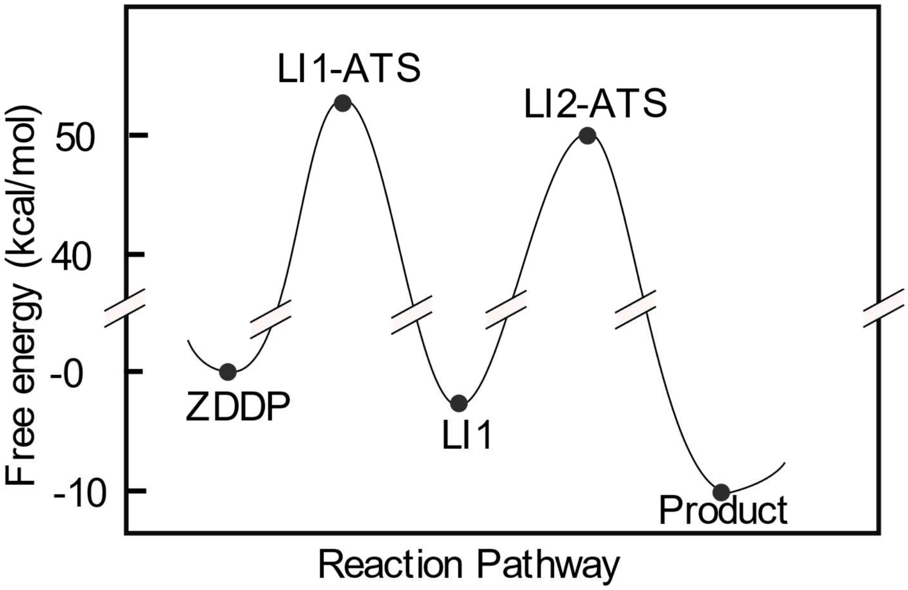

Figure V.2 The calculated Gibbs free energy of ZDDP's tribochemical process[278]. (Figure was re-plotted from the source)

The chemical reactions during tribological contact cannot be fully described by thermodynamics theory in equilibrium or reversible state. These tribochemical reactions of lubricant additives have three unique conditions that demand modification of the Gibbs free energy: the surface energy from the interface of lubricant and lubricated materials, the thermal and mechanical agitation from the friction force, and the change of free energy induced by shear strain. Here, the influences of these three factors are discussed.

Surface energy must be considered in tribochemical reactions because these reactions are confined to a small space. The tribological lubricant film has a thickness of a few microns, and the boundary films are on the submicron scale. The contact between asperities allows the reactions to happen in a space only a few atomic layers thick. In all three conditions, the surface-to-volume ratio is too high to not be considered. To account for the surface energy, the Gibbs free energy equation need to be modified to:

$$\Delta G = \Delta H - T\Delta S + A\gamma$$

where A is the contact area and γ is the surface tension between lubricant and contacting surfaces.

Surface energy is the cause of the adsorption of lubricant additives. In the tribochemical reactions, the surface (interface between oil and metal solid) area is constant. Hence, we only need to consider the change of surface tension γ. The adsorption of lubricant additives occurs because it lowers the surface tension on the lubricated surfaces. All tribochemical reactions reviewed in this paper started with the adsorption process. For example, ZDDP can be chemically adsorbed on metal and metal oxide surfaces through the ion exchange process. The room temperature Ionic liquids (ILs) can be adsorbed on the metal surface via electrostatic forces. Water molecules adsorbed on a silica surface can even lead to ultra-low friction through tribochemical reactions[273].

Another less frequently discussed effect of surface energy on tribochemical reactions is its effect on lubricant and lubricant additives. When confined between two nascent metal surfaces, ILs can transform from fluid to viscous solid. The solid phase of IL has lower metal-IL interface energy compared to the liquid phase, promoting this transformation. The friction force is dissipative, meaning the energy created by $f \cdot distance$ is dissipated from the contact to the surrounding materials. This can create a large thermal gradient[274–276]. Under dry sliding, this thermal energy can even change the microstructure of the contacting metal [275]. In the case of boundary lubrication or single asperity contact, this thermal gradient is considerable[274]. This friction energy can increase the local temperature at the contact region, which can change the fluid film thickness in the elastohydrodynamic lubrication regime[277]. For tribochemically active lubricant additives, the localized temperature can increase its reaction rate. The very localized high temperature also creates a large thermal gradient. This can cause the diffusion of molecules along this thermal gradient or polarization of some molecules[278].

To analyze the influence of shear stress, extended irreversible thermodynamics can be used. The major "extension" these thermodynamics make is the re-introduction of the concept of "space". In equilibrium thermodynamics, the systems we analyzed were all ambiguous entities without a clear shape or position. The extended irreversible thermodynamics studies a "space" that has positions. Assigning external quantities such as entropy, free energy, volume, and chemical compositions to a "position" creates two new things. One is the "flux" such as energy flux and diffusion flux of matter. The entropy, being a non-conservative quantity, has an explicit "rate of production" and entropy flux (heat flux). Similar to the extensive quantities turned into fluxes, the introduction of positions makes intensive quantities turn into "forces." The second equation of thermodynamics was reinterpreted here as "the fluxes and the forces must make the entropy production be positive." The flow of liquid under shear stress inside the tribological contact creates an open system. This open system can be analyzed in the same way as the thermal gradient by creating a "flux" term.

The shear stress can increase the free energy. A rough analysis can lead to a new equation of Gibbs free energy:

$$\Delta G = \Delta H - T\Delta S - V\Delta J_{flow}(\tau_{visco})^2$$

where V is the volume and J_{flow} is the steady flow compliance defined as $J_{flow} = \frac{G'}{G''^2}$ when the frequency is 0Hz[279]. The G' and G'' is the storage and loss component of the shear modulus G, respectively. This equation tells us creation of a matter with a higher storage modulus is favored under a high shear stress.

5.1.3 Kinetics of tribochemical reactions

Tribochemical reactions can be triggered by frictional heat and/or triboemission. When there is sliding between two contacting surfaces, the frictional force can generate a significant concentrated force which creates a phenomenon called frictional heat. Triboemission is the emission of electrons, charged particles, and photons caused by abrasion[280]. These emitted particles can promote electrochemical reactions and act as catalysts [281–283]. The effect of triboemission, typically the triboemission of charged particles, is essential to the tribochemical reactions in the boundary lubrication regime[281].

Without triboemission, the shear force can change the kinetics of tribochemistry as well. Experiments conducted with atomic force microscopy (AFM) show the simple pulling force is sufficient to trigger the disulfide bond reduction[284]. The force applied to the molecules deforms the molecular structures, thus changing the reaction characteristics. This can be modeled as the change of activation energy. In the tribochemical reactions, this mechanochemical process occurs on the molecules adsorbed on the contacting surfaces that are distorted by the shear stress between two contacting surfaces[285]. Strain on the molecule can directly change the kinetics of reactions. Thiol/disulfide exchange reaction's reaction rate can be controlled by stretching the disulfide bond with AFM[284]. It was found that the reaction rate of this reaction increases exponentially with the applied force. Activation energy was shown experimentally to reduce by 8.2kJ/mol under 400 pN force on the S-S bond[284]. In addition, the effect of force and temperature also indicated the force applied on the S-S bond changes its activation energy[286]. The reaction rate can be expressed as the Arrhenius equation[286]:

$$r = A\,\mathrm{e}^{\frac{E_a - F\Delta x_r}{k_B T}}$$

where A is the pre-factor, F is the force applied on the bond, E_a is the activation energy, k_B is the Boltzmann's constant, and Δx_r is a factor with a dimension of length. A direct result of this relation is that pulling of the molecule increases the reaction rate in a similar manner to increasing temperature, as shown in Figure V.3[286].

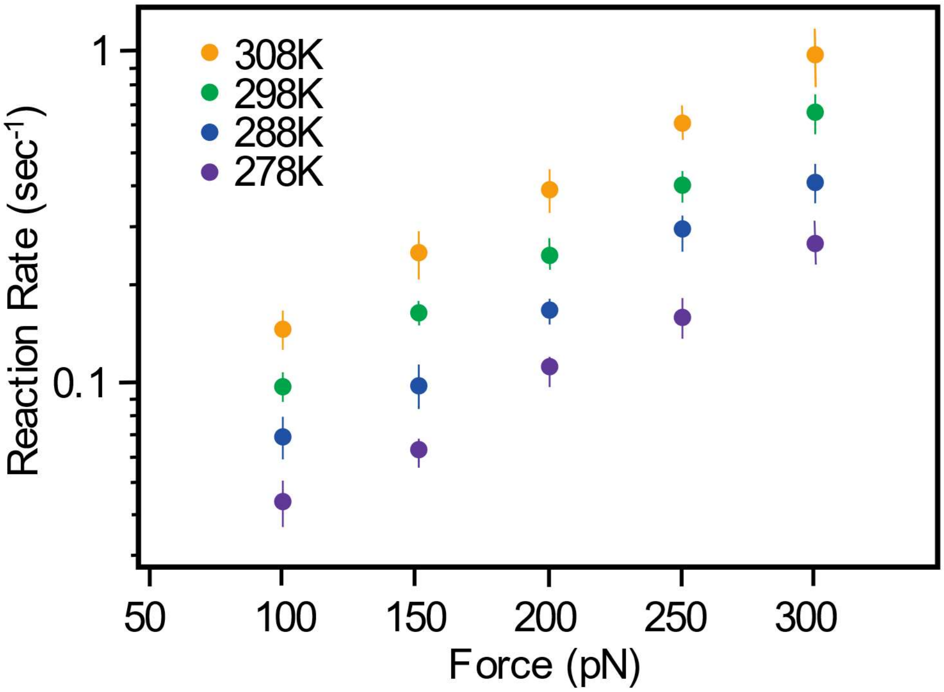

Figure V.3 The reaction rate of S-S bond reduction under the influence of force and thermal energy[292]. (Figure was re-plotted from source.)

Mechanochemical effects on reaction rates not only applied to the molecules directly pulled by AFM but also on the surface adsorbed molecules under shear[285]. Similar to the direct pulling of the molecules, the reaction rate increased with the increase of applied shear force. In the studies of methyl thiolate decomposition activated by shear force[285], molecular dynamic simulation shows that the adsorbed molecules experienced a normal force under constant shear. This normal force was distributed on the surface molecules, changing their chemical reactivities.

The microscopic origin of this activation energy function shift under shear is the change of bond length distribution. Figure 4 displays the calculated bond length distribution of a surface-adsorbed allyl alcohol molecule[287]. This shows the bond length distribution "flatten" during sliding, decreasing the energy required for bond breakage. The change of molecular configuration under shear force can also transfer the atoms on the contacting surfaces and make it react with the adsorbed molecules[288].

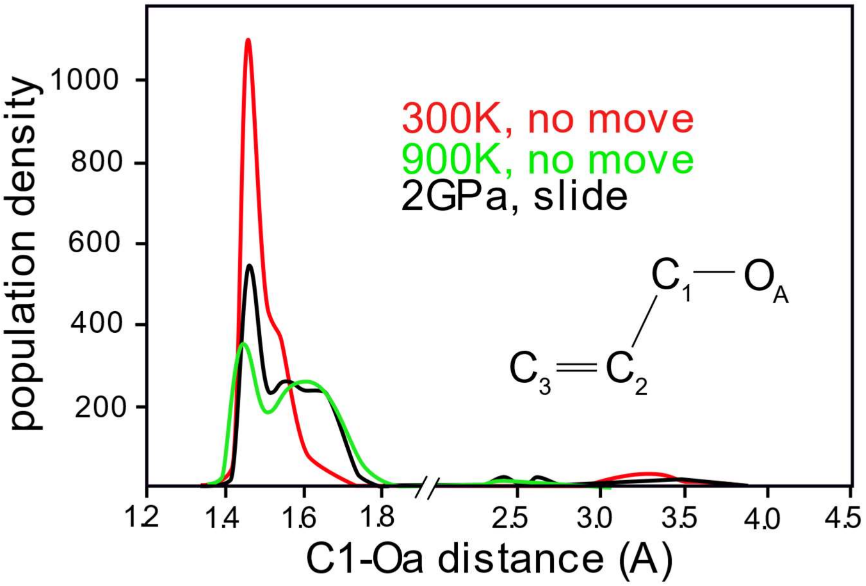

Figure V.4Figure 4. The bond length distribution of a C1-OA bond in adsorbed allyl alcohol under room temperature, 2GPa shear stress at room temperature, and high temperature[293] .

The kinetics of tribofilm growth can also be modeled as an Arrhenius equation[289–291]:

$$\left(\frac{\partial h}{\partial t}\right)_g = \Gamma_0 e^{\frac{\Delta U_{act} - \tau \Delta V_{act}}{k_B T}}$$

where Γ_0 is a pre-factor and τ is the shear stress defined by $\tau = \mu p$. In order to make the grouping $\tau \Delta V_{act}$ have the same dimension as energy, the ΔV_{act} has the same unit as a volume. It is called "activation volume" in some texts.

In some other literature, this equation takes another form[18]:

$$\left(\frac{\partial h}{\partial t}\right)_g = \Gamma_0 e^{\frac{\Delta U_{act} - \Delta E}{k_B T}}$$

In those papers, a term called mechanical energy input is defined. Since this "mechanical energy" term is linearly proportional to the shear stress defined above, these two definitions are mathematically identical.

This simplistic model cannot explain some phenomena in tribofilm growth. The Arrhenius equation will always produce a positive growth rate, which is not true. For example, the growth of ZDDP tribofilm can be described with three phases: growth, slight decrease, and then stabilized at a certain thickness. Even in the stable growth phase, the growth rate of tribofilm is not constant[292]. For the mechanisms which limit the thickness of tribofilm such as wear, consumption of iron must be considered.

The deviation from the simple Arrhenius behavior can be explained by three factors. First, shear stress or mechanical energy input is not a constant factor during the growth of tribofilm due to the evolution of contact pressure[289,293]. Second, the growth of tribofilm may require multiple steps; each has a different activation energy and activation volume[272]. Third, tribological forces also cause wear of the generated tribofilm. The balance of these three mechanisms have made the modeling the tribochemical process difficult[289].

5.1.1 Tribochemical reactions of nanolubricants

Nanoparticles (NP) have been used as additives in lubricants to enhance their tribologial performance [1,294]. Stable dispersion has been achieved in nanolubricants [294]. Like other additives, the NPs can be adsorbed on the contacting surfaces. This adsorption is driven by Van der Waals's interactions between the NPs and the surfaces[1,5]. In some cases the adsorption of NPs can directly reduce the friction in the boundary lubrication regime and protect the surfaces from contacting[6,7]. However, with the tribochemical reactions the NP additive can have better tribological performance.

For some NPs such as metal oxides NP, there are no tribochemical "reactions" because the composition of the tribofilm they form has the same composition as the NPs. They are essentially sintered to the contacting surfaces by the tribological process[8–15]. There is also a report on tribochemically active oxide NPs such as Fe_3O_4. The metal elements can be reduced and/or oxidized via tribochemical reactions[16,17]. This oxidation reaction promoted by the oxide nanoparticles is essential to the chemical-mechanical polishing process[18–22]. In these reactions, the nanoparticle tribochemical reactions chemically wears the surface instead of protecting it. The overbased detergents are NP lubricant additives that can effectively reduce wear by forming a tribofilm[23,24]. This NP is also tribochemically inactive. The formation of its tribofilm is mechanical rather than chemical[24]. The capped metal NPs can reduce wear and friction without tribofilm formation[25]. In some cases such as copper NPs[26] and silver NPs[27] the tribofilm can form directly by mechanical cold welding. One exception to the capped metallic NPs is the dodecanethiol-modified Palladium NPs. The dodecanetiol capped Palladium forms palladium sulfide on the contacted surface when used as a lubricant additive[28]. The rare earth-containing nanoparticles can form iron oxide tribofilms through the oxidation-catalysis effect[29].

One of the most successful NP friction modifying additives, inorganic fullerene molybdenum disulfide (IF-MoS_2) has its friction modifying ability due to its tribochemical reactions. MoS_2 is known to be a solid lubricant as a powder or additive[30]. Under tribological forces, the IF-MoS_2 forms a tribofilm comprised of 2H-MoS_2 and chemically bonds to the iron oxide on the steel surface[31]. The mechanism of this reaction was proposed that the mechanical breakdown of IF-MoS_2 nanosheets can tribochemically bond to the iron/iron oxide[31]. The iron sulfide can also be found in the tribofilm formed by MoS_2 and WS_2 NPs[32,33]. The MoO_3 nanoparticles can tribochemically react with oleyfin polysulphide to form MoS_2[34,35]. The molecular dynamics simulation also shows that MoS_2 nanosheets were more stable between contacting surfaces compared to the amorphous phase[36].

The WS_2 tribochemical process creates a film with a layered structure. The top layer of WS_2 tribofilm is a mixture of WS_2, WO_3, and iron oxides (Figure V.5)[295]. The bottom layer is comprised of the reduced W and Fe. Unlike oxides nanoparticles, WS_2 can actively react with iron and iron oxide, forming oxides and even W metal. Here, the similar "surface concentration" phenomenon observed in MoDTC is found. The formed metal disulfide seemingly gravitates towards the contacting surface.

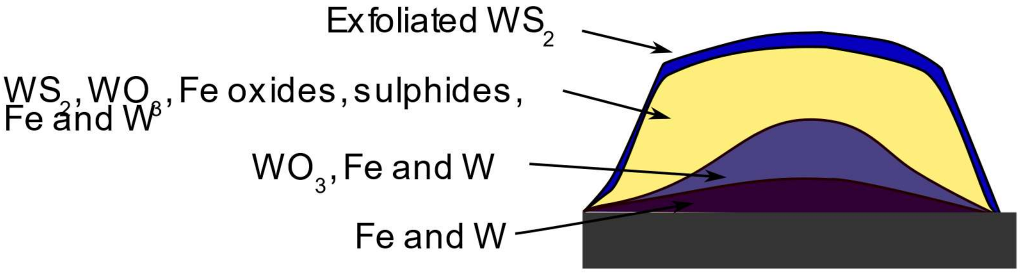

Figure V.5 The cross-section of tribofilm formed by WS2 NPs(Figure was based on [301]) .

The surface-adsorbed nanoparticles, when mechanically broken by the tribological processes, can produce some active materials due to the resultant high surface area. This can explain why the sulfur or phosphorus containing NPs, while having low hardness, can greatly improve the boundary lubrication performance of a lubricant[1]. The nanosheet of MoS_2 can readily react with iron and iron oxide[31].

Similar to ZDDP and ILs, different elements act differently in NP tribochemical reactions. When the NP contains nitrogen or phosphorus, the product of the tribochemical reaction is mainly nitrides and phosphide[296,297]. Similarly, CaF_2 NP and ZnB NP form FeF_2 and Fe_2B when tribochemically reacting with a steel substrate[102,298]. The α-ZrP nanoparticles which contain phosphorus forms iron phosphate which protects the surface from wear[299–301]. Carbon in NPs stays tribochemically inactive to metal surfaces. When graphene quantum dots were used as an additive, they tribochemically formed a fullerene structure instead of reacting with the contacting surfaces[302]. The $CaCO_3$ formed a tribofilm comprised of $CaCO_3$ and the CaO, and the carbon was removed from the NPs during the tribochemical process[100].

Interestingly, the DDP-coated ZnS nanoparticles tribochemically formed a film similar to ZDDP[303].

With a proper catalyst, the normally tribochemically inactive carbon can tribochemically form carbon nanostructures. Carbon-based NPs under the tribological force can form a glass phase with an amorphization process when mixed with iron NPs[304]. The tribological forces also reduced the Gibbs free energy of structurally more complex phases. This led to a phase transformation from the amorphized phase to onion-like carbon[304,305] or carbon nanotubes[306]. This process started with reactions between iron NP and graphite[304], which formed an amorphous carbon-containing iron carbide. The amorphous phase under tribological forces then transformed into onion-like carbon with superior tribological properties. It appears that the reason behind the inactivity of the alkyl chain in all the lubricant additives is caused by the strong carbon-carbon bond. The addition of iron disrupted this bond and made carbon tribochemically active.

The tribochemical process is essential to the lubricant additive functions, especially its anti-wear and friction modifying properties. This section reviewed the thermodynamics and kinetics of the tribochemical processes involving lubricant additives. Tribochemical reactions started with the adsorption of reactants to the contacting surfaces. The tribochemical reactions in nanolubricant greatly depended on the tribochemically active elements, Phosphorus, sulfur, fluorine, and nitrogen. The carbon is unlikely to be included in the final product. For a tribochemical reaction, it is likely that, the occurrence of the tribochemical reactions requires chemical or physical adsorption of lubricant additive to the contacting surfaces.Most reaction products were amorphous in nature. The only exception was transitional metal sulfide. This forms a 2D nanosheet which gravitates to the contacting surface.A tribochemical reaction is thermodynamically controlled by a force applied to the additive covalent bond. Such a force changes the free energy of the reactant and the product. The kinetics of tribochemical reactions are affected by the temperature, shear stress, and the wear of the tribofilm.

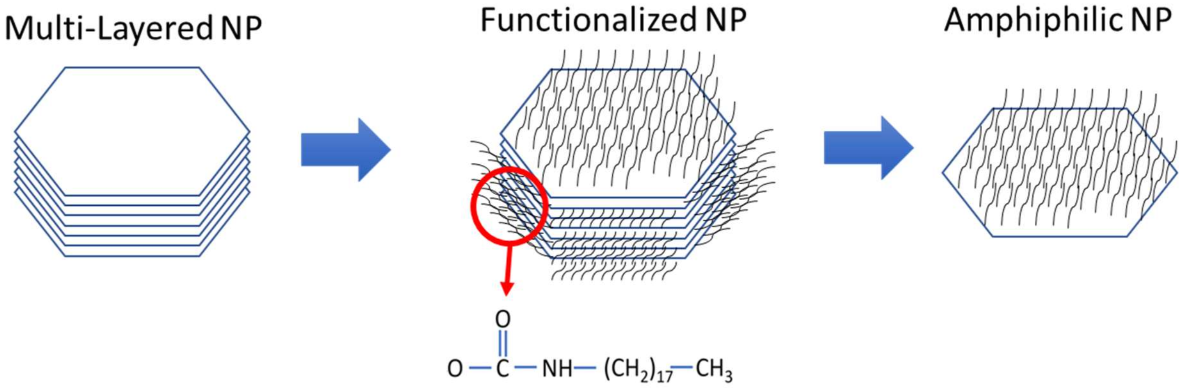

Figure V.6 The synthesis process of amphiphilic ZrP (a-ZrP)

5.2 The tribochemical of amphiphilic nanolubricant

5.2.1 The synthesis of a amphiphilic nanolubricant

Janus or gemini nanoparticles shows similar amphiphilic properties as the traditional anti-wear additives and organic friction modifiers. Those particles has inhomogeneous surface functionalizations[307,308]. The surface of such particles is partially hydrophobic and partially hydrophilic. This made them good candidate for forming emulsifications and potentially good lubricant additives with enhanced tribochemical reactions.

The nanoparticle synthesis has three steps, the synthesis of the core nanoparticle, the surface modification and the exfoliation (Figure V.6). The α-ZrP have a layered structure. Each layer's surface was covered with hydroxyl group (hydrophilic). The surface functionalized with alkyl chains becomes hydrophobic. By exposing the hydroxyl group between layers with exfoliation, the amphiphilic NP was synthesized.

The core nanoparticle α-ZrP was prepared with reflux method. First, 6g of zirconyl chloride octahydrate (ZrOCl2·8H2O, Sigma-Aldrich, St. Louis, MO) was mixed into 50 mL of 12 M phosphate acid (Sigma-Aldrich, St. Louis, MO). The mixture was loaded in a reflux system consisted of a 100-mL round flask and condenser. This system was heated to 94°C in oil bath and kept for 24 hours. The product was washed with deionized(DI) water three times, and dried in a drying oven.

The prepared α-ZrP was then functionalized with octadecyl isocyanate (ODI, TCI American, Portland, OR). The reactions in this process cannot happen under the presence of water. Thus, a second drying process is required right before the functionalization. In this drying process, the nanoparticles were left in an drying oven overnight and used immediately afterwards. The nanoparticle was then transferred into dry toluene in a flask with a magnetic stirring bar (without stirring) after preheating this toluene to 90°C with oil bath. This flask was then flushed with nitrogen gas for 10 minutes. ODI solution was prepared by adding ODI into dry toluene. Under nitrogen protection, this solution was added into the flask. The final molar ratio between α-ZrP and ODI was 10:1. The system was then flushed with nitrogen gas for another 20 minutes to continue driving out the moisture. After this process, the mixture was stirred under protection for 24 hours. The functionalized product was then washed with methanol for three times and dried in a 70°C oven.

The amphiphilic NP were obtained by exfoliating the product with tetrabutylammonium hydroxide (TBA, Sigma-Aldrich, St. Louis, MO). Mixing the functionalized ZrP with 40% TBA in DI water at room temperature the NP can be exfoliated. The molar ratio between ZrP and TBA were 1:1. The product was then freeze dried (FD-1A-50, Beijing Boyikang Laboratory Instruments Co., Ltd., China) at 50 °C (~15 Pa) for 48 h.

The nanolubricant was produced by mixing the amphiphilic NP with light mineral oil (Sigma-Aldrich, St. Louis, MO). The NPs were directly added into the light mineral oil and treated with ultrasound for four hours until a homogeneous dispersion was obtained. The concentration of NP in light mineral oil was 0.1wt%.

5.2.2 Tribotesting and characterization of the nanolubricant

Tribochemical study was conducted with a tribtesting system which combines a tribometer (CSM Instruments, Needham, MA) and an impedance analyzer (Gamry, Warminster, PA). The tribometer was configured as a disc-on-disc testing device (Figure 2). Two E53200 steel discs (Mcmaster-Carr, Atlanta, GA) connecting to the impedance analyzer were used as a tribopair. The temperature was controlled with a heating element under the lower disc. This system can characterize the tribological process and change of resistance *in situ* [254].The tested oil was placed between two discs before the testing. The load was applied with the upper disc while lower disc moved in a reciprocal motion. The load used in this experiment was 2N. The reciprocal motion was sinusoidal with

10mm amplitude and 1cm/s maximum speed. Three temperatures were used for this experiment: 35 °C, 65°C and 100°C.

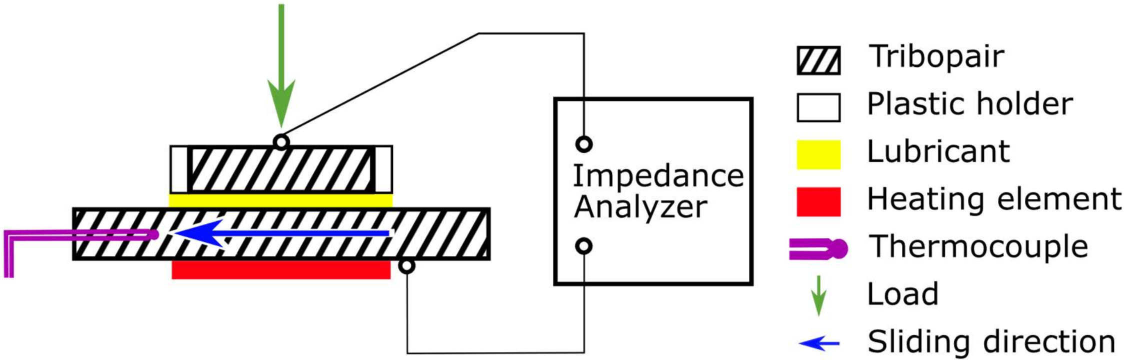

Figure V.7 The configuration of the impedance tribotesting system.

Chemical property of the tested surface was characterized with a Raman spectroscopy. Commercial Raman microscope (LabRAM HR Evolution, Horiba) was used in all the characterization process. The excitation light at 785nm and ~3.0mW generated from laser source(TEC-520-780-100, Sacher Lasertechnik) focused by an objective lens(LMPlanFL N, 50x, N.A. 0.5, Olympus) was used to generate the Raman signal. The spectrum was collected with a spectrometer with a 150 groves/mm grating. The resultant spectrum was averaged 30 times.

The anti-wear property of this nanolubricant was characterized with a ball-on-disc wear test. In this test, an E52100 ball and a polished E52100 plate was used with the same tribometer. The disc was moving at 1cm/s maximum speed in reciprocal motion with a 5mm amplitude. The load applied between the ball and disc was 2N. After 1000 cycles of testing, the sample was characterized with an interferometer (Zygo NewView 600, Zygo Corporation, Laurel Brook Road, Middlefield, CT).

5.2.3 The tribochemistry of amphiphiles nanolubricant

The Raman spectroscopy result revealed that the product of the amphiphiles nanolubricant tribochemical reaction is zirconium pyrophosphate (L-ZrP_2O_7). The Raman spectra of exfoliated α-ZrP and amphiphiles α-ZrP were shown in Figure V8a and FigureV.8b. Both spectra contain the peak at $1050cm^{-1}$ and $990cm^{-1}$, which corresponding to the POH stretching[309]. The amphiphiles nanoparticle shows two additional peaks at $1450cm^{-1}$ and $1310cm^{-1}$, which corresponding to bending of CH_3 bonds and stretching of CH_2 bonds, respectively[310]. Those two peaks are resulted from the epoxide modifications. However, those peaks were not found in the Raman spectra taken from the wear track (FigureV.8 c-e). These figures are taken from wear track generated under 35 °C, 65°C and 100°C respectively. All of them shows two peaks at the $1260cm^{-1}$ and $1110cm^{-1}$, with $1260cm^{-1}$ peak at a higher intensity. This indicated that a tribochemical reaction occurred during the experiments, and tribofilms were formed on the wear track. The most probable explanation of these two peaks are the complex peaks from Layered Zirconium pyrophosphates(L-ZrP_2O_7)[311–313]. The CH_3 bending peak at 1450 cm^{-1} still presenting in the spectra from tribofilms with varying intensities. There are two possible explanations. The first possibility is the carbon alkyl chain existed in the tribofilm as either an inclusion or surface modification.

Another explanation was the base oil (Light mineral oil) not completely removed during the cleaning process.

The tribochemical reaction mechanism can be explained by two processes. The structure of amphiphiles α-ZrP and L-ZrP_2O_7 were shown in figure V.8.f. The L-ZrP_2O_7 and α-ZrP has the same structure inside the layers but L-ZrP_2O_7 connect the layers with a phosphate atom instead of Van der Waals force between hydroxyl groups. To form the pyrophosphates, the nanoparticle must detach the alkyl chain on the surface. Such detachment is common in tribochemical reactions. The Zinc dithiophosphate (ZDDP) decomposition under tribochemical process started with the removal of its alkyl chain[314]. Similarly, the ionic liquids forms tribofilm started by the separation of head-group and alkyl chain[315]. After the detachment of the alkyl chain, the single layer α-ZrP structure went through a condensation process and formed L-ZrP_2O_7. Similar chemical reaction from multi-layer α-ZrP to L-ZrP_2O_7 at high temperature(700°C)[316,317]. This indicated that the tribological process greatly reduced the energy barrier between two compounds. The possible reaction is:

$$(C_{18}H_{38}NCO)_n@Zr(O_3POH)_2\cdot H_2O(s) \rightarrow H_2O(g) + ZrP_2O_7(s) + CO_2(g) + NO_x(g)$$

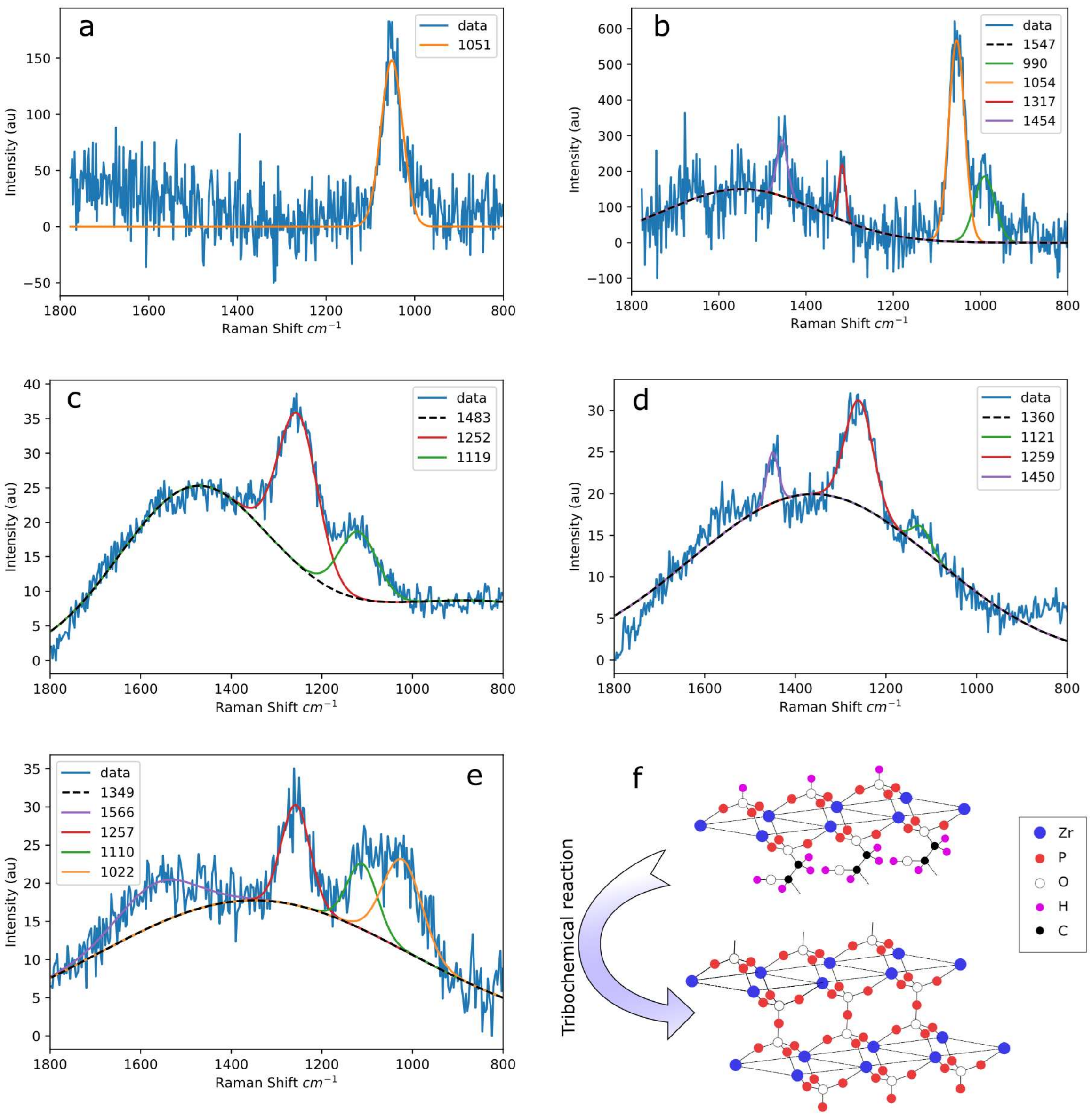

Figure V.8 The Raman spectra of exfoliated ZrP (a), A-ZrP (b), the wear track of 35 ° C(c), 65° C(d) and 100° C(e). The structure difference between the A-ZrP and L-ZrP2 O7 where the dotted lines represent -NH(CH2)17 CH3.

The nanoparticle additive reduced the coefficient of friction up to 40%. In figure V.9, the coefficient of friction between light mineral oil and nanolubricant under three testing temperature were plotted. Compared to the light mineral oil without any additives, the friction coefficient of nanolubricant is not only lower, but also more stable. The tribofilm generated by the A-ZrP has a layered structure, this structure may reduce the coefficient of friction by acting as a solid lubricant. The higher the temperature, the lower the coefficient of friction. This indicated the tribofilm was generated faster at a higher temperature, better protecting the surface.

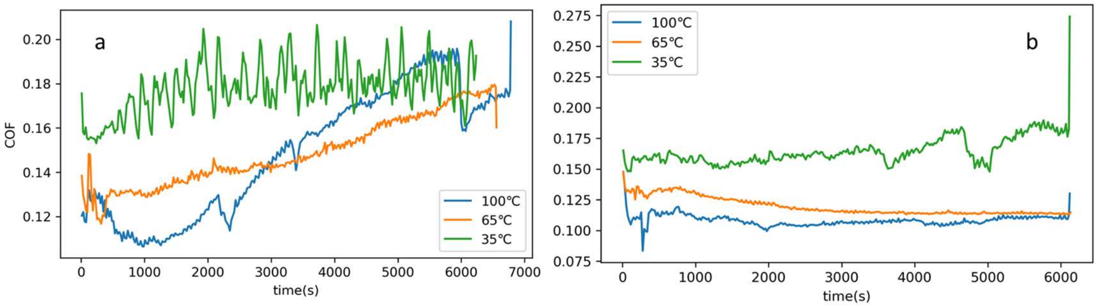

Figure V.9The coefficient of friction of light mineral oil(a) and nanolubricant(b).

The kinetics of this tribofilm growth was controlled by both the Arrhenius kinetics and wear process. The calculated resistance between two tribopair was plotted against the experiment time in Figure 5. All three experiment shows the resistance increase with the time. This indicated the deposition of the tribofilm increased the interface resistivity. This is expected because the L-ZrP_2O_7 is not conductive. However, this increase has a limit, the highest resistance in all the test were $10k\Omega$. It appears that the growth of tribofilm have two stages, first it was constant growth, then it stabilized at a certain resistance. The higher the temperature, the faster the initial growth speed. But the temperature has no perceivable influence on the final resistance. The growth section can be fitted to such simple functions: $R = At^2$, where A is the growth rate. That is, the resistance growth is proportional two the square of time. Under the assumption that the volume of the tribofilm is proportional to the resistance. The growth rate in this equation is the growth rate of tribofilm volume. The insect of Figure V.10 plots log (A) verses $1/(RT)$, where R is the gas constant and T is the temperature. This linear relation shows the growth rate follows an Arrhenius equation:

$$A \propto \exp\left(\frac{-E_A}{RT}\right)$$

where E_A is the activation energy. By fitting this linear relation, the E_A is 8822J/mol. The reason why there is a limitation of the resistance is the mechanical wear balanced the chemical growth. Thus, the final thickness of the tribofilm remains at a stable value.

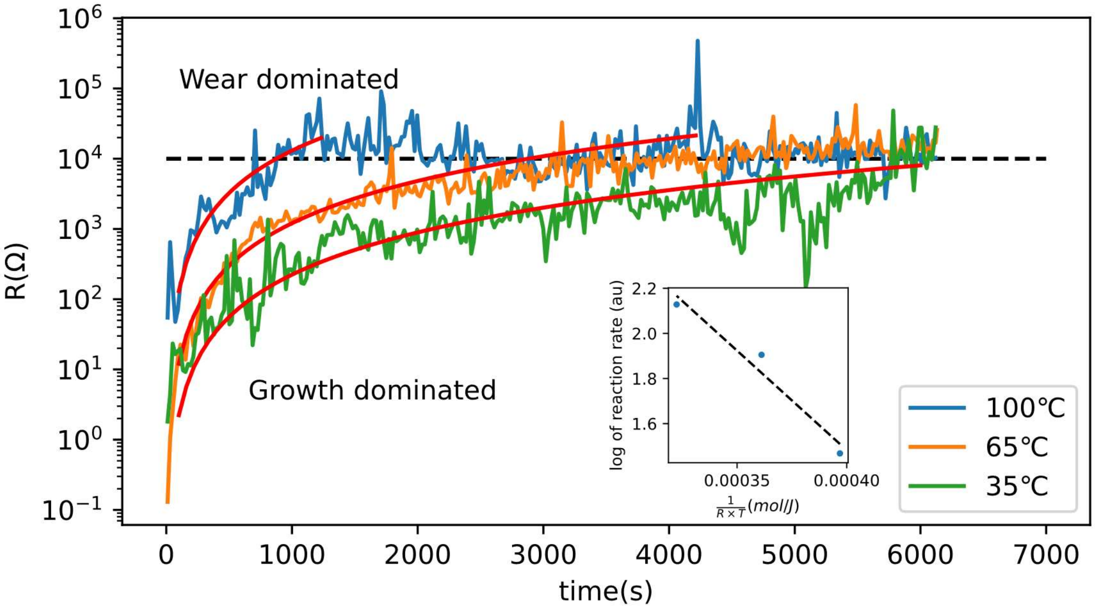

Figure V.10 The kinetics of tribofilm growth revealed by the *in situ* resistance tracking. The insect shows the relation between log of reaction rate vs. the 1/RT, indicating an Arrhenius behavior.

The coefficient of friction also influences the growth and wear of tribofilm. In figure 6, the growth rate was plotted against the coefficient of friction. This plot also shows the growth-dominated behavior and the wear-dominated behavior. The experiment carried out under 35℃ never entered the wear-dominated behavior. Thus, its growth rate always increased with the coefficient of friction. For the experiment under 100℃, most of its data are from the wear-dominated zone. Thus, an increase of the coefficient of friction always promotes wear and decreases the growth rate. The experiment under 65℃ has mixed behaviors. It follows the 35℃ at a high coefficient of friction but follows the 100℃ behavior at lower friction.

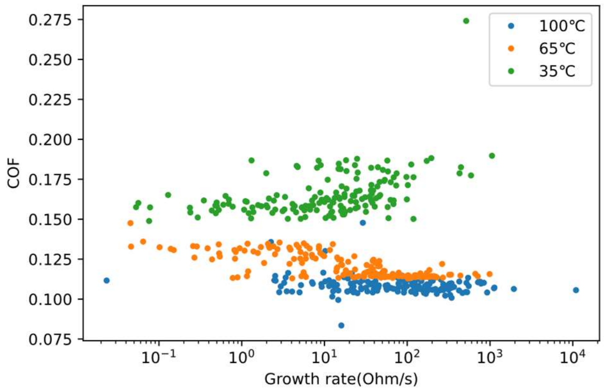

Figure V.11 The coefficient of friction's influence on growth rate.

This balancing behavior creates an electrically homogenous contact. Figure 7 compared the resistance mapping on the base oil and the nanolubricant. The resistance of the contact at different time period and different positions of wear track was plotted as different colors. The resistant mapping of the base oil shows a lot of patches. This is because the tribofilm formed in the base oil is not electrically uniform. The resistance of the contact lubricated by the nanolubricant is uniform after about 800s when the tribofilm is formed. This indicated the nanolubricant produced a stable electric contact.

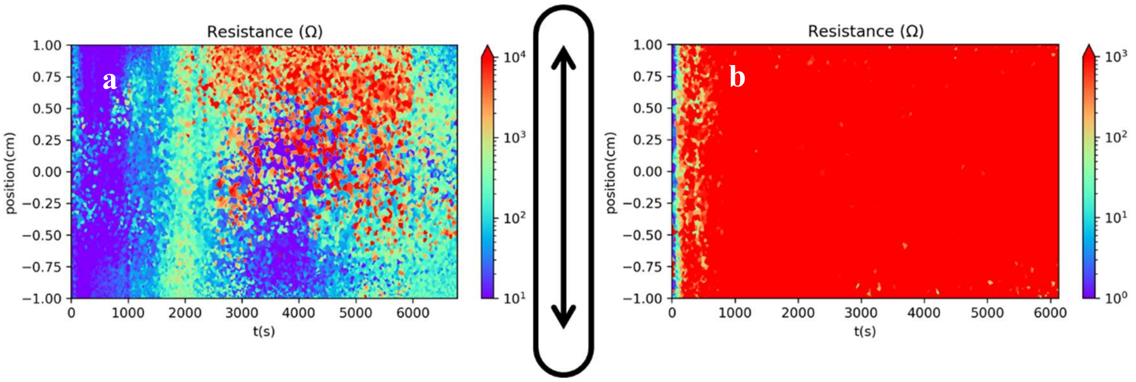

Figure V.12 a) the resistance mapping of base oil under 100℃, b) the resistance mapping of nanolubricant under 100℃

Because of the generated tribofilm, the nanolubricant has a better anti-wear property compared to the light mineral oil. Figure 6 shows the height map of the wear track generated from the interferometer. When the ball-on-disc system was lubricated with light mineral oil, the surface shows typical lubricated wear (Figure 6 a). With the help of nanolubricant, the wear reduced nearly non-existence (Figure 6 b). The L-ZrP_2O_7 generated from the nanolubricant protected the surface. The wear rate for the light mineral lubricated surface was 3828 $\mu m^2/m$ and the nanolubricant lubricated surface has a wear rate of 308 $\mu m^2/m$. This means nanolubricant can reduce the wear by 90% compared to light mineral oil.

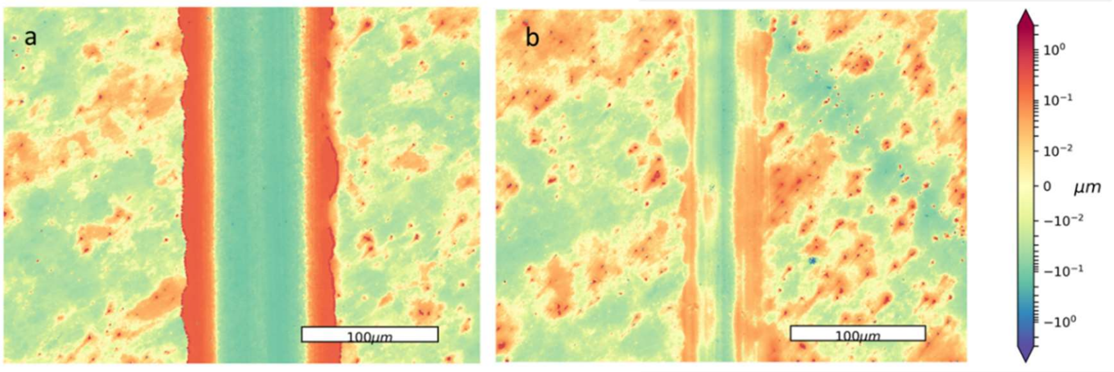

Figure V.13 The height map of the wear track from ball-on-disc test. Compared to the light mineral oil(a), the nanolubricant(b) greatly reduced the wear.

5.3 Summary

Novel amphiphilic nanolubricant was formulated based on light mineral oil and modified 2-D α-ZrP. This nanolubricant contains the nanoparticle analog to the amphiphilic friction modifiers and ZDDP. Its amphiphilic structure was expected to have a better reactivity on the surface of tribological contacts.

The tribotesting shows that compared to the light mineral oil, the nanolubricant reduced the friction up to 40% and wear up to 90%. The Raman spectroscopy revealed the mechanism of wear and friction reduction in tribochemical reactions. The modified nanoparticle turns into layered pyrophosphate under tribological conditions. This layered tribofilm reduced friction and wear. The in-situ resistance tracking shows that the kinetics of this reaction follows the Arrhenius relation. The final film thickness is controlled by the balance between wear and chemical processes. The tribochemical process was dominated by chemical growth or mechanical wear. Because of this balance, the tribofilm has a limited thickness. The temperature has a great influence on the growth speed. The growth rate has an Arrhenius-like behavior to the temperature. The coefficient of friction influenced both the wear and growth behavior. When the coefficient of friction is increased, both the growth and wear increase. This balanced growth of tribofilm produced a stable electrical contact.

CHAPTER VI

APPLICATIONS[4]

In this chapter, a study was conducted in association with two applications. The first was to use a nanolubricant to prevent severe wear during galling. In the second an aqueous nanolubricant was used to prevent and repair the wear of a tooth. Both implanted 2D nanoparticles, treating a tribological wear under low speed and high pressure. The effectiveness of using 2D nanoparticles in wear protection was demonstrated.

6.1 Tribochemical reactions for galling prevention

6.1.1 The galling of metals

In industrial applications such as oil and gas exploration, metal forming, and machine elements like air bearings, one of the most common failures is galling. [127–130]. Metals are known to be galled under severe contact conditions. In particular alloys containing face-centered cubic crystal structure, such as those in austenite stainless steel or aluminum alloys, are susceptible to galling failure [131]. Galling is known as an extreme form of adhesive wear, often characterized by the protrusions formed above the original surface[132]. Slow sliding speed, high contact pressure, and inadequate lubrication are often associated with galling. Galling can be in the forms of cold welding, instant seizure, and breakage of components, [133] that are catastrophic.

---

[4] Part of this chapter is reprinted with permission from "Using nanoparticles to prevent enamel wear." By Chen, Yan, Bradley T. Simon, Lynne A. Opperman, Peter Renner, Dilworth Parkinson, Alexander Sinyukov, and Hong Liang. Biotribology 26 (2021)
Part of this chapter is reprinted with permission from "Anti-galling effects of α-zirconium phosphate nanoparticles as grease additives." By Chen, Yan, Xuezhen Wang, Abraham Clearfield, and Hong Liang. Journal of Tribology 141, no. 3 (2019).

6.1.2 Synthesis and evaluation of anti-galling nanolubricant

All ZrP nanoparticles in this research were prepared using a hydrothermal method[318]. A mixture of 4 grams $ZrOCl_2 \cdot 8H_2O$ (Sigma-Aldrich, St. Louis, MO) and 40ml of H_3PO_4 (Sigma-Aldrich, St. Louis, MO) was sealed inside a Teflon-lined hydrothermal vessel and heated up to 200°C for a certain time. The nanoparticles were then washed with deionized water and dried. Three different sizes of ZrP nanoparticles were fabricated using the procedure in Table 1[318].

Table VI-1. ZrP synthesis procedure

Expected particle size	H_3PO_4 concentration	Time
200nm	3 mol/L	5h
500nm	3 mol/L	24h
1000nm	12 mol/L	24h

After synthesis, the morphological characteristics of the nanoparticles were examined. Synthesized nanoparticles were dispersed in 200 proof ethanol (Sigma-Aldrich, St. Louis, MO) forming a mixture which concentration was about 0.05mg/ml. The mixture was cast on a glass slide(VWR, Radno, PA) and dried in air. The nanoparticles dispersed on the glass slide was then characterized using AFM (Nano-R2, Pacific Nanotechnology, Santa Clara, CA) mode.

Grease samples used in this experiment were prepared by mixing nanoparticles with two kinds of greases: API grease(Jet Lubes, formulation described in API 7A1[130]), and petroleum jelly. All mixtures containing 0.5 weight percent of nanoparticles. Those mixtures were stirred for 10 minutes and treated with ultrasonic for 4 hours to make the nanoparticles dispersed relatively evenly in the grease.

To investigate the anti-galling effect of nanoparticles as additives, experiments were conducted using a specialized tester. A pair of carbon steels were examined, 4130 and P530, as schematically shown in Figure 1. These steels are nonmagnetic stainless steel used in drill pipe applications[319,320]. The 4130 and P530 pair were used as drill pipe collars which were subject to galling in the drilling operation. The property of 4130 and P530 steel are listed in Table 2. In figure 1, a grease is applied between two sliding surfaces. The maximum applied load and torque are 0.45 $kN \cdot m$ and 160kN. During operation, specimens were brought into contact. The bottom one was held stationary, and upper rotated at 3 rpm. Subsequently, the normal load between the specimens was ramped up until the torsion on the sample reached $236\ N \cdot m$. The same pair of samples were used in all experiments. Before and after each test, the surface morphology was observed under the interferometer (Zygo NewView 600, Zygo Corporation, Laurel Brook Road, Middlefield, CT).

Table VI-2 Chemical compositions of P530 and 4130 steel[319,321]

	C	Cr	Mo	Si	N
P530	max 0.05	13.00	0.40-0.60	-	0.25-0.40
4130	0.28-0.33	0.80-1.10	0.15-0.25	0.15-0.35	-

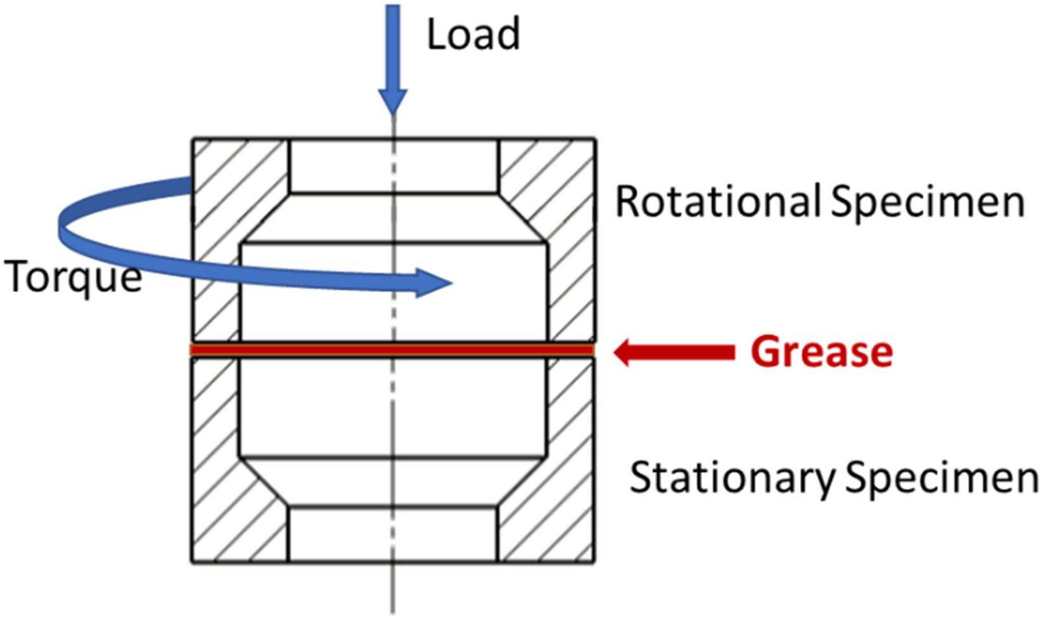

Figure VI.1.The cross-section of galling testing specimens when loaded on the instrument. The inner and outer diameter of mating surfaces was 48mm and 38mm. The direction of applied load and torque is also shown.

To obtain the contact nature of particle additives and surfaces, two pairs of samples of different surface roughness were prepared. They have the average surface roughness of 5nm and 16nm. The rough surface was achieved by grinding the sample surface with 800 grit sand papers. The sample with a smooth surface was polished with alkaline colloidal silica polishing fluid for a half hour after grinding. As shown in Figure 2, the smooth surface has a smooth surface profile while the rough surface consists of visible ridges and valleys. After each experiment and characterization, the sample surfaces were ground with sandpaper and polished to the same roughness of 5nm or 16nm.

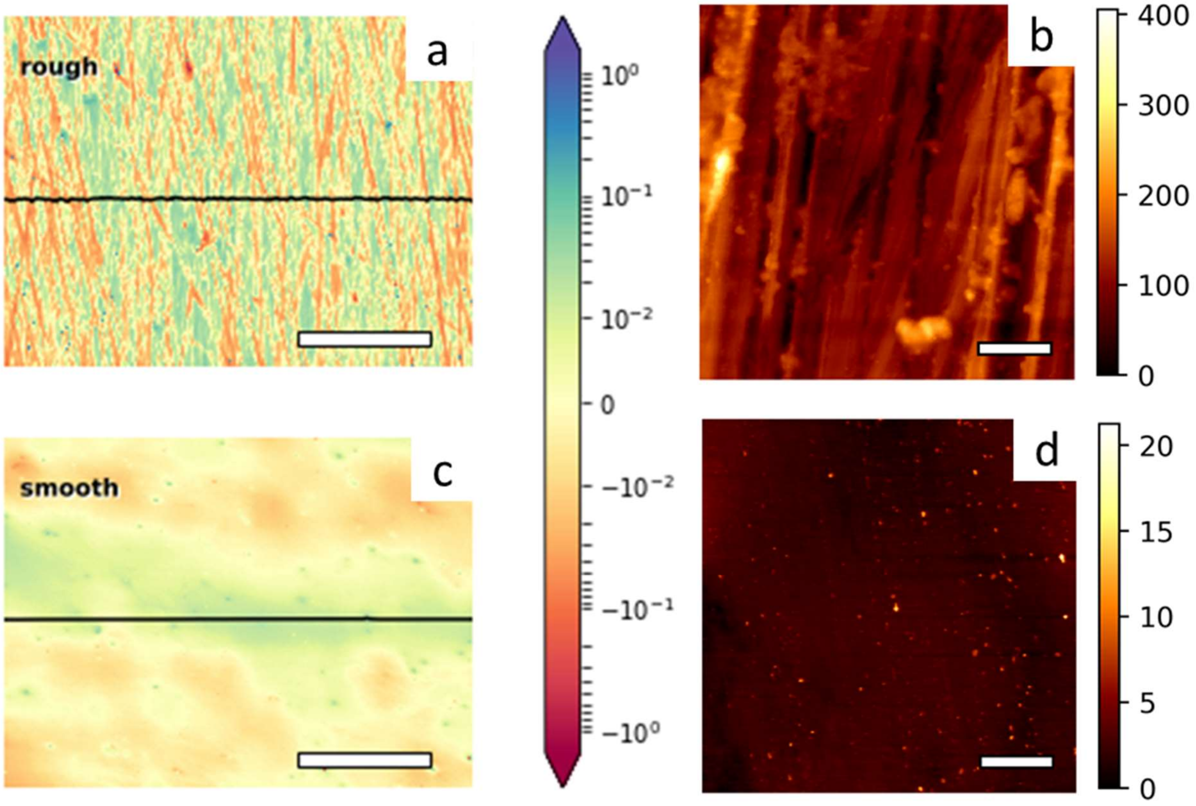

Figure VI.2, (a,b) The interferometer measurement of rough(a) and smooth(b) surface, scale bar length is 100μm, color bar unit μm. (b,d) AFM height map of rough(b) and smooth(d) surface, scale bar length is 2μm, color bar unit nm.

6.1.2 The anti-galling properties of nanolubricants

The morphological characteristics were examined on as-synthesized α-ZrP nanoparticles. Figures 3 a-c were the AFM images of particles. They were obtained by combining height image and phase images through AFM scanning. The grey scale of the image shows the topography, and the color represents phase contrast. The thickness (as shown in the height map) of those nanoparticles was 8nm, 25nm and 300nm for 200nm, 500nm and $1\mu m$ sized nanoparticles respectively. The thickness of nanoparticles is associated with the number of stacked layers. The distance between the two layers of α-ZrP is 7.6Å [322]. Estimation of the number of layers based on the thickness of α-ZrP are 10, 30 and 400 for the 200nm, 500nm and $1\mu m$ sized nanoparticles respectively. The effect of the number of stacked layers will be discussed in later section.

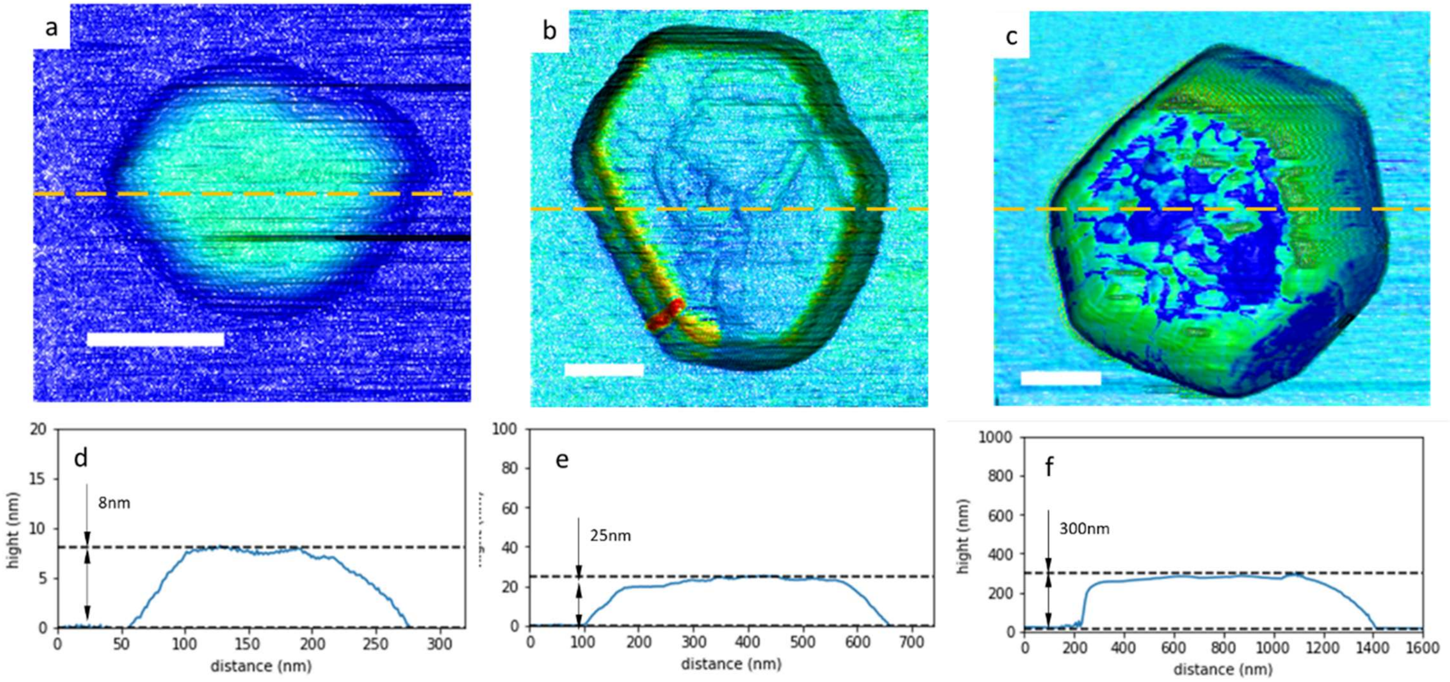

Figure VI.3 The morphology of nanoparticles generated by AFM data of α-ZrP nanoparticle of 200nm(a), 500nm(b) and 1μm(c) size on glass substrate. The false color in those image shows the value of the phase contrast. (d-f) the profile of the nanoparticle of 200nm,500nm and 1μm.

Grease with nanoparticle additives shows reduced friction during galling experiments. The load and the torque measurement using petroleum jelly as a reference (Figure 3(a)) exhibited lower torque. The apparent friction coefficient, i.e., the total force through torque divided by the applied load, can be calculated. Results are shown in Figure 3(b). It is seen that the addition of nanoparticles reduced the apparent friction coefficient. Details will be discussed with the faction factor below. The reduction of apparent friction coefficient in galling test can suggest the reduction of galling[323]. The degree of anti-galling effect of nanoparticles will be discussed in the following.

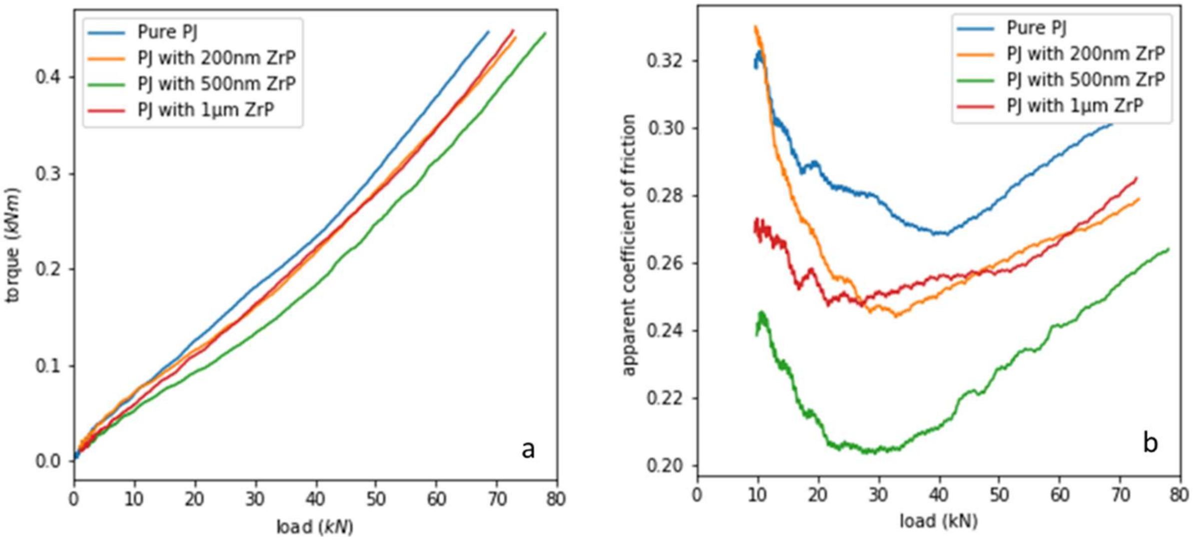

Figure VI.4, (a) the load and torque reading from galling testing using petroleum jelly with or without nanoparticle additives. (b) The apparent coefficient of friction in the galling test calculated from the torque and load data.

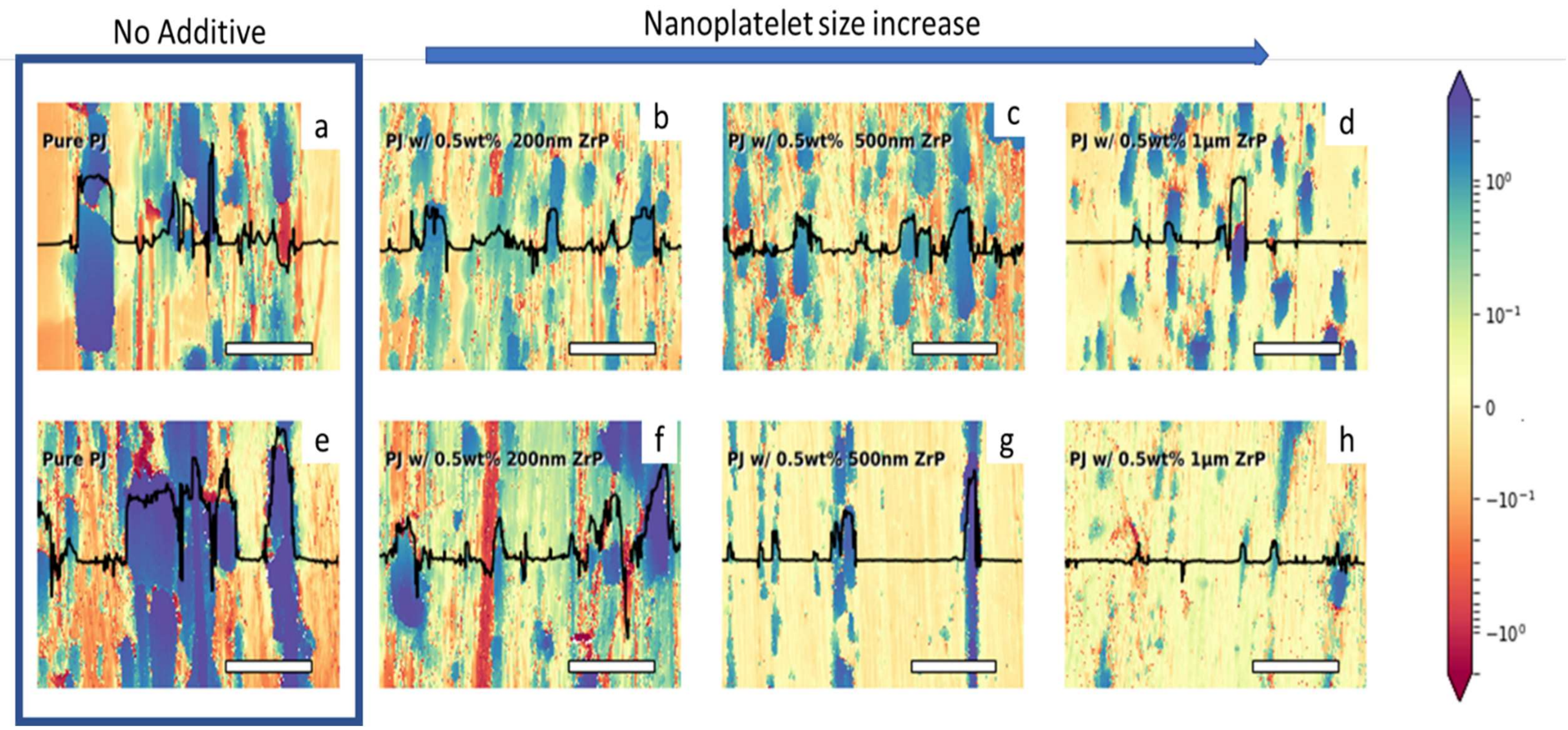

Figure VI.5, The surface morphology of smooth(a-d) and rough(e-h) sample (rotatory part) after the galling test with or without nanoparticle additives. The black line indicates the surface profile of the center line. The galling was reduced with increased nanoparticle size in petroleum jelly. Scale bar length is 100μm. Unit of color bar is μm.

How does the addition of nanoparticles affects galling behavior ? Before and after galling experiments, the surface morphology was observed under interferometer (Figures 2 a,c and 5). Two samples were studied for galling experiments, the smooth (5.0nm Ra, Figures 5 a-d) and rough (16nm Ra, Figures 5 e-h). The black lines are the profile of the surface center line and the colored ones are the surface height. The blue color means the higher altitude of the surface and the red is that of the valley. For the specimen having a smooth surface (Figures 5 a-d), the reference sample (galled in petroleum jelly) shows considerable amount galling (50% Figure 5a). The blue color is the galled area and is evidenced by the surface profile in dark lines. When nanoparticles are added, the larger the particles, the less the galling (Figures 4 b-d). It's confirmed by both the color (galling) and profile. The sample with rough surface tested in petroleum jelly showed the material was galled 60% (Figure 5e). Like the sample with a smooth surface, when nanoparticles added in the petroleum jelly, the larger the particles, the less the galling (Figures 5e-h). When 0.5wt% $1\mu m$ nanoparticle is added, the sample with the rough surface has less than 10% surface galled, an 80% decrease in comparison to petroleum jelly without additives.

To further validate the effectiveness, we added the particles in a commercial grease (API Ca-F thread compound). Without additives, the sample surfaces showed galling (Figures 6 a, c). With additives of 0.5% $1\mu m$ nanoparticle, the galling was visibly reduced in sample either with smooth (Figure 6b) or rough (Figure 6d) surface. It is clear that nanoparticles improve the anti-galling performance.

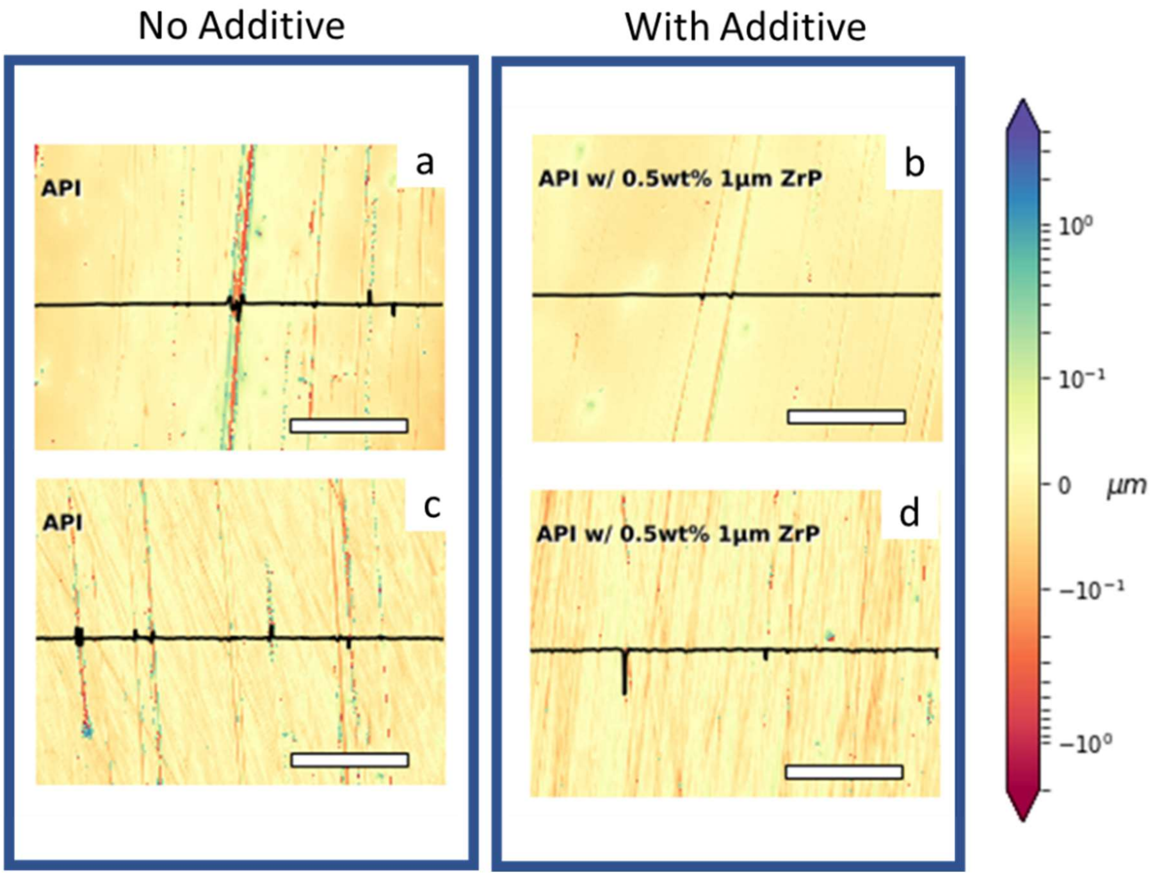

Figure VI.6, The surface morphology of smooth(a,b) and rough(c,d) sample (rotatory part) after the galling test with or without nanoparticle additives. The black line indicates the surface profile of the center line. Scale bar length is 100μm. The unit of color bar is μm.

There are two possibilities for galling reduction. One is the area% of coverage by nanoparticles and the other the number of stacked ZrP layers in nanoparticles. Considering the density of the grease (1.5 g/cm^3) and that of the α-ZrP (2.7 g/cm^3) [322], the density of nanoparticles and their coverage on the mating surfaces (assuming a

$1\mu m$ gap in between surfaces) can be estimated . Table 3 listed the density of particles, their surface coverage, and the stacked layers of those. According to the results obtained through the galling experiment, the nanoparticles have low area coverage and a high number of stacked layers ($1\mu m$ nanoparticles) appear to have the best performance. It appears that the number of stacked layers were the dominating factor of anti-galling behavior.

Table VI-3 The calculated surface coverage of nanoparticles

Dimeter of α-ZrP Nanoparticles	Number density ($\#/mm^{-1}$)	Coverage on surface	Number of stacked layers
200nm	1×10^{10}	33%	10
500nm	5.5×10^{8}	10%	30
1μm	1.7×10^{7}	1.5%	400

One possible reason for stacked particles to reduce galling is that α-ZrP nanoparticle can be exfoliated under stress. The α-ZrP has layers connected by a Van Der Waals force with a distance of 7.6 Å[322]. We can estimate the Van Der Waals force between those two layers as[209]:

$$P = \frac{A}{6\pi h^3}$$

here P is force per unit area, h is the layer distance and A is the Hamaker constant. For inorganic materials like ZrP, the Hamaker constant was in the range of $10^{-19}J$ [210].

Thus, the separation of α-ZrP requires stress in the order of $12MPa$, one order of magnitude smaller compares to the yield stress of stainless steel. Additionally, the ZrP particles was negatively charged[324]. This means the actual interaction force between layers will be even smaller due to electric static force. When ZrP nanoparticles inserted in between the rubbing surfaces (Figures 7 a-c), its layers were exfoliated under stress (Figure 7 d). Under shear, the exfoliated ZrP can react and form zirconium pyrophosphate and protect the surface:

$$Zr(O_3POH)_2 \cdot H_2O(s) \rightarrow 2H_2O(g) + ZrP_2O_7(s)$$

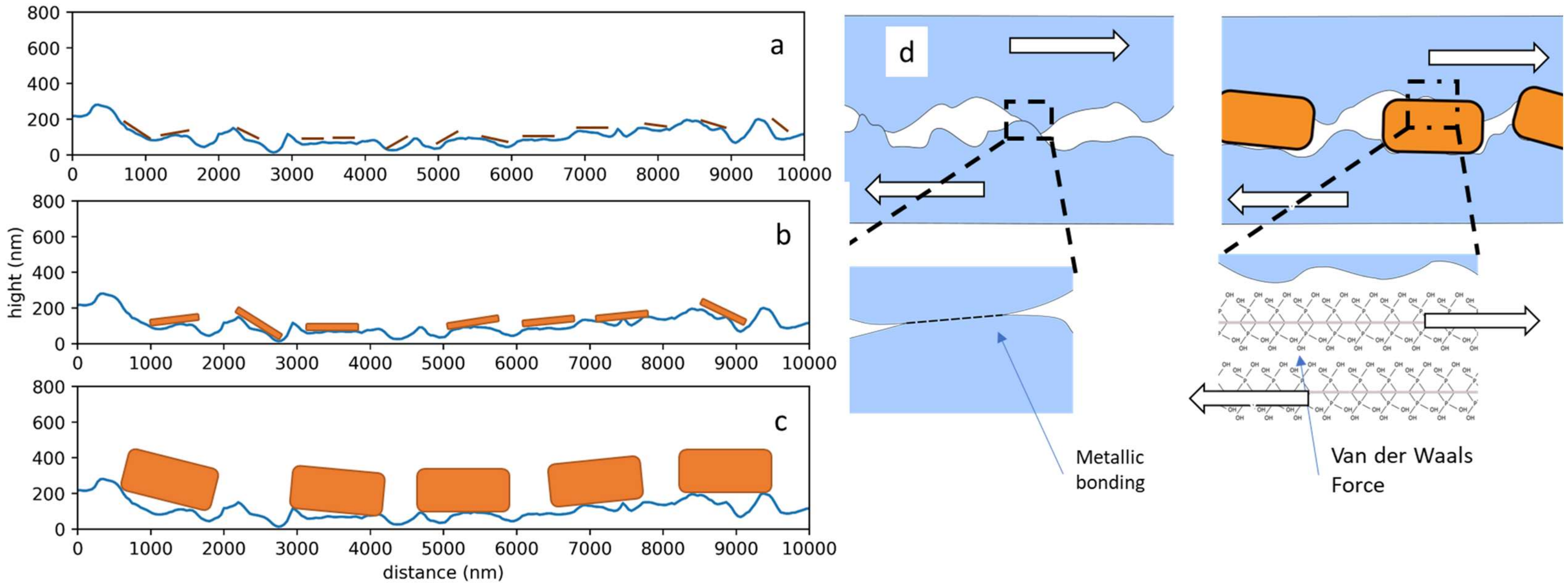

Figure VI.7, (a-c) Profile of surface from rough surface AFM height map with 200nm(a), 500nm(b) and 1000nm(c) nanoparticle (draw to scale) on it. (d) The mechanism of galling reduction: the existence of nanoparticle separated mating surfaces. Their weak Van der Waals force is easy to break compare to metallic bonding, causing them to exfoliate under stress.

The $1\mu m$ particle also is less likely to act like an abrasive particle. According to galling experiment, the surfaces of samples using 200nm and 500nm nanoparticles appears to have abrasive wear (Figures 5 b-d, f, red). Comparing with the 1um particles, 200nm and 500nm nanoparticles are less likely to be exfoliated because of a small number of stacked layers. The unexfoliated nanoparticles thus act as abrasive particles when trapped in the valley. Due to shear, they turn around similar to three body wear condition.

The friction factor obtained through galling suggests that $1\mu m$ nanoparticle has the favorable performance. This parameter is used to compare the frictional behavior of petroleum jelly to a standard grease. The friction factor of petroleum jelly with 200nm, 500nm and $1\mu m$ nanoparticles the friction factor was 1.55 ($\pm$ 0.07), 1.50 ($\pm$ 0.1) and 1.39 ($\pm$ 0.05). Petroleum jelly added with $1\mu m$ nanoparticles has the lowest friction factor, that is a 10% reduction.

6.1.3 Summary

In this research, α-ZrP nanoparticles were studied for their effects on galling. Three nanoparticles with diameter of 200nm, 500nm, and $1\mu m$ were fabricated using hydrothermal method. Their thickness was 8nm, 25nm, and 300nm respectively. Experimental evaluation was carried out using a galling tester. Results showed that adding nanoparticles can reduce torque and friction as well as galling. It was interesting to find out that the number of stacked layers dominated the galling reduction. The sample tested in petroleum jelly added with $1\mu m$ nanoparticles can effectively reduce galling by 80% compared to the one without additives. In terms of galling friction, those particles are effective in reducing friction factor for 10%. Analysis in morphological characteristics revealed that the Van der Waals forces introduced into grease promoted the exfoliation of nanoparticles resulting surface protection. This research opens new approaches to design future lubricants.

6.2 The formation of a tribofilm to prevent tooth enamel damage

6.2.1 The protection of tooth enamel

The previous chapters reported that functionalized nanoparticles, when used as additives in a lubricant, could generate a protective film on a pair of rubbing surfaces. Subjecting these particles to frictional forces generate a film on the surface called tribofilm[290,291,300,325,326]. This film is harder than the original substrate surface and likely can protect the surface from future damage. Our recent research found that α-zirconium phosphate (α-ZrP) and sodium yttrium fluoride (NaYF4) were effective additives to form the tribofilm[299–301,327]. The α-ZrP nanoparticles have a unique layered structure which is held together via Van der Waals forces [322,328]. Under shear, chemical reactions between particle and surface are triggered, forming a protective layer on the surface[300,301]. To date, repairing or preventing surface wear of teeth using the concept of tribofilms has not been reported [291,300]. This new method was inspired by the effectiveness and rapidity of tribochemical interactions between rubbing surfaces. This interaction can form a protective film more rapidly compared to current alternate remineralization methods.

The objective of this research is to investigate a novel approach to restore, modify, and protect tooth enamel using functionalized nanoparticles. The hypothesis to be tested is that intercalated α-ZrP nanoparticles form a hard protective layer on enamel when added via simulated chewing.

6.2.2 Repair Material Synthesis

The α-ZrP nanoparticles and HAP nanoparticles were synthesized using hydrothermal methods. For α-ZrP, 50mL food grade 12M phosphoric acid (Sigma Aldrich, St. Louis, USA) and 5g zirconyl chloride octahydrate ($ZrOCl_2 \cdot 8H_2O$, Sigma Aldrich, St. Louis, USA) was mixed under constant stirring conditions. The mixture was then sealed in a polytetrafluoroethylene (PTFE) lined autoclave and moved to a 200℃ oven for 24 hours. The precursor of HAP was prepared with the following procedure: 12mL 0.25M calcium nitrate (Sigma Aldrich, St. Louis, USA) solution ($Ca(NO_3)_2$) was added dropwise into 20mL 0.15M disodium hydrogen phosphate (Na_2HPO_4, Sigma Aldrich, St. Louis, USA) solution under constant stirring at 50-60℃. The pH of this mixture was adjusted to 8-10 with ammonium hydroxide (Sigma Aldrich, St. Louis, USA). This mixture was put in a PTFE lined autoclave and placed in a 160℃ oven for 12 hours. After the hydrothermal reactions, the products were washed with deionized (DI) water and retrieved by centrifugation three times. The washed nanoparticles were dried in a vacuum furnace at 70℃ for 12 hours. The synthesized α-ZrP was intercalated with polyether amine M-600 (Huntsman Corporation, Houston, TX, USA). The synthesized 1mmol α-ZrP was first dispersed in 5mL of DI water with an ultrasonic bath for 1 hour, then 5mL 0.4M M-600 solution was added into the dispersion dropwise.

The repair agents, as pastes, were developed as a mixture of the HAP nanoparticles and M-600 amine intercalated α-ZrP. The synthesized dispersion of intercalated α-ZrP was first mixed with the HAP nanoparticles. The amount of HAP nanoparticles used in mass ratios to α-ZrP before intercalation was 0:1, 0.25:1, 0.5:1 and 1:1 (the produced repair agents were labeled as S0, S2.5, S5 and S10). The products were centrifuged for 10min. After the centrifuge process, the supernatants were removed by tilting the tubes, and the precipitates were retrieved. These precipitates were used in the tribo-mastication process described in the following sections.

6.2.3 Simulation of chewing

Dog canine teeth were used to create both “disc” teeth and “pin” teeth for the experiment. All dog canine teeth were procured from postmortem extractions from dogs used in unrelated studies. Before the experiment, all the teeth were washed in hydrogen peroxide (H_2O_2) and DI water. Any residual soft tissue was removed with a small knife. To make the disc teeth, each canine tooth was first sealed in epoxy resin with the chewing contact surface exposed. Then, the enamel of this surface was carefully shaved flat, ground smooth with sandpaper and polished with a $3\mu m$ grit diamond paste. This polishing process created a flat surface on each tooth to simulate mechanically worn or damaged enamel and created a reference surface for film thickness measurement. This process was repeated to create 5 flat surfaces on each “disc” tooth Five teeth, each with five flat disc areas were created. The “pin” teeth were untreated dog canine teeth.

To simulate the chewing and grinding motion of teeth, a rubbing process was used. This process was conducted on a pin-on-disc tribometer (CSM Instruments, Needham, Massachusetts). The set-up of this rubbing mastication experiment is illustrated in Figure 8. In every rubbing mastication experiment, two freshly prepared dog canine teeth were used, one configured as a pin, and the other as the disc. The normal force on the pin was 1 Newton (N). This force generates an approximate pressure of 100MPa on the contact area, which is similar to the pressure a tooth experiences when chewing on hard food such as bones[329]. The “pin” tooth was moved with a sinusoidal reciprocal motion on the disc tooth with an amplitude of 2mm and a maximum speed of 1cm/s. Approximately 0.005mL of repair agent paste was placed between the teeth before the rubbing-mastication process started. The motion was terminated after 100 cycles. After the process, samples were washed with DI water and air-dried. The repair agents (S0, S2.5, S5, and S10) were tested with this rubbing-mastication process before interferometry and atomic force microscopy (AFM) observation. Each set of tests with each material were carried out on a new pair of teeth and repeated five times at adjacent new locations. In total, five pairs were used, which included four repair agents. The disc tooth was used for surface characterization in order to quantify the repair outcome.

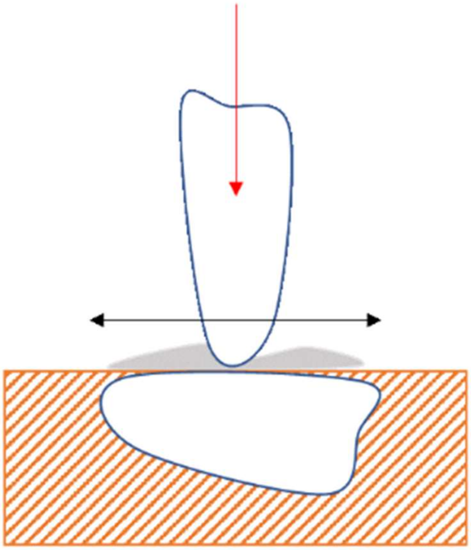

Figure VI.8The rubbing-mastication process. Two canine teeth were used in this set up, one as the "disc" (bottom) and one as the "pin "(top). The "disc" tooth was sealed in epoxy (dashed block) with surface enamel polished. The "pin" tooth was pressed down and rubbed.

6.2.4 Characterization of repaired tooth surface

After rubbing experiments, surfaces were examined using interferometry, atomic force microscope, and Raman spectroscopic techniques. After the rubbing-mastication process, the effect of each repair agent on all "disc" samples were characterized. The formed film morphology and microstructure were characterized by an interferometer (Zygo NewView 600, Zygo Corp, Berwyn, PA) and atomic force microscopy (AFM, Nano-R2, Pacific Nanotechnology, Santa Clara, CA) using close-contact mode. The interferometer mapped the topographic information of samples optically. A heightmap was generated for each sample based on the monochromatic light interference. The AFM also generated a heightmap for each sample with a tiny prob. That prob interacts with the surface-force of samples. The heightmap and a phase map were generated by tracing that interaction. The Raman spectrum result of the repair film was collected with an iHR550 Spectrometer (HORIBA Scientific, Edison, NJ) with a 532nm laser. The photon of the laser can inelastically scatter by chemical groups inside the surface layer of a sample. The wavelength of the scattered photons was detected with a digital controlled spectroscope. Two spectrums were collected, one from the repair film, the other from the polished tooth surface. Data collected from those instruments were plotted with python. All method described above are non-destructive and requires no further treatment of the samples.

To test if the newly created protective film was resistant to removal and to evaluate the mechanical strength of the protective film, a simple scratch test was preformed on the tooth sample (S5) that had visible film formed. The repair agent S5 was chosen because it generated the best thick protective film. The same tribometer with a steel needle was used to perform this scratch test. The needle was pressed against the tooth disc sample with 1N force and scratched across the formed repair film and across exposed enamel manually.

To examine the durability of repair film coverage on teeth, the “pin” teeth were analyzed with Synchrotron micro X-ray CT (μ-XCT). For this experiment, a new rubbing-mastication experiment was conducted. In this test, the tooth repair agent S5 was used with new “pin” and “disc” tooth samples. The S5 agent was chosen for the same reason as for the scratch test. The μ-XCT experiments were performed on the the Beam line 8.3.2 instrument at Lawrence Berkeley National Laboratory. All samples were imaged with a LuAG:Ce scintillator. Tomographic reconstruction was conducted using Xi-CAM with a tomopy tomography plugin.

The imaging of the coatings from all experimental films and controls was accomplished using the dual energy k-edge technique [330–332]. Before the test, the illuminating x-ray energy was calibrated to the x-ray absorption edge of the Zr with a pure α-ZrP nanoparticle sample. As illustrated in Figure 9, the x-ray absorption by Zr element jumps around 18KeV. Two illuminating energies were used to take two separate tomographic images of the same sample: 18.2KeV and 17.8KeV. From figure 9, when the sample was illuminated with 17.8KeV, the Zr element will be brighter than when illuminated with 18.2KeV. Thus, a simple subtraction between the two data sets can reveal the distribution of the Zr element, which demonstrates the distribution of the repair film. The data collected from these experiments were then rendered with Avizo software (Thermo Fisher Scientific, Waltham, MA).

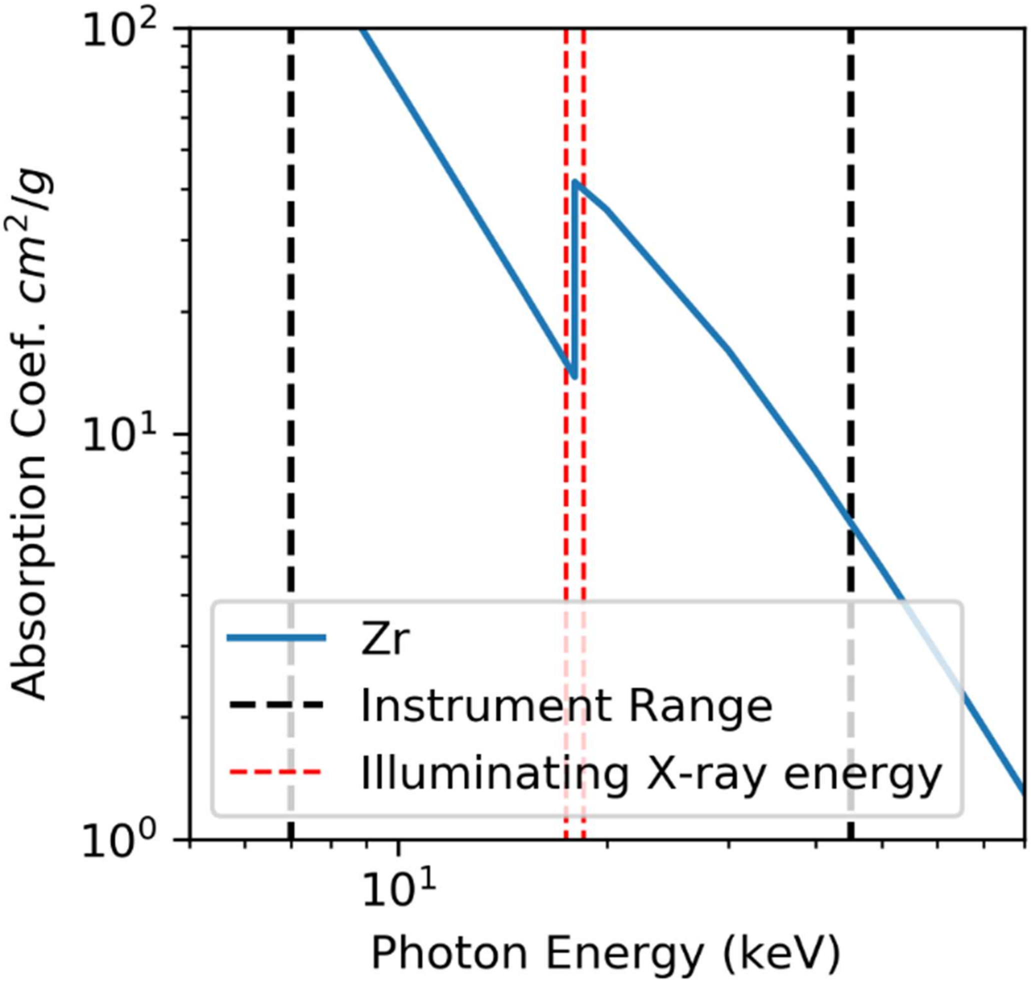

Figure VI.9 The x-ray mass attenuation coefficient for Zr. The data used in this plot was collected from the National Institute of Standards and Technology database (NIST).

Repair films were formed by the rubbing-mastication process for all repair agents. The interferometer topographic image is shown in Figure 10. Simulated chewing with the different repair agents generated protective films with different coverage and thickness ranging from 100nm to 1 micron (orange to red range in Figure 10). Where no repair material was present the baseline height of the enamel is yellow and where 100nm to 1 micron of enamel was removed by polishing the color is green. The repair agent S0 resulted a continuous but thin film, while the repair agent S1 resulted in a lumpy but thick film. The repair agents S2.5 and S5 produced a film with better film coverage and film thickness compare to both S0 and S10. Compare to protective film formed with S2.5, the protective film formed by S5 was more continuous. Therefore, we concluded that the repair agent that produced the best result in terms of coverage and thickness was S5.

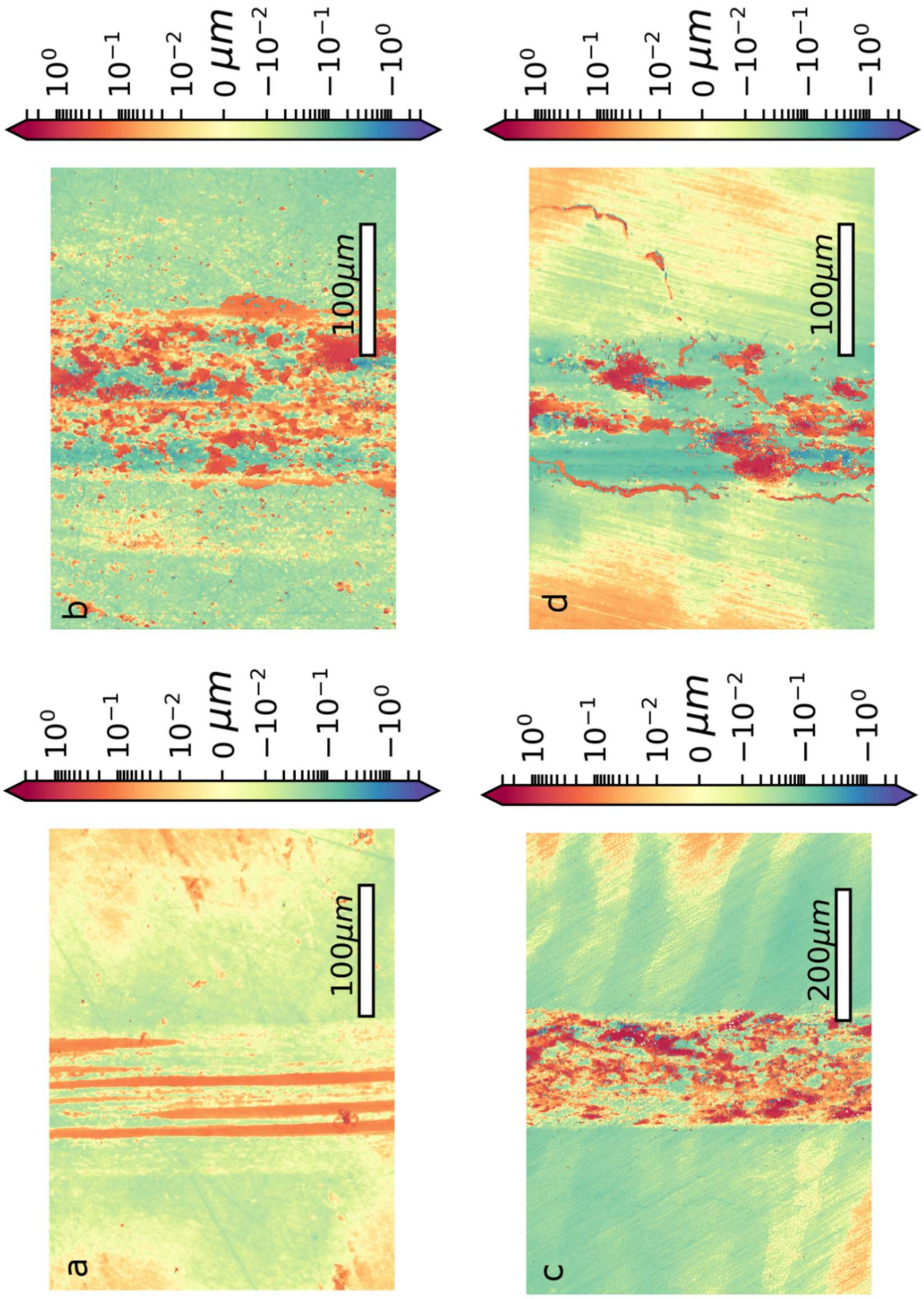

Figure VI.10 The interferometer image of the enamel surface after the rubbing-mastication process with repair agent, S0(a), S2.5(b), S5(c) and S10 (d).

The AFM analysis revealed the micro-structure of the intercalated α-ZrP repair films. Here the result from repair agent S0 which was pure intercalated α-ZrP and the repair agent S5 which have the best performance were shown (Figure 11). In Figure 11, the AFM height and phase map of the repair films in Figure 10a and Figure 10c are shown. The repair film generated with S0 contained many flaky particles on the surface with a size around 100nm (Figure 20a, b). The repair film generated with S5 showed a surface consisting of granular particles with a size around 50nm (Figure 10b, c).

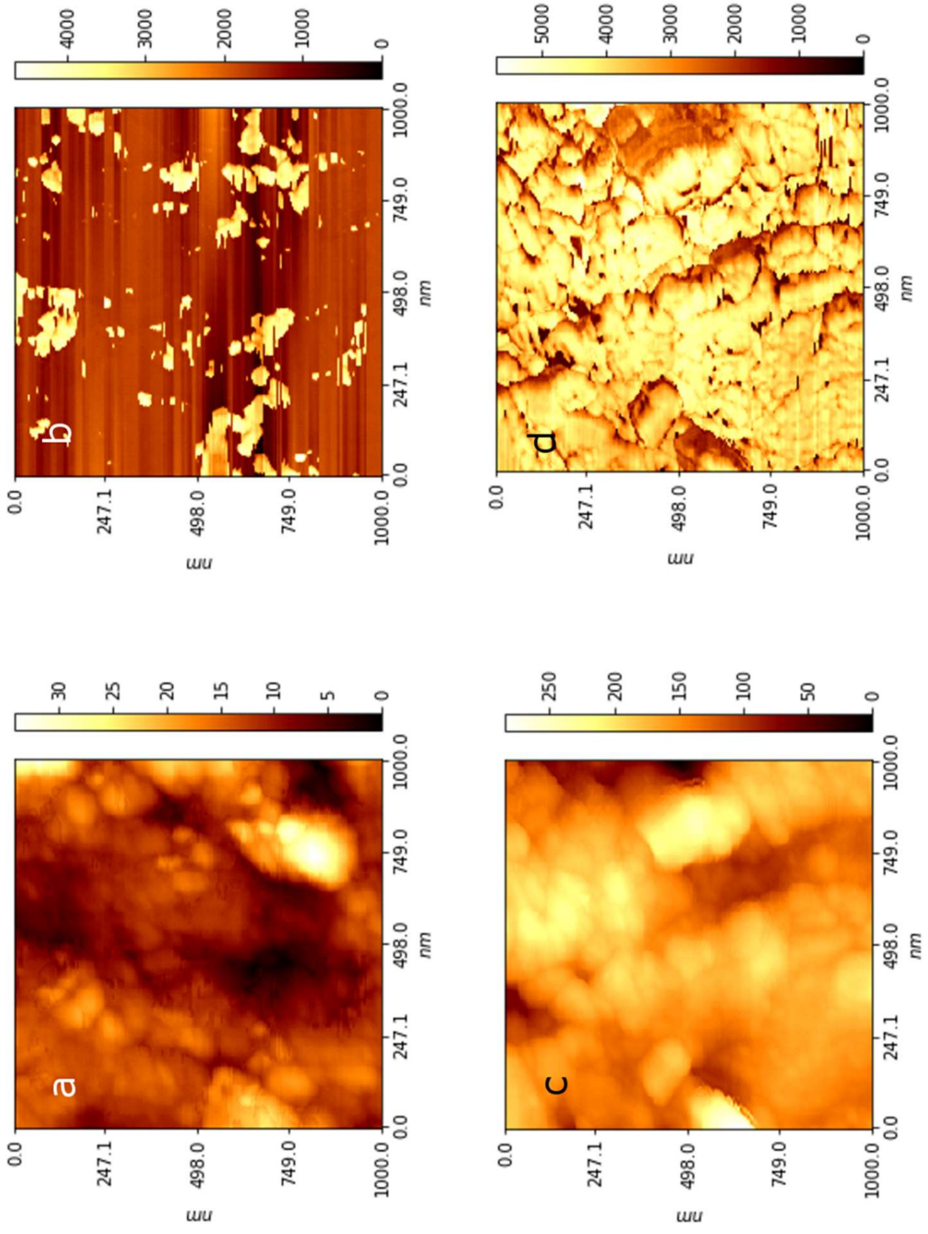

Figure VI.11 The AFM height (a,c) and phase (b,d) image of the repair film generated with S0 (a,b) and S5(c,d). The unit of the color bars in a,c was nm, in b,d it was mV.

Raman analysis showed only two peaks for both tooth enamel and the repair films (Figure 12). This figure plots the light intensity versus the light wavelength change due to Raman shift. This Raman shift was caused by the absorption and emission of photons by the chemical structure of the repair agents. In figure 5, two peaks were observed, one on the protective films and one on the enamel, both of them resulted from the $-PO_4$ group[322]. No additional chemicals were detected from the Raman spectrum, meaning that there are no other phospho- related chemical groups present on the sample surfaces.

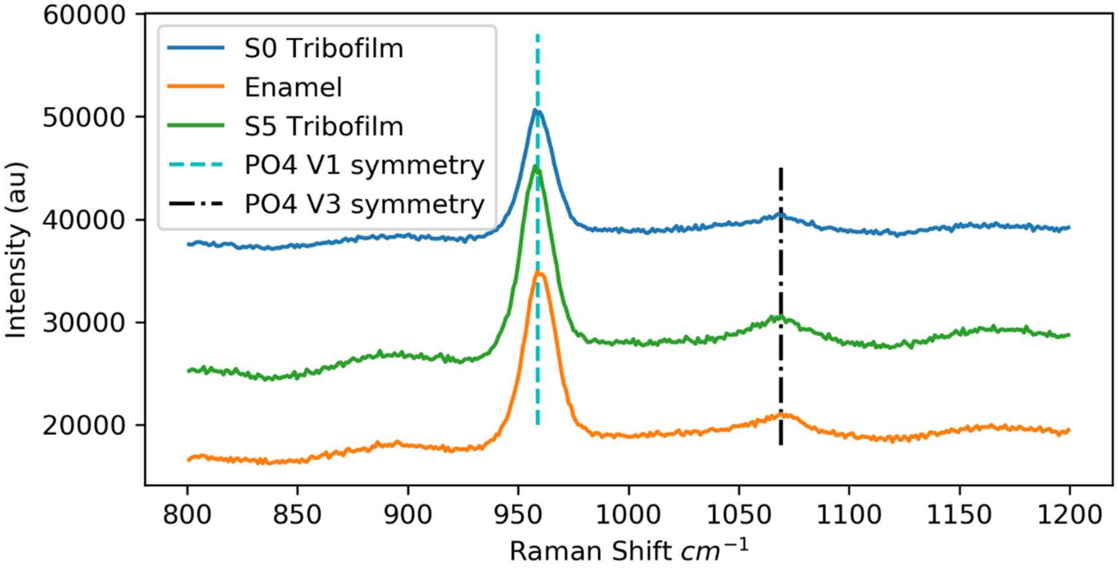

Figure VI.12 The Raman spectra collected from the enamel surface and the repair film generated from S0 and S5. Two peaks resulted from the phosphate groups

In the scratch test, the generated films' scratch resistance was equal to or higher than the enamel of the tooth itself (Figure 13). The scratches from the steel needle caused a loss of materials from both the tooth surface and the repair film surface. However, the repair film was not removed or exfoliated back to the depth of the sample's surface despite the scratching. Compared to the deep groove scratched onto the unprotected enamel surface, this repair film showed good hardness and wear resistance.

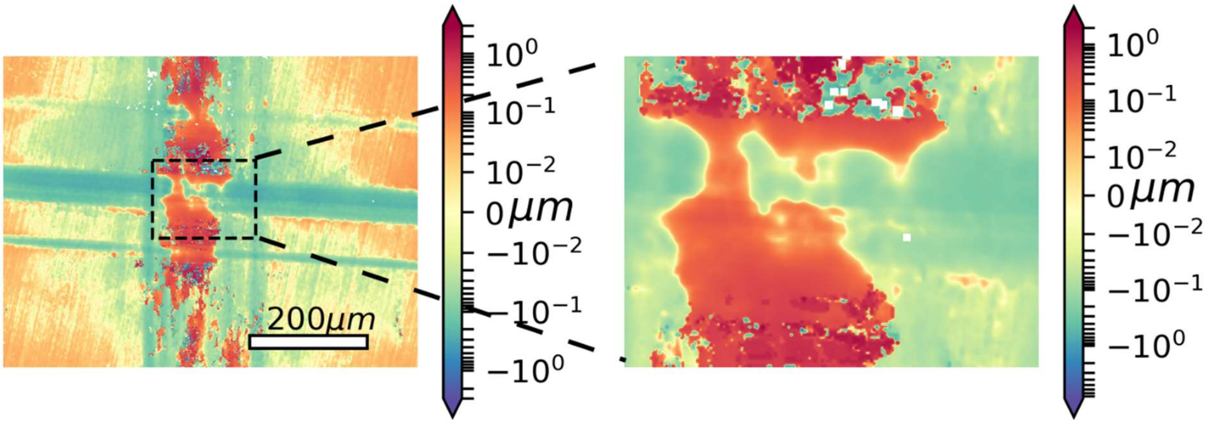

Figure VI.13 The scratch test of the repair film generated by S5. The red color shows the repair film. After the scratch test, part of the film is still present while a deep groove was formed on the enamel surface next to the repair film.

The appearance of a crack on the tip of one of the "pin" teeth allowed characterization of the depth of penetration of the repair material into the enamel instead of only on the surface using micro X-ray CT. In Figure 14, the density distribution of the Zr element was overlaid on the reconstructed tooth image. This "pin" tooth was used in the rubbing-mastication process with the S5 agent. On the contact surface, a film was formed that wrapped around the tip of the tooth. In addition to that, the Zr element was detected inside the cracks to a depth of about $2\mu m$.

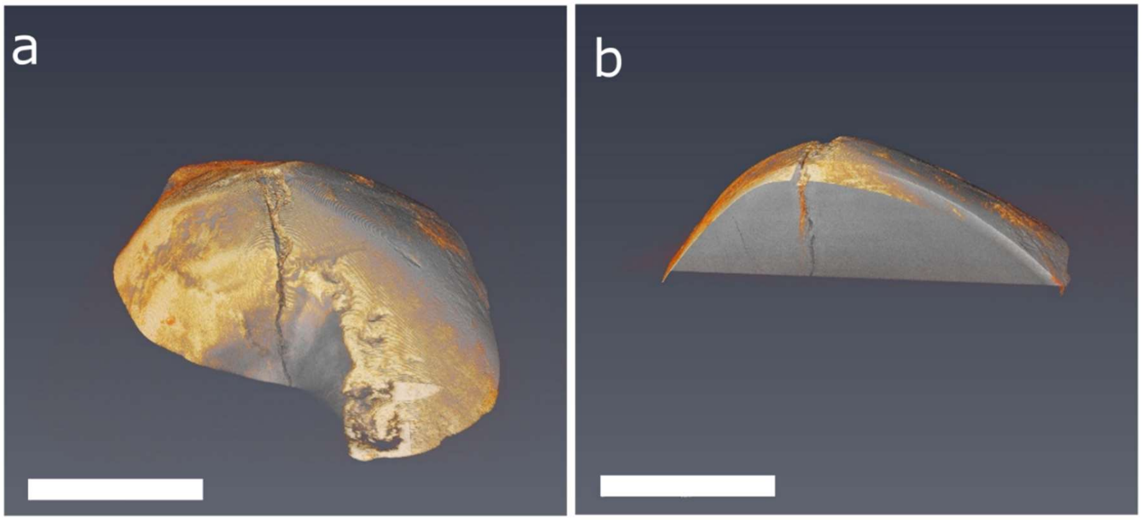

Figure VI.14 The 3D rendering of the "pin" tooth after the rubbing-mastication process with repair agent S5. The distribution of the Zr element calculated from the dual energy k-edge technique was rendered as a golden color. a) the tip of the tooth. b) the cross-section of tooth

Tribomastication with all repair agents resulted in a protective film being added to the enamel. The lowest concentration of α-ZrP produced the thinnest film, which also appeared as flakes on the surface of the enamel. The highest concentration of α-ZrP produced the thickest film but the distribution was very uneven. A pilot assessment of whether the film could be scratched off revealed that this film was resistant to scratching and that the generation of this film prevented wear on the tooth. The thickness and coverage of this repair film was controlled by manipulating the amount of HAP nanoparticles. With increased amounts of HAP, the thickness of the generated repair film was increased. With repair agent S0, the film thickness was only around 100nm, but increased to $2\mu m$ when the HAP:ZrP mass ratio was increased to 1:1 in the case of S10. The coverage of the repair film was also changed by this mass ratio. In the case of S0, a continuous film was produced and the sample S2.5 and S5 generated repair films that almost fully covered the wear track. Furthermore, when the ratio of α-ZrP and HAP increased to 1:2 in mass ratio, the repair film did not form at all. The addition of too much HAP nanoparticles caused the material to lose its rubbing-film forming properties. Because of this, we concluded that the S5 is a good compromise between film coverage and film thickness.

The AFM result provided some insight to the mechanism of the protective film generation. The particle size observed under AFM images (100nm) were smaller than the α-ZrP size in the repair agent (1μm) [299]. This means the generation of a protective film was not a direct deposition of the α-ZrP particles. Because the intercalation process decreased the Van der Waals force between the α-ZrP layers[327], they can be more readily exfoliated by the shear force during the rubbing-mastication process. These exfoliated functionalized 2-dimensional sheets thus became the building blocks of the repair film. The inclusion of HAP nanoparticles not only changed the micro-structure of the resulting repair film, but instead of a flaky aggregation of particles, a more regular cellular like structure was formed. This cellular structure consisted of grains with almost identical sizes, very likely to be the HAP nanoparticles. The HAP nanoparticles survived the rubbing-mastication process and were “glued” together by the “sticky” M600 attached α-ZrP. This further explained why the inclusion of HAP nanoparticles increased the thickness of the film but decreased the coverage. The HAP nanoparticles therefore cannot form a repair film without the intercalated α-ZrP. Thus, the higher concentration of HAP decreased the possibility of intercalated α-ZrP contacting the tooth surface. In addition to that, the Raman spectra showed that the generated film did not introduce any foreign inorganic functional groups on the surface of the teeth. The tribo-chemical process was known to chemically alter the phosphate group[290].

Based on these results, we propose the following repair film forming mechanism for this tooth repair agent. For the pure intercalated α-ZrP, the nanoparticles were exfoliated and broken down by the rubbing-mechanical force. Then, the polymer chains attached to the exfoliated nanoparticles reattached those exfoliated layers under shear. When polymer chains were ground together by the mechanical force, the polymerization process occurred[333–335]. This mechanochemical polymerization process appears to be the driving force for the growth of the repair film. When HAP nanoparticles are introduced, the polymer chain further interacts with the HAP crystals and "glues" the HAP crystals onto the tooth surface, forming a thick coherent film. This cohesiveness of the formed protective film also provides one explanation for its good strength. The micro-CT results further indicated that this repair mechanism may work in the enamel surface cracks as well as on the enamel surface.

6.2.5 Summary

In this research, a simple one-step procedure to reduce wear and repair teeth was developed. The formation of a protective film was made possible through mechanical rubbing (chewing) of materials consisting of nanoparticles, polymers, and biomaterials for mineralization. After rubbing (simulated mastication) between two teeth, the tooth repair agent formed a film with a thickness up to $2\mu m$. The formed repair film has a hardness comparable to the enamel surface. In addition to surface repair, this new agent can enter cracks on the enamel surface. The formation of such protective films may be attributed to the affinity between the polyether and HAP with the tooth enamel. Other polyether modified nanoparticles may also have the potential to form a protective film on the enamel surface. This research presents a new concept and method to prevent enamel wear or repair teeth through chewing.

CHAPTER VII

CONCLUSIONS AND FUTURE RECOMMENDATION

7.1 Conclusions

This thesis research has been focused to obtain the fundamental understanding of nanolubricants under working conditions. To achieve the goal, a methodology that enables *in situ* detection of a rubbing pair was developed. The properties and performance of nanoluricants were studied using such approach. The resulting tribochemical products as tribofilms were investigated. Specifically, three areas of investigation were conducted detailed in the following.

The *in situ* tribo-electrochemical methods were developed for the evaluation of nanolubricants. A configuration consisting of a disc-on-disc tribometer and an impedance analyzer was designed and built. Using this system, triboelectrochemical evaluation of electrical conductivity and the thickness of lubricating oils against friction was made possible.

Using the above mentioned system, the dynamic properties and thermal performance of working lubricating oils were studied. Experimental results revealed the non-ohmic behavior of a lubricating film in the hydrodynamic regime. Properties of lubricants and testing conditions are factors affecting the performance. To probe the thermal properties, the system electrically measured the oil film thickness against temperature while the lubricating oil impendence was recorded. Experimental data was used for calculating dynamic thermal conductivity using a dimensional analysis. Results showed that the dynamic thermal conductivity of mineral oil was 0.25mW/K and Poly-alpha-olefin (PAO) oil was 0.2mW/K when the speed/load of the tribometer was 100cm/Ns. The results indicate that commercial lubricants for conventional vehicles could be improved in order to be adapted to electric vehicles. This methodology was the foundation of other investigation in this research.

Finally, amphiphilic nanolubricant's tribochemical reactions and kinetics were investigated. The amphiphilic nanolubricant was based on exfoliated-surface-modified nanoparticles of α-ZrP. The tribochemical reactions induced by the tribological contact resulted the formation of a layered pyrophosphate tribofilm. Such a film reduced wear for 90% and friction 40% against the base oil. The kinetics of the growth appear to be in two stages. One is quadratic growth where the growth rate is proportional to the thickness. The other is the stable phase when the thickness of a tribofilm is stabilized. The temperature has great influence on the growth rate. The coefficient of friction influenced both the wear and growth behaviors. When the coefficient of friction is increased, both the growth and wear increase. This balanced growth of tribofilm leading to stable electrical contact.

To summarize, this research has three key achievements:

1) Developed an integrated tribo-electrochemical methodology to investigate physical and tribochemical properties for nanolubricants.
2) Discovered the dynamic and thermal properties of a working lubricant.

3) Discovered the tribochemical reactions and kinetics of a nanolubricant consisting modified α-ZrP nanoparticles.

7.2 Future recommendation

This thesis research presented potential in its methodology and enabling study in nanolubricants. The improvement of the integrated tribotesting method can improve the quality of measurement, as well as this capability. The method developed in this research was based on the assumed physical model to simplify the data analysis process. The simplicity also means that the true physical quantity may deviate from the measurement. To solve these issues, a few steps can be made in the future:

- Establish a direct calibration method designed for this method. Currently, only the impedance analyzer is calibrated. Others against properties with samples of known quantities can further validate testing. . The thickness measurement of a lubricant can be calibrated with a designated gap. The resistivity can be calibrated with a thin film with known value.
- Improve the electronics can expand the number of physical properties tested. Currently, the single frequency impedance measurement was used. This limited testing in non-polar lubricants with simple electrochemical characteristics. If the response of multiple frequencies is measured simultaneously, the capability of this method can be improved.
- Functionalized nanoparticles should be further studied as potential lubricant additives.

REFERENCES

[1] Dai, W., Kheireddin, B., Gao, H., and Liang, H., 2016, “Roles of Nanoparticles in Oil Lubrication,” Tribol. Int., **102**, pp. 88–98.

[2] Gulzar, M., Masjuki, H. H., Kalam, M. A., Varman, M., Zulkifli, N. W. M., Mufti, R. A., and Zahid, R., 2016, “Tribological Performance of Nanoparticles as Lubricating Oil Additives,” J. Nanoparticle Res., **18**(8), p. 223.

[3] Choa, S.-H., Ludema, K. C., Potter, G. E., Dekoven, B. M., Morgan, T. A., and Kar, K. K., 1994, “A Model of the Dynamics of Boundary Film Formation,” Wear, **177**(1), pp. 33–45.

[4] Georges, J. M., Martin, J. M., Mathia, T., Kapsa, P., Meille, G., and Montes, H., 1979, “Mechanism of Boundary Lubrication with Zinc Dithiophosphate,” Wear, **53**(1), pp. 9–34.

[5] Bakunin, V. N., Suslov, A. Yu., Kuzmina, G. N., Parenago, O. P., and Topchiev, A. V., 2004, “Synthesis and Application of Inorganic Nanoparticles as Lubricant Components – a Review,” J. Nanoparticle Res., **6**(2), pp. 273–284.

[6] Ghaednia, H., and Jackson, R. L., 2013, “The Effect of Nanoparticles on the Real Area of Contact, Friction, and Wear,” J. Tribol., **135**(4).

[7] Ghaednia, H., Babaei, H., Jackson, R. L., Bozack, M. J., and Khodadadi, J. M., 2013, “The Effect of Nanoparticles on Thin Film Elasto-Hydrodynamic Lubrication,” Appl. Phys. Lett., **103**(26), p. 263111.

[8] Parsaeian, P., Ghanbarzadeh, A., Van Eijk, M. C. P., Nedelcu, I., Morina, A., and Neville, A., 2017, “Study of the Interfacial Mechanism of ZDDP Tribofilm in Humid Environment and Its Effect on Tribochemical Wear; Part II: Numerical,” Tribol. Int., **107**, pp. 33–38.

[9] Peña-Parás, L., Taha-Tijerina, J., Garza, L., Maldonado-Cortés, D., Michalczewski, R., and Lapray, C., 2015, “Effect of CuO and Al2O3 Nanoparticle Additives on the Tribological Behavior of Fully Formulated Oils,” Wear, **332–333**, pp. 1256–1261.

[10] Kang, Y., Peng, D., Chen, C., Chang, Y., and Chang, S., 2010, “Size Effects of SiO2 Nanoparticles as Oil Additives on Tribology of Lubricant,” Ind. Lubr. Tribol., **62**(2), pp. 111–120.

[11] Alves, S. M., Mello, V. S., Faria, E. A., and Camargo, A. P. P., 2016, “Nanolubricants Developed from Tiny CuO Nanoparticles,” Tribol. Int., **100**, pp. 263–271.

[12] Hernández Battez, A., González, R., Viesca, J. L., Fernández, J. E., Díaz Fernández, J. M., Machado, A., Chou, R., and Riba, J., 2008, “CuO, ZrO2 and ZnO Nanoparticles as Antiwear Additive in Oil Lubricants,” Wear, **265**(3), pp. 422–428.

[13] Kato, H., and Komai, K., 2007, “Tribofilm Formation and Mild Wear by Tribo-Sintering of Nanometer-Sized Oxide Particles on Rubbing Steel Surfaces,” Wear, **262**(1–2), pp. 36–41.

[14] Fan, X., Li, G., Guo, Y., Zhang, L., Xu, Y., Zhao, F., and Zhang, G., 2020, “Role of Reinforcement Types and Silica Nanoparticles on Tribofilm Growth at PTFE-Steel Interface,” Tribol. Int., **143**, p. 106035.

[15] Dassenoy, F., Jenei, I. Z., Pavan, S., Galipaud, J., Thersleff, T., Wieber, S., Hagemann, M., and Ness, D., 2020, “Performance and Lubrication Mechanism of New TiO2 Particle-Based High-Performance Lubricant Additives,” Tribol. Trans., **0**(ja), pp. 1–16.

[16] GAO, C., WANG, Y., 2, XIANG, L., HU, D., 2, and PAN, Z., 2, 2013, “Tribochemical Properties of Fe3O4 Nanoparticles with Hexagonal Morphology in Lubricating Oil,” J. Chin. Ceram. Soc., **41**(10), pp. 1339–1346.

[17] Xiang, L., Gao, C., Wang, Y., Pan, Z., and Hu, D., 2014, “Tribological and Tribochemical Properties of Magnetite Nanoflakes as Additives in Oil Lubricants,” Particuology, **17**, pp. 136–144.

[18] Gao, F., and Liang, H., 2011, “Transformable Oxidation of Tantalum in Electrochemical Mechanical Polishing (ECMP),” J. Electron. Mater., **40**(2), pp. 134–140.

[19] He, X., Chen, Y., Zhao, H., Sun, H., Lu, X., and Liang, H., 2013, “Y 2 O 3 Nanosheets as Slurry Abrasives for Chemical-Mechanical Planarization of Copper,” Friction, **1**(4), pp. 327–332.

[20] Joo, S., and Liang, H., 2013, “In Situ Characterization of Triboelectrochemical Effects on Topography of Patterned Copper Surfaces,” J. Electron. Mater., **42**(6), pp. 979–987.

[21] Xu, W., Ma, L., Chen, Y., and Liang, H., 2018, “Mechano-Oxidation during Cobalt Polishing,” Wear, **416**, pp. 36–43.

[22] Zhang, P., He, H., Chen, C., Xiao, C., Chen, L., and Qian, L., 2017, “Effect of Abrasive Particle Size on Tribochemical Wear of Monocrystalline Silicon,” Tribol. Int., **109**, pp. 222–228.

[23] Chinas-Castillo, F., and Spikes, H. A., 2000, “Film Formation by Colloidal Overbased Detergents in Lubricated Contacts,” Tribol. Trans., **43**(3), pp. 357–366.

[24] Topolovec-Miklozic, K., Forbus, T. R., and Spikes, H., 2008, “Film Forming and Friction Properties of Overbased Calcium Sulphonate Detergents,” Tribol. Lett., **29**(1), pp. 33–44.

[25] Chin˜as-Castillo, F., and Spikes, H. A., 2003, “Mechanism of Action of Colloidal Solid Dispersions,” J. Tribol., **125**(3), pp. 552–557.

[26] Yu, H. L., Xu, Y., Shi, P. J., Xu, B. S., Wang, X. L., Liu, Q., and Wang, H. M., 2008, “Characterization and Nano-Mechanical Properties of Tribofilms Using Cu Nanoparticles as Additives,” Surf. Coat. Technol., **203**(1–2), pp. 28–34.

[27] Kumara, C., Luo, H., Leonard, D. N., Meyer, H. M., and Qu, J., 2017, “Organic-Modified Silver Nanoparticles as Lubricant Additives,” ACS Appl. Mater. Interfaces, **9**(42), pp. 37227–37237.

[28] Kumara, C., Leonard, D. N., Meyer, H. M., Luo, H., Armstrong, B. L., and Qu, J., 2018, “Palladium Nanoparticle-Enabled Ultrathick Tribofilm with Unique Composition,” ACS Appl. Mater. Interfaces, **10**(37), pp. 31804–31812.

[29] Liu, R., Wei, X., Tao, D., and Zhao, Y., 2010, “Study of Preparation and Tribological Properties of Rare Earth Nanoparticles in Lubricating Oil,” Tribol. Int., **43**(5), pp. 1082–1086.

[30] Wu, X., Gong, K., Zhao, G., Lou, W., Wang, X., and Liu, W., 2018, “Surface Modification of MoS2 Nanosheets as Effective Lubricant Additives for Reducing Friction and Wear in Poly-α-Olefin,” Ind. Eng. Chem. Res., **57**(23), pp. 8105–8114.

[31] Tannous, J., Dassenoy, F., Lahouij, I., Le Mogne, T., Vacher, B., Bruhács, A., and Tremel, W., 2011, “Understanding the Tribochemical Mechanisms of IF-MoS2 Nanoparticles Under Boundary Lubrication,” Tribol. Lett., **41**(1), pp. 55–64.

[32] Wu, X., Gong, K., Zhao, G., Lou, W., Wang, X., and Liu, W., 2018, “MoS2/WS2 Quantum Dots as High-Performance Lubricant Additive in Polyalkylene Glycol for Steel/Steel Contact at Elevated Temperature,” Adv. Mater. Interfaces, **5**(1), p. 1700859.

[33] Kumari, S., Gusain, R., Kumar, N., and Khatri, O. P., 2016, “PEG-Mediated Hydrothermal Synthesis of Hierarchical Microspheres of MoS2 Nanosheets and Their Potential for Lubrication Application,” J. Ind. Eng. Chem., **42**, pp. 87–94.

[34] Ripoll, M. R., Tomala, A., Gabler, C., Dražić, G., Pirker, L., and Remškar, M., 2018, “In Situ Tribochemical Sulfurization of Molybdenum Oxide Nanotubes,” Nanoscale, **10**(7), pp. 3281–3290.

[35] Rodríguez Ripoll, M., Tomala, A. M., Pirker, L., and Remškar, M., 2020, “In-Situ Formation of MoS2 and WS2 Tribofilms by the Synergy Between Transition Metal Oxide Nanoparticles and Sulphur-Containing Oil Additives,” Tribol. Lett., **68**(1), p. 41.

[36] Morita, Y., Onodera, T., Suzuki, A., Sahnoun, R., Koyama, M., Tsuboi, H., Hatakeyama, N., Endou, A., Takaba, H., Kubo, M., Del Carpio, C. A., Shin-yoshi, T., Nishino, N., Suzuki, A., and Miyamoto, A., 2008, “Development of a New Molecular Dynamics Method for Tribochemical Reaction and Its Application to Formation Dynamics of MoS2 Tribofilm,” Appl. Surf. Sci., **254**(23), pp. 7618–7621.

[37] Chinas-Castillo, F., and Spikes, H. A., 2003, “Mechanism of Action of Colloidal Solid Dispersions,” J. Tribol., **125**(3), pp. 552–557.

[38] Kalin, M., Kogovšek, J., and Remškar, M., 2012, “Mechanisms and Improvements in the Friction and Wear Behavior Using MoS2 Nanotubes as Potential Oil Additives,” Wear, **280–281**, pp. 36–45.

[39] Rabaso, P., Ville, F., Dassenoy, F., Diaby, M., Afanasiev, P., Cavoret, J., Vacher, B., and Le Mogne, T., 2014, “Boundary Lubrication: Influence of the Size and Structure of Inorganic Fullerene-like MoS2 Nanoparticles on Friction and Wear Reduction,” Wear, **320**, pp. 161–178.

[40] Berne, B. J., and Pecora, R., 2000, *Dynamic Light Scattering: With Applications to Chemistry, Biology, and Physics*, Courier Corporation.

[41] Lin, J., Wang, L., and Chen, G., 2011, “Modification of Graphene Platelets and Their Tribological Properties as a Lubricant Additive,” Tribol. Lett., **41**(1), pp. 209–215.

[42] Li, B., Wang, X., Liu, W., and Xue, Q., 2006, “Tribochemistry and Antiwear Mechanism of Organic–Inorganic Nanoparticles as Lubricant Additives,” Tribol. Lett., **22**(1), pp. 79–84.

[43] Xue, Q., Liu, W., and Zhang, Z., 1997, "Friction and Wear Properties of a Surface-Modified TiO2 Nanoparticle as an Additive in Liquid Paraffin," Wear, **213**(1), pp. 29–32.

[44] Zhang, L., Chen, L., Wan, H., Chen, J., and Zhou, H., 2011, "Synthesis and Tribological Properties of Stearic Acid-Modified Anatase (TiO2) Nanoparticles," Tribol. Lett., **41**(2), pp. 409–416.

[45] Wright, R. A. E., Wang, K., Qu, J., and Zhao, B., 2016, "Oil-Soluble Polymer Brush Grafted Nanoparticles as Effective Lubricant Additives for Friction and Wear Reduction," Angew. Chem. Int. Ed., **55**(30), pp. 8656–8660.

[46] Ingole, S., Charanpahari, A., Kakade, A., Umare, S. S., Bhatt, D. V., and Menghani, J., 2013, "Tribological Behavior of Nano TiO2 as an Additive in Base Oil," Wear, **301**(1), pp. 776–785.

[47] Bogunovic, L., Zuenkeler, S., Toensing, K., and Anselmetti, D., 2015, "An Oil-Based Lubrication System Based on Nanoparticular TiO<Subscript>2</Subscript> with Superior Friction and Wear Properties," Tribol. Lett., **59**(2), p. 29.

[48] Kim, D., and Archer, L. A., 2011, "Nanoscale Organic−Inorganic Hybrid Lubricants," Langmuir, **27**(6), pp. 3083–3094.

[49] Kheireddin, B. A., Lu, W., Chen, I.-C., and Akbulut, M., 2013, "Inorganic Nanoparticle-Based Ionic Liquid Lubricants," Wear, **303**(1), pp. 185–190.

[50] Seymour, B. T., Wright, R. A., Parrott, A. C., Gao, H., Martini, A., Qu, J., Dai, S., and Zhao, B., 2017, "Poly (Alkyl Methacrylate) Brush-Grafted Silica Nanoparticles as Oil Lubricant Additives: Effects of Alkyl Pendant Groups on Oil Dispersibility, Stability, and Lubrication Property," ACS Appl. Mater. Interfaces, **9**(29), pp. 25038–25048.

[51] Li, X., Cao, Z., Zhang, Z., and Dang, H., 2006, "Surface-Modification in Situ of Nano-SiO2 and Its Structure and Tribological Properties," Appl. Surf. Sci., **252**(22), pp. 7856–7861.

[52] Xie, H., Jiang, B., He, J., Xia, X., and Pan, F., 2016, "Lubrication Performance of MoS2 and SiO2 Nanoparticles as Lubricant Additives in Magnesium Alloy-Steel Contacts," Tribol. Int., **93**, pp. 63–70.

[53] Sui, T., Song, B., Zhang, F., and Yang, Q., 2015, "Effect of Particle Size and Ligand on the Tribological Properties of Amino Functionalized Hairy Silica Nanoparticles As an Additive to Polyalphaolefin," J Nanomater., **16**(1), p. 427:427-427:427.

[54] López, T. D.-F., González, A. F., Reguero, Á. D., Matos, M., Díaz-García, M. E., and Badía-Laíño, R., 2015, "Engineered Silica Nanoparticles as Additives in Lubricant Oils," Sci. Technol. Adv. Mater., **16**(5), p. 055005.

[55] Sui, T., Ding, M., Ji, C., Yan, S., Wei, J., Wang, A., Zhao, F., and Fei, J., 2018, "Dispersibility and Rheological Behavior of Functionalized Silica Nanoparticles as Lubricant Additives," Ceram. Int.

[56] Sui, T., Song, B., Zhang, F., and Yang, Q., 2016, "Effects of Functional Groups on the Tribological Properties of Hairy Silica Nanoparticles as an Additive to Polyalphaolefin," RSC Adv., **6**(1), pp. 393–402.

[57] Sui, T., Song, B., Wen, Y., and Zhang, F., 2016, "Bifunctional Hairy Silica Nanoparticles as High-Performance Additives for Lubricant," Sci. Rep., **6**, p. 22696.

[58] Li, W., Zheng, S., Cao, B., and Ma, S., 2011, “Friction and Wear Properties of ZrO<Subscript>2</Subscript>/SiO<Subscript>2</Subscript> Composite Nanoparticles,” J. Nanoparticle Res., **13**(5), pp. 2129–2137.

[59] Jiao, D., Zheng, S., Wang, Y., Guan, R., and Cao, B., 2011, “The Tribology Properties of Alumina/Silica Composite Nanoparticles as Lubricant Additives,” Appl. Surf. Sci., **257**(13), pp. 5720–5725.

[60] Alves, S. M., Barros, B. S., Trajano, M. F., Ribeiro, K. S. B., and Moura, E., 2013, “Tribological Behavior of Vegetable Oil-Based Lubricants with Nanoparticles of Oxides in Boundary Lubrication Conditions,” Tribol. Int., **65**, pp. 28–36.

[61] Chen, Q., Zheng, S., Yang, S., Li, W., Song, X., and Cao, B., 2012, “Enhanced Tribology Properties of ZnO/Al<Subscript>2</Subscript>O<Subscript>3</Subscript> Composite Nanoparticles as Liquid Lubricating Additives,” J. Sol-Gel Sci. Technol., **61**(3), pp. 501–508.

[62] Zhou, G., Zhu, Y., Wang, X., Xia, M., Zhang, Y., and Ding, H., 2013, “Sliding Tribological Properties of 0.45% Carbon Steel Lubricated with Fe3O4 Magnetic Nano-Particle Additives in Baseoil,” Wear, **301**(1), pp. 753–757.

[63] Hu, Z. S., Dong, J. X., and Chen, G. X., 1998, “Study on Antiwear and Reducing Friction Additive of Nanometer Ferric Oxide,” Tribol. Int., **31**(7), pp. 355–360.

[64] Luo, T., Wei, X., Huang, X., Huang, L., and Yang, F., 2014, “Tribological Properties of Al2O3 Nanoparticles as Lubricating Oil Additives,” Ceram. Int., **40**(5), pp. 7143–7149.

[65] Luo, T., Wei, X., Zhao, H., Cai, G., and Zheng, X., 2014, “Tribology Properties of Al2O3/TiO2 Nanocomposites as Lubricant Additives,” Ceram. Int., **40**(7, Part A), pp. 10103–10109.

[66] Zhou, Q., Huang, J., Wang, J., Yang, Z., Liu, S., Wang, Z., and Yang, S., 2015, “Preparation of a Reduced Graphene Oxide/Zirconia Nanocomposite and Its Application as a Novel Lubricant Oil Additive,” RSC Adv., **5**(111), pp. 91802–91812.

[67] Chen, S., Liu, W., and Yu, L., 1998, “Preparation of DDP-Coated PbS Nanoparticles and Investigation of the Antiwear Ability of the Prepared Nanoparticles as Additive in Liquid Paraffin,” Wear, **218**(2), pp. 153–158.

[68] Rosentsveig, R., Gorodnev, A., Feuerstein, N., Friedman, H., Zak, A., Fleischer, N., Tannous, J., Dassenoy, F., and Tenne, R., 2009, “Fullerene-like MoS<Subscript>2</Subscript> Nanoparticles and Their Tribological Behavior,” Tribol. Lett., **36**(2), pp. 175–182.

[69] Joly-Pottuz, L., Dassenoy, F., Belin, M., Vacher, B., Martin, J. M., and Fleischer, N., 2005, “Ultralow-Friction and Wear Properties of IF-WS<Subscript>2</Subscript> under Boundary Lubrication,” Tribol. Lett., **18**(4), pp. 477–485.

[70] Shahar, C., Zbaida, D., Rapoport, L., Cohen, H., Bendikov, T., Tannous, J., Dassenoy, F., and Tenne, R., 2010, “Surface Functionalization of WS2 Fullerene-like Nanoparticles,” Langmuir, **26**(6), pp. 4409–4414.

[71] Moshkovith, A., Perfiliev, V., Verdyan, A., Lapsker, I., Popovitz-Biro, R., Tenne, R., and Rapoport, L., 2007, "Sedimentation of IF-WS2 Aggregates and a Reproducibility of the Tribological Data," Tribol. Int., **40**(1), pp. 117–124.

[72] Jiang, Z., Zhang, Y., Yang, G., Yang, K., Zhang, S., Yu, L., and Zhang, P., 2016, "Tribological Properties of Oleylamine-Modified Ultrathin WS2 Nanosheets as the Additive in Polyalpha Olefin Over a Wide Temperature Range," Tribol. Lett., **61**(3), p. 24.

[73] Wu, J., and Fu, X., 2007, "A Low-Temperature Solvothermal Method to Prepare Hollow Spherical WS2 Nanoparticles Modified by TOA," Mater. Lett., **61**(21), pp. 4332–4335.

[74] Jifen, W., Wensheng, Z., and Guifen, J., 2010, "Preparation and Tribological Properties of Tungsten Disulfide Hollow Spheres Assisted by Methyltrioctylammonium Chloride," Tribol. Int., **43**(9), pp. 1650–1658.

[75] Cizaire, L., Vacher, B., Le Mogne, T., Martin, J. M., Rapoport, L., Margolin, A., and Tenne, R., 2002, "Mechanisms of Ultra-Low Friction by Hollow Inorganic Fullerene-like MoS2 Nanoparticles," Surf. Coat. Technol., **160**(2), pp. 282–287.

[76] Bakunin, V. N., Kuzmina, G. N., Kasrai, M., Parenago, O. P., and Bancroft, G. M., 2006, "Tribological Behavior and Tribofilm Composition in Lubricated Systems Containing Surface-Capped Molybdenum Sulfide Nanoparticles," Tribol. Lett., **22**(3), pp. 289–296.

[77] Koshy, C. P., Rajendrakumar, P. K., and Thottackkad, M. V., 2015, "Evaluation of the Tribological and Thermo-Physical Properties of Coconut Oil Added with MoS2 Nanoparticles at Elevated Temperatures," Wear, **330–331**, pp. 288–308.

[78] Xu, Z. Y., Xu, Y., Hu, K. H., Xu, Y. F., and Hu, X. G., 2015, "Formation and Tribological Properties of Hollow Sphere-like Nano-MoS2 Precipitated in TiO2 Particles," Tribol. Int., **81**, pp. 139–148.

[79] Kang, X., Wang, B., Zhu, L., and Zhu, H., 2008, "Synthesis and Tribological Property Study of Oleic Acid-Modified Copper Sulfide Nanoparticles," Wear, **265**(1), pp. 150–154.

[80] Zhou, J., Wu, Z., Zhang, Z., Liu, W., and Xue, Q., 2000, "Tribological Behavior and Lubricating Mechanism of Cu Nanoparticles in Oil," Tribol. Lett., **8**(4), pp. 213–218.

[81] Yang, G., Chai, S., Xiong, X., Zhang, S., Yu, L., and Zhang, P., 2012, "Preparation and Tribological Properties of Surface Modified Cu Nanoparticles," Trans. Nonferrous Met. Soc. China, **22**(2), pp. 366–372.

[82] Choi, Y., Lee, C., Hwang, Y., Park, M., Lee, J., Choi, C., and Jung, M., 2009, "Tribological Behavior of Copper Nanoparticles as Additives in Oil," Curr. Appl. Phys., **9**(2, Supplement), pp. e124–e127.

[83] Liu, G., Li, X., Qin, B., Xing, D., Guo, Y., and Fan, R., 2004, "Investigation of the Mending Effect and Mechanism of Copper Nano-Particles on a Tribologically Stressed Surface," Tribol. Lett., **17**(4), pp. 961–966.

[84] Viesca, J. L., Hernández Battez, A., González, R., Chou, R., and Cabello, J. J., 2011, "Antiwear Properties of Carbon-Coated Copper Nanoparticles Used as an Additive to a Polyalphaolefin," Tribol. Int., **44**(7), pp. 829–833.

[85] Chen, Y., Zhang, Y., Zhang, S., Yu, L., Zhang, P., and Zhang, Z., 2013, “Preparation of Nickel-Based Nanolubricants via a Facile In Situ One-Step Route and Investigation of Their Tribological Properties,” Tribol. Lett., **51**(1), pp. 73–83.

[86] Qiu, S., Zhou, Z., Dong, J., and Chen, G., 2001, “Preparation of Ni Nanoparticles and Evaluation of Their Tribological Performance as Potential Additives in Oils,” J. Tribol., **123**(3), pp. 441–443.

[87] Chou, R., Battez, A. H., Cabello, J. J., Viesca, J. L., Osorio, A., and Sagastume, A., 2010, “Tribological Behavior of Polyalphaolefin with the Addition of Nickel Nanoparticles,” Tribol. Int., **43**(12), pp. 2327–2332.

[88] Sun, L., Tao, X., Zhao, Y., and Zhang, Z., 2010, “Synthesis and Tribology Properties of Stearate-Coated Ag Nanoparticles,” Tribol. Trans., **53**(2), pp. 174–178.

[89] Sun, L., Zhang, Z. J., Wu, Z. S., and Dang, H. X., 2004, “Synthesis and Characterization of DDP Coated Ag Nanoparticles,” Mater. Sci. Eng. A, **379**(1), pp. 378–383.

[90] Kolodziejczyk, L., Martínez-Martínez, D., Rojas, T. C., Fernández, A., and Sánchez-López, J. C., 2007, “Surface-Modified Pd Nanoparticles as a Superior Additive for Lubrication,” J. Nanoparticle Res., **9**(4), pp. 639–645.

[91] Huang, H. D., Tu, J. P., Gan, L. P., and Li, C. Z., 2006, “An Investigation on Tribological Properties of Graphite Nanosheets as Oil Additive,” Wear, **261**(2), pp. 140–144.

[92] Zhang, W., Zhou, M., Zhu, H., Tian, Y., Wang, K., Wei, J., Ji, F., Li, X., Li, Z., Peng Zhang, and Wu, D., 2011, “Tribological Properties of Oleic Acid-Modified Graphene as Lubricant Oil Additives,” J. Phys. Appl. Phys., **44**(20), p. 205303.

[93] Choudhary, S., Mungse, H. P., and Khatri, O. P., 2012, “Dispersion of Alkylated Graphene in Organic Solvents and Its Potential for Lubrication Applications,” J. Mater. Chem., **22**(39), pp. 21032–21039.

[94] Yang, J., Xia, Y., Song, H., Chen, B., and Zhang, Z., 2017, “Synthesis of the Liquid-like Graphene with Excellent Tribological Properties,” Tribol. Int., **105**, pp. 118–124.

[95] Lee, J., Cho, S., Hwang, Y., Lee, C., and Kim, S. H., 2007, “Enhancement of Lubrication Properties of Nano-Oil by Controlling the Amount of Fullerene Nanoparticle Additives,” Tribol. Lett., **28**(2), pp. 203–208.

[96] Joly-Pottuz, L., Vacher, B., Ohmae, N., Martin, J. M., and Epicier, T., 2008, “Anti-Wear and Friction Reducing Mechanisms of Carbon Nano-Onions as Lubricant Additives,” Tribol. Lett., **30**(1), pp. 69–80.

[97] Zin, V., Agresti, F., Barison, S., Colla, L., Mercadelli, E., Fabrizio, M., and Pagura, C., 2014, “Tribological Properties of Engine Oil with Carbon Nano-Horns as Nano-Additives,” Tribol. Lett., **55**(1), pp. 45–53.

[98] Nunn, N., Mahbooba, Z., Ivanov, M. G., Ivanov, D. M., Brenner, D. W., and Shenderova, O., 2015, “Tribological Properties of Polyalphaolefin Oil Modified with Nanocarbon Additives,” Diam. Relat. Mater., **54**, pp. 97–102.

[99] Sunqing, Q., Junxiu, D., and Guoxu, C., 2000, "Wear and Friction Behaviour of CaCO3 Nanoparticles Used as Additives in Lubricating Oils," Lubr. Sci., **12**(2), pp. 205–212.

[100] Zhang, M., Wang, X., Fu, X., and Xia, Y., 2009, "Performance and Anti-Wear Mechanism of CaCO3 Nanoparticles as a Green Additive in Poly-Alpha-Olefin," Tribol. Int., **42**(7), pp. 1029–1039.

[101] Peri, J. B., 1958, "The State of Dispersion of Detergent Additives in Lubricating Oil and Other Hydrocarbons," J. Am. Oil Chem. Soc., **35**(3), pp. 110–117.

[102] Dong, J. X., and Hu, Z. S., 1998, "A Study of the Anti-Wear and Friction-Reducing Properties of the Lubricant Additive, Nanometer Zinc Borate," Tribol. Int., **31**(5), pp. 219–223.

[103] Song, X., Zheng, S., Zhang, J., Li, W., Chen, Q., and Cao, B., 2012, "Synthesis of Monodispersed ZnAl2O4 Nanoparticles and Their Tribology Properties as Lubricant Additives," Mater. Res. Bull., **47**(12), pp. 4305–4310.

[104] Zhang, Z., Liu, W., and Xue, Q., 1998, "Study on Lubricating Mechanisms of La(OH)3 Nanocluster Modified by Compound Containing Nitrogen in Liquid Paraffin," Wear, **218**(2), pp. 139–144.

[105] Hu, Z. S., Dong, J. X., Chen, G. X., and He, J. Z., 2000, "Preparation and Tribological Properties of Nanoparticle Lanthanum Borate," Wear, **243**(1), pp. 43–47.

[106] Zhou, J., Wu, Z., Zhang, Z., Liu, W., and Dang, H., 2001, "Study on an Antiwear and Extreme Pressure Additive of Surface Coated LaF3 Nanoparticles in Liquid Paraffin," Wear, **249**(5), pp. 333–337.

[107] Kumari, S., Sharma, O. P., Gusain, R., Mungse, H. P., Kukrety, A., Kumar, N., Sugimura, H., and Khatri, O. P., 2015, "Alkyl-Chain-Grafted Hexagonal Boron Nitride Nanoplatelets as Oil-Dispersible Additives for Friction and Wear Reduction," ACS Appl. Mater. Interfaces, **7**(6), pp. 3708–3716.

[108] Farrokhpay, S., 2009, "A Review of Polymeric Dispersant Stabilisation of Titania Pigment," Adv. Colloid Interface Sci., **151**(1), pp. 24–32.

[109] Rabaso, P., Dassenoy, F., Ville, F., Diaby, M., Vacher, B., Mogne, T. L., Belin, M., and Cavoret, J., 2014, "An Investigation on the Reduced Ability of IF-MoS<Subscript>2</Subscript> Nanoparticles to Reduce Friction and Wear in the Presence of Dispersants," Tribol. Lett., **55**(3), pp. 503–516.

[110] Nakayama, N., and Hayashi, T., 2008, "Preparation of TiO2 Nanoparticles Surface-Modified by Both Carboxylic Acid and Amine: Dispersibility and Stabilization in Organic Solvents," Colloids Surf. Physicochem. Eng. Asp., **317**(1), pp. 543–550.

[111] Li, Z., and Zhu, Y., 2003, "Surface-Modification of SiO2 Nanoparticles with Oleic Acid," Appl. Surf. Sci., **211**(1), pp. 315–320.

[112] Li, C.-C., and Chang, M.-H., 2004, "Colloidal Stability of CuO Nanoparticles in Alkanes via Oleate Modifications," Mater. Lett., **58**(30), pp. 3903–3907.

[113] Jifen, W., Wensheng, Z., and Guifen, J., 2010, "Preparation and Tribological Properties of Tungsten Disulfide Hollow Spheres Assisted by Methyltrioctylammonium Chloride," Tribol. Int., **43**(9), pp. 1650–1658.

[114] Ma, X., Lee, N.-H., Oh, H.-J., Kim, J.-W., Rhee, C.-K., Park, K.-S., and Kim, S.-J., 2010, “Surface Modification and Characterization of Highly Dispersed Silica Nanoparticles by a Cationic Surfactant,” Colloids Surf. Physicochem. Eng. Asp., **358**(1), pp. 172–176.

[115] Chang, S.-J., Liao, W.-S., Ciou, C.-J., Lee, J.-T., and Li, C.-C., 2009, “An Efficient Approach to Derive Hydroxyl Groups on the Surface of Barium Titanate Nanoparticles to Improve Its Chemical Modification Ability,” J. Colloid Interface Sci., **329**(2), pp. 300–305.

[116] Du, Y., Yin, Z., Zhu, J., Huang, X., Wu, X.-J., Zeng, Z., Yan, Q., and Zhang, H., 2012, “A General Method for the Large-Scale Synthesis of Uniform Ultrathin Metal Sulphide Nanocrystals,” Nat. Commun., **3**, p. 1177.

[117] Bruce, I. J., and Sen, T., 2005, “Surface Modification of Magnetic Nanoparticles with Alkoxysilanes and Their Application in Magnetic Bioseparations,” Langmuir, **21**(15), pp. 7029–7035.

[118] Vandenberg, E. T., Bertilsson, L., Liedberg, B., Uvdal, K., Erlandsson, R., Elwing, H., and Lundström, I., 1991, “Structure of 3-Aminopropyl Triethoxy Silane on Silicon Oxide,” J. Colloid Interface Sci., **147**(1), pp. 103–118.

[119] White, L. D., and Tripp, C. P., 2000, “Reaction of (3-Aminopropyl)Dimethylethoxysilane with Amine Catalysts on Silica Surfaces,” J. Colloid Interface Sci., **232**(2), pp. 400–407.

[120] Ge, J., He, L., Goebl, J., and Yin, Y., 2009, “Assembly of Magnetically Tunable Photonic Crystals in Nonpolar Solvents,” J. Am. Chem. Soc., **131**(10), pp. 3484–3486.

[121] Yu, B., Qian, L., Yu, J., and Zhou, Z., 2009, “Effects of Tail Group and Chain Length on the Tribological Behaviors of Self-Assembled Dual-Layer Films in Atmosphere and in Vacuum,” Tribol. Lett., **34**(1), p. 1.

[122] Iijima, M., Tsukada, M., and Kamiya, H., 2007, “Effect of Particle Size on Surface Modification of Silica Nanoparticles by Using Silane Coupling Agents and Their Dispersion Stability in Methylethylketone,” J. Colloid Interface Sci., **307**(2), pp. 418–424.

[123] Pham, K. N., Fullston, D., and Sagoe-Crentsil, K., 2007, “Surface Charge Modification of Nano-Sized Silica Colloid,” Aust. J. Chem., **60**(9), pp. 662–666.

[124] Zeltner, M., N. Grass, R., Schaetz, A., B. Bubenhofer, S., A. Luechinger, N., and J. Stark, W., 2012, “Stable Dispersions of Ferromagnetic Carbon-Coated Metal Nanoparticles : Preparation via Surface Initiated Atom Transfer Radical Polymerization,” J. Mater. Chem., **22**(24), pp. 12064–12071.

[125] Zhao, B., and Zhu, L., 2009, “Mixed Polymer Brush-Grafted Particles: A New Class of Environmentally Responsive Nanostructured Materials,” Macromolecules, **42**(24), pp. 9369–9383.

[126] Rodriguez, R., Herrera, R., Archer, L. A., and Giannelis, E. P., 2008, “Nanoscale Ionic Materials,” Adv. Mater., **20**(22), pp. 4353–4358.

[127] Wilson, W. R. D., 1997, “Tribology in Cold Metal Forming,” J. Manuf. Sci. Eng., **119**(4B), pp. 695–698.

[128] Kawai, N., and Dohda, K., 1987, “A New Lubricity Evaluation Method for Metal Forming by a Compression-Twist Type Friction Testing Machine,” J. Tribol., **109**(2), pp. 343–350.

[129] Radil, K. C., and Dellacorte, C., 2002, “The Effect of Journal Roughness and Foil Coatings on the Performance of Heavily Loaded Foil Air Bearings,” Tribol. Trans., **45**(2), pp. 199–204.

[130] Bailey, E. I., and Smith, J. E., 1993, “Testing Thread Compounds for Rotary-Shouldered Connections,” SPE Drill. Complet., **8**(03), pp. 170–174.

[131] Bhansali, K. J., and Miller, A. E., 1982, “The Role of Stacking Fault Energy on Galling and Wear Behavior,” Wear, **75**(2), pp. 241–252.

[132] Cocks, M., 1965, “The Formation of Wedges of Displaced Metal between Sliding Metal Surfaces,” Wear, **8**(2), pp. 85–92.

[133] Hummel, S. R., 2008, “Development of a Galling Resistance Test Method with a Uniform Stress Distribution,” Tribol. Int., **41**(3), pp. 175–180.

[134] Lugt, P. M., 2016, “Modern Advancements in Lubricating Grease Technology,” Tribol. Int., **97**, pp. 467–477.

[135] Bauer, W. H., Finkelstein, A. P., and Wiberley, S. E., 1960, “Flow Properties of Lithium Stearate-Oil Model Greases as Functions of Soap Concentration and Temperature,” E Trans., **3**(2), pp. 215–224.

[136] Lugt, P. M., 2009, “A Review on Grease Lubrication in Rolling Bearings,” Tribol. Trans., **52**(4), pp. 470–480.

[137] Hong, H., Waynick, A. J., and Roy, W., 2008, “Nanogrease Based on Carbon Nanotube,” NLGI Spokesm., **72**(7), pp. 9–17.

[138] Spikes, H., 2015, “Friction Modifier Additives,” Tribol. Lett., **60**(1), p. 5.

[139] Carper, H. J., Ertas, A., and Cuvalci, O., 1995, “Rating Thread Compounds for Galling Resistance,” J. Tribol., **117**(4), pp. 639–645.

[140] Colmery, B. H., 1998, “Composite Restorative Dentistry,” Vet. Clin. Small Anim. Pract., **28**(5), pp. 1261–1271.

[141] Greenfield, B. A., 2012, “Enamel Defect Restoration of the Left Mandibular First Molar Tooth,” J. Vet. Dent., **29**(1), pp. 36–43.

[142] He, L. H., and Swain, M. V., 2007, “Enamel—A ‘Metallic-like’ Deformable Biocomposite,” J. Dent., **35**(5), pp. 431–437.

[143] Bajaj, D., and Arola, D. D., 2009, “On the R-Curve Behavior of Human Tooth Enamel,” Biomaterials, **30**(23), pp. 4037–4046.

[144] Lee, J. J.-W., Constantino, P. J., Lucas, P. W., and Lawn, B. R., 2011, “Fracture in Teeth—a Diagnostic for Inferring Bite Force and Tooth Function,” Biol. Rev., **86**(4), pp. 959–974.

[145] Roy, S., and Basu, B., 2008, “Mechanical and Tribological Characterization of Human Tooth,” Mater. Charact., **59**(6), pp. 747–756.

[146] Addy, M., and Shellis, R. P., 2006, “Interaction between Attrition,Abrasion and Erosion in Tooth Wear,” Dent. Eros., **20**, pp. 17–31.

[147] Bajaj, D., Nazari, A., Eidelman, N., and Arola, D. D., 2008, “A Comparison of Fatigue Crack Growth in Human Enamel and Hydroxyapatite,” Biomaterials, **29**(36), pp. 4847–4854.

[148] He, L. H., and Swain, M. V., 2007, "Contact Induced Deformation of Enamel," Appl. Phys. Lett., **90**(17), p. 171916.

[149] Rios, D., Honório, H. M., Magalhães, A. C., Buzalaf, M. A. R., Palma-Dibb, R. G., Machado, M. A. de A. M., and Silva, S. M. B. da, 2006, "Influence of Toothbrushing on Enamel Softening and Abrasive Wear of Eroded Bovine Enamel: An in Situ Study," Braz. Oral Res., **20**(2), pp. 148–154.

[150] Lewis, R., and Dwyer-Joyce, R. S., 2005, "Wear of Human Teeth: A Tribological Perspective," Proc. Inst. Mech. Eng. Part J J. Eng. Tribol., **219**(1), pp. 1–18.

[151] Levitch, L. C., Bader, J. D., Shugars, D. A., and Heymann, H. O., 1994, "Non-Carious Cervical Lesions," J. Dent., **22**(4), pp. 195–207.

[152] Buzalaf, M. A. R., Hannas, A. R., and Kato, M. T., 2012, "Saliva and Dental Erosion," J. Appl. Oral Sci., **20**(5), pp. 493–502.

[153] West, N. X., and Joiner, A., 2014, "Enamel Mineral Loss," J. Dent., **42**, pp. S2–S11.

[154] Cheng, R., Yang, H., Shao, M., Hu, T., and Zhou, X., 2009, "Dental Erosion and Severe Tooth Decay Related to Soft Drinks: A Case Report and Literature Review," J. Zhejiang Univ. Sci. B, **10**(5), pp. 395–399.

[155] Palamara, D., Palamara, J. E. A., Tyas, M. J., Pintado, M., and Messer, H. H., 2001, "Effect of Stress on Acid Dissolution of Enamel," Dent. Mater., **17**(2), pp. 109–115.

[156] Holmstrom, S. E., Fitch, P. F., and Eisner, E. R., 2004, *Veterinary Dental Techniques for the Small Animal Practitioner*, Elsevier Health Sciences.

[157] Majewski, R. F., Snyder, C. W., and Bernat, J. E., 1988, "Dental Emergencies Presenting to a Children's Hospital.," ASDC J. Dent. Child., **55**(5), pp. 339–342.

[158] Monse, B., Heinrich-Weltzien, R., Benzian, H., Holmgren, C., and Helderman, W. V. P., 2010, "PUFA – An Index of Clinical Consequences of Untreated Dental Caries," Community Dent. Oral Epidemiol., **38**(1), pp. 77–82.

[159] Nunn, J. H., 1996, "Prevalence of Dental Erosion and the Implications for Oral Health," Eur. J. Oral Sci., **104**(2), pp. 156–161.

[160] Lacruz, R. S., Habelitz, S., Wright, J. T., and Paine, M. L., 2017, "Dental Enamel Formation and Implications for Oral Health and Disease," Physiol. Rev., **97**(3), pp. 939–993.

[161] Cochrane, N. J., Cai, F., Huq, N. L., Burrow, M. F., and Reynolds, E. C., 2010, "New Approaches to Enhanced Remineralization of Tooth Enamel," J. Dent. Res., **89**(11), pp. 1187–1197.

[162] Zhou, Y.-Z., Cao, Y., Liu, W., Chu, C. H., and Li, Q.-L., 2012, "Polydopamine-Induced Tooth Remineralization," ACS Appl. Mater. Interfaces, **4**(12), pp. 6901–6910.

[163] Walker, G., Cai, F., Shen, P., Reynolds, C., Ward, B., Fone, C., Honda, S., Koganei, M., Oda, M., and Reynolds, E., 2006, "Increased Remineralization of Tooth Enamel by Milk Containing Added Casein Phosphopeptide-Amorphous Calcium Phosphate," J. Dairy Res., **73**(1), pp. 74–78.

[164] Arends, J., and Ten Cate, J. M., 1981, "Tooth Enamel Remineralization," J. Cryst. Growth, **53**(1), pp. 135–147.

[165] Hicks, J., Garcia-Godoy, F., and Flaitz, C., 2004, "Biological Factors in Dental Caries: Role of Saliva and Dental Plaque in the Dynamic Process of

Demineralization and Remineralization (Part 1)," J. Clin. Pediatr. Dent., **28**(1), pp. 47–52.

[166] Cölfen, H., 2010, "A Crystal-Clear View," Nat. Mater., **9**(12), pp. 960–961.

[167] Oshiro, M., Yamaguchi, K., Takamizawa, T., Inage, H., Watanabe, T., Irokawa, A., Ando, S., and Miyazaki, M., 2007, "Effect of CPP-ACP Paste on Tooth Mineralization: An FE-SEM Study," J. Oral Sci., **49**(2), pp. 115–120.

[168] Sitthisettapong, T., Phantumvanit, P., Huebner, C., and DeRouen, T., 2012, "Effect of CPP-ACP Paste on Dental Caries in Primary Teeth: A Randomized Trial," J. Dent. Res., **91**(9), pp. 847–852.

[169] Jayarajan, J., Janardhanam, P., Jayakumar, P., and Deepika, 2011, "Efficacy of CPP-ACP and CPP-ACPF on Enamel Remineralization - An in Vitro Study Using Scanning Electron Microscope and DIAGNOdent®," Indian J. Dent. Res., **22**(1), p. 77.

[170] Fan, Y., Sun, Z., and Moradian-Oldak, J., 2009, "Controlled Remineralization of Enamel in the Presence of Amelogenin and Fluoride," Biomaterials, **30**(4), pp. 478–483.

[171] Kapadia, R., Glyde, R., and Wu, Y., 2007, "In Situ Observation of Phosphorous and Non-Phosphorous Antiwear Films Using a Mini Traction Machine with Spacer Layer Image Mapping," Tribol. Int., **40**(10–12), pp. 1667–1679.

[172] Xu, Y., Wang, Q., Hu, X., Li, C., and Zhu, X., 2010, "Characterization of the Lubricity of Bio-Oil/Diesel Fuel Blends by High Frequency Reciprocating Test Rig," Energy, **35**(1), pp. 283–287.

[173] Tonck, A., Martin, J. M., Kapsa, Ph., and Georges, J. M., 1979, "Boundary Lubrication with Anti-Wear Additives: Study of Interface Film Formation by Electrical Contact Resistance," Tribol. Int., **12**(5), pp. 209–213.

[174] Rosenkranz, A., Martin, B., Bettscheider, S., Gachot, C., Kliem, H., and Mücklich, F., 2014, "Correlation between Solid–Solid Contact Ratios and Lubrication Regimes Measured by a Refined Electrical Resistivity Circuit," Wear, **320**(Supplement C), pp. 51–61.

[175] Myshkin, N. K., and Konchits, V. V., 1994, "Evaluation of the Interface at Boundary Lubrication Using the Measurement of Electric Conductivity," Wear, **172**(1), pp. 29–40.

[176] Clarke, A., Weeks, I. J. J., Evans, H. P., and Snidle, R. W., 2016, "An Investigation into Mixed Lubrication Conditions Using Electrical Contact Resistance Techniques," Tribol. Int., **93**, pp. 709–716.

[177] Jablonka, K., Glovnea, R., and Bongaerts, J., 2012, "Evaluation of EHD Films by Electrical Capacitance," J. Phys. Appl. Phys., **45**(38), p. 385301.

[178] Furtmann, A., and Poll, G., 2016, "Evaluation of Oil-Film Thickness along the Path of Contact in a Gear Mesh by Capacitance Measurement," Tribol. Online, **11**(2), pp. 189–194.

[179] Jablonka, K., Glovnea, R., Bongaerts, J., and Morales-Espejel, G., 2013, "The Effect of the Polarity of the Lubricant upon Capacitance Measurements of EHD Contacts," Tribol. Int., **61**, pp. 95–101.

[180] Schnabel, S., Marklund, P., Minami, I., and Larsson, R., 2016, "Monitoring of Running-in of an EHL Contact Using Contact Impedance," Tribol. Lett., **63**(3), p. 35.

[181] Hadden, T., Jiang, J. W., Bilgin, B., Yinye Yang, Sathyan, A., Dadkhah, H., and Emadi, A., 2016, "A Review of Shaft Voltages and Bearing Currents in EV and HEV Motors," *IECON 2016 - 42nd Annual Conference of the IEEE Industrial Electronics Society*, pp. 1578–1583.

[182] Håkansson, B., Andersson, P., and Bäckström, G., 1988, "Improved Hot-wire Procedure for Thermophysical Measurements under Pressure," Rev. Sci. Instrum., **59**(10), pp. 2269–2275.

[183] Shibata, H., Suzuki, A., and Ohta, H., 2005, "Measurement of Thermal Transport Properties for Molten Silicate Glasses at High Temperatures by Means of a Novel Laser Flash Technique," Mater. Trans., **46**(8), pp. 1877–1881.

[184] Chen, Y., Yue, Y., Rasoulzadeh, M., and Liang, H., 2019, "Nanofluidic Behavior at the Fluid-Solid Interface," Mater. Perform. Charact., **8**(1), pp. 538–550.

[185] Bocquet, L., and Charlaix, E., 2010, "Nanofluidics, from Bulk to Interfaces," Chem. Soc. Rev., **39**(3), pp. 1073–1095.

[186] Murata, K., Mitsuoka, K., Hirai, T., Walz, T., and al, et, 2000, "Structural Determinants of Water Permeation through Aquaporin-1," Nat. Lond., **407**(6804), pp. 599–605.

[187] Sui, H., Han, B.-G., Lee, J. K., Walian, P., and Jap, B. K., 2001, "Structural Basis of Water-Specific Transport through the AQP1 Water Channel," Nature, **414**(6866), pp. 872–878.

[188] Wu, C. W., and Ma, G. J., 2005, "Abnormal Behavior of a Hydrodynamic Lubrication Journal Bearing Caused by Wall Slip," Tribol. Int., **38**(5), pp. 492–499.

[189] Thompson, P. A., and Troian, S. M., 1997, "A General Boundary Condition for Liquid Flow at Solid Surfaces," Nat. Lond., **389**(6649), pp. 360–362.

[190] Neto, C., Evans, D. R., Bonaccurso, E., Butt, H.-J., and Craig, V. S. J., 2005, "Boundary Slip in Newtonian Liquids: A Review of Experimental Studies," Rep. Prog. Phys., **68**(12), p. 2859.

[191] Bocquet, L., and Barrat, J.-L., 2007, "Flow Boundary Conditions from Nano- to Micro-Scales," Soft Matter, **3**(6), pp. 685–693.

[192] Cottin-Bizonne, C., Cross, B., Steinberger, A., and Charlaix, E., 2005, "Boundary Slip on Smooth Hydrophobic Surfaces: Intrinsic Effects and Possible Artifacts," Phys. Rev. Lett., **94**(5), p. 056102.

[193] Restagno, F., Crassous, J., Charlaix, É., Cottin-Bizonne, C., and Monchanin, M., 2002, "A New Surface Forces Apparatus for Nanorheology," Rev. Sci. Instrum., **73**(6), pp. 2292–2297.

[194] Klein, J., and Kumacheva, E., 1998, "Simple Liquids Confined to Molecularly Thin Layers. I. Confinement-Induced Liquid-to-Solid Phase Transitions," J. Chem. Phys., **108**(16), pp. 6996–7009.

[195] Raviv, U., Giasson, S., Frey, J., and Klein, J., 2002, "Viscosity of Ultra-Thin Water Films Confined between Hydrophobic or Hydrophilic Surfaces," J. Phys. Condens. Matter, **14**(40), p. 9275.

[196] Pit, R., Hervet, H., and Léger, L., 2000, "Direct Experimental Evidence of Slip in Hexadecane: Solid Interfaces," Phys. Rev. Lett., **85**(5), pp. 980–983.
[197] Landau, L. D., and Lifshitz, E. M., 2013, *Fluid Mechanics*, Elsevier.
[198] Wang, C. Y., 1991, "Exact Solutions of the Steady-State Navier-Stokes Equations," Annu. Rev. Fluid Mech., **23**, pp. 159–177.
[199] Macosko, C. W., 1994, *Rheology: Principles, Measurements, and Applications*, VCH.
[200] Shaw, D. J., 1992, *Introduction to Colloid and Surface Chemistry*, Butterworth-Heinemann, Oxford ; Boston.
[201] Russel, W. B., Russel, W. B., Saville, D. A., and Schowalter, W. R., 1991, *Colloidal Dispersions*, Cambridge university press.
[202] Napper, D. H., 1977, "Steric Stabilization," J. Colloid Interface Sci., **58**(2), pp. 390–407.
[203] Smitham, J. B., and Napper, D. H., 1979, "Steric Stabilization in Worse Than<Emphasis Type="Italic">θ</Emphasis>-Solvents," Colloid Polym. Sci., **257**(7), pp. 748–756.
[204] Zhulina, E. B., Borisov, O. V., and Priamitsyn, V. A., 1990, "Theory of Steric Stabilization of Colloid Dispersions by Grafted Polymers," J. Colloid Interface Sci., **137**(2), pp. 495–511.
[205] Van Der Hoeven, Ph. C., and Lyklema, J., 1992, "Electrostatic Stabilization in Non-Aqueous Media," Adv. Colloid Interface Sci., **42**, pp. 205–277.
[206] Briscoe, W. H., and Horn, R. G., 2002, "Direct Measurement of Surface Forces Due to Charging of Solids Immersed in a Nonpolar Liquid," Langmuir, **18**(10), pp. 3945–3956.
[207] Carey, A. A., "The Dielectric Constant of Lubrication Oils," p. 9.
[208] Gerber, P., and Moore, M. A., 1977, "Comments on the Theory of Steric Stabilization," Macromolecules, **10**(2), pp. 476–481.
[209] Hamaker, H. C., 1937, "The London—van Der Waals Attraction between Spherical Particles," Physica, **4**(10), pp. 1058–1072.
[210] Bergstr, L., 1997, "Hamaker Constants of Inorganic Materials," Adv Colloid Interface Sci, p. 45.
[211] Srivastava, S. N., and Haydon, D. A., 1964, "Estimate of the Hamaker Constant for Paraffinic Hydrocarbons in Aqueous Suspensions," Trans. Faraday Soc., **60**, p. 971.
[212] Vial, J., and Carré, A., 1991, "Calculation of Hamaker Constant and Surface Energy of Polymers by a Simple Group Contribution Method," Int. J. Adhes. Adhes., **11**(3), pp. 140–143.
[213] Croucher, M. D., and Hair, M. L., 1977, "Hamaker Constants and the Principle of Corresponding States," J. Phys. Chem., **81**(17), pp. 1631–1636.
[214] Visser, J., 1972, "On Hamaker Constants: A Comparison between Hamaker Constants and Lifshitz-van Der Waals Constants," Adv. Colloid Interface Sci., **3**(4), pp. 331–363.
[215]Pinchuk, A. O., 2012, "Size-Dependent Hamaker Constant for Silver Nanoparticles," J. Phys. Chem. C, **116**(37), pp. 20099–20102.

[216] Jiang, K., and Pinchuk, P., 2016, “Temperature and Size-Dependent Hamaker Constants for Metal Nanoparticles,” Nanotechnology, **27**(34), p. 345710.

[217] Yang, K., Peng, H., Wen, Y., and Li, N., 2010, “Re-Examination of Characteristic FTIR Spectrum of Secondary Layer in Bilayer Oleic Acid-Coated Fe3O4 Nanoparticles,” Appl. Surf. Sci., **256**(10), pp. 3093–3097.

[218] Kataby, G., Cojocaru, M., Prozorov, R., and Gedanken, A., 1999, “Coating Carboxylic Acids on Amorphous Iron Nanoparticles,” Langmuir, **15**(5), pp. 1703–1708.

[219] Gun’ko, V. M., Voronin, E. F., Pakhlov, E. M., Zarko, V. I., Turov, V. V., Guzenko, N. V., Leboda, R., and Chibowski, E., 2000, “Features of Fumed Silica Coverage with Silanes Having Three or Two Groups Reacting with the Surface,” Colloids Surf. Physicochem. Eng. Asp., **166**(1), pp. 187–201.

[220] Ishida, H., and Koenig, J. L., 1978, “Fourier Transform Infrared Spectroscopic Study of the Structure of Silane Coupling Agent on E-Glass Fiber,” J. Colloid Interface Sci., **64**(3), pp. 565–576.

[221] Murat, M., and Grest, G. S., 1989, “Structure of a Grafted Polymer Brush: A Molecular Dynamics Simulation,” Macromolecules, **22**(10), pp. 4054–4059.

[222] Holmberg, K., and Erdemir, A., 2019, “The Impact of Tribology on Energy Use and CO2 Emission Globally and in Combustion Engine and Electric Cars,” Tribol. Int., **135**, pp. 389–396.

[223] Walther, H. C., and Holub, R. A., 2014, “Lubrication of Electric Motors as Defined by IEEE Standard 841-2009, Shortcomings and Potential Improvement Opportunities,” *2014 IEEE Petroleum and Chemical Industry Technical Conference (PCIC)*, IEEE, pp. 91–98.

[224] Chen, S., Lipo, T. A., and Fitzgerald, D., 1996, “Modeling of Motor Bearing Currents in PWM Inverter Drives,” IEEE Trans. Ind. Appl., **32**(6), pp. 1365–1370.

[225] Whittle, M., Trevelyan, J., and Tavner, P. J., 2013, “Bearing Currents in Wind Turbine Generators,” J. Renew. Sustain. Energy, **5**(5), p. 053128.

[226] Akagi, H., and Doumoto, T., 2004, “An Approach to Eliminating High-Frequency Shaft Voltage and Ground Leakage Current from an Inverter-Driven Motor,” IEEE Trans. Ind. Appl., **40**(4), pp. 1162–1169.

[227] Chen, S., and Lipo, T. A., 1998, “Bearing Currents and Shaft Voltages of an Induction Motor under Hard-and Soft-Switching Inverter Excitation,” IEEE Trans. Ind. Appl., **34**(5), pp. 1042–1048.

[228] Fan, F., See, K. Y., Banda, J. K., Liu, X., and Gupta, A. K., 2019, “Investigation and Mitigation of Premature Bearing Degradation in Motor Drive System,” IEEE Electromagn. Compat. Mag., **8**(1), pp. 75–81.

[229] Hamrock, B. J., and Dowson, D., 1977, “Isothermal Elastohydrodynamic Lubrication of Point Contacts: Part III—Fully Flooded Results,” J. Lubr. Technol., **99**(2), pp. 264–275.

[230] Okrent, E. H., 1961, “The Effect of Lubricant Viscosity and Composition on Engine Friction and Bearing Wear,” ASLE Trans., **4**(1), pp. 97–108.

[231] Evans, C. R., and Johnson, K. L., 1986, “The Rheological Properties of Elastohydrodynamic Lubricants,” Proc. Inst. Mech. Eng. Part C J. Mech. Eng. Sci., **200**(5), pp. 303–312.

[232] Johnston, G. J., Wayte, R., and Spikes, H. A., 1991, “The Measurement and Study of Very Thin Lubricant Films in Concentrated Contacts,” Tribol. Trans., **34**(2), pp. 187–194.

[233] Cann, P. M., and Spikes, H. A., 1989, “Determination of the Shear Stresses of Lubricants in Elastohydrodynamic Contacts,” Tribol. Trans., **32**(3), pp. 414–422.

[234] Masjedi, M., and Khonsari, M. M., 2014, “Theoretical and Experimental Investigation of Traction Coefficient in Line-Contact EHL of Rough Surfaces,” Tribol. Int., **70**, pp. 179–189.

[235] Gao, F., and Liang, H., 2012, “Effects of Potential and Mechanical Stimulation on Oxidation of Tantalum during Electrochemical Mechanical Polishing,” J. Electron. Mater., **41**(3), pp. 624–631.

[236] Huitink, D., Gao, F., Wang, K., and Liang, H., 2010, “In Situ Monitoring of Tantalum during Electrochemical-Mechanically Induced Oxidation,” Electrochem. Solid-State Lett., **13**(9), pp. F16–F19.

[237] Kar, P., Wang, K., and Liang, H., 2008, “Force-Dominated Non-Equilibrium Oxidation Kinetics of Tantalum,” Electrochimica Acta, **53**(16), pp. 5084–5091.

[238] Stribeck, R., 1902, “The Key Qualities of Sliding and Roller Bearings,” Z. Vereines Seutscher Ingenieure, **46**(38), pp. 1342–1348.

[239] Komvopoulos, K., Saka, N., and Suh, N. P., 1985, “The Mechanism of Friction in Boundary Lubrication,” J. Tribol., **107**(4), pp. 452–462.

[240] Kogut, L., and Komvopoulos, K., 2003, “Electrical Contact Resistance Theory for Conductive Rough Surfaces,” J. Appl. Phys., **94**(5), pp. 3153–3162.

[241] Kogut, L., and Komvopoulos, K., 2003, “Electrical Contact Resistance Theory for Conductive Rough Surfaces Separated by a Thin Insulating Film,” J. Appl. Phys., **95**(2), pp. 576–585.

[242] Chen, Y., Jha, S., Raut, A., Zhang, W., and Liang, H., 2020, “Performance Characteristics of Lubricants in Electric and Hybrid Vehicles: A Review of Current and Future Needs,” Front. Mech. Eng., **6**.

[243] Woods, L. C., 1975, *The Thermodynamics of Fluid Systems*.

[244] Yang, Y., Bilgin, B., Kasprzak, M., Nalakath, S., Sadek, H., Preindl, M., Cotton, J., Schofield, N., and Emadi, A., 2016, “Thermal Management of Electric Machines,” IET Electr. Syst. Transp., **7**(2), pp. 104–116.

[245] Hasebe, M., Miyaishi, Y., Wakuta, S., Minezawa, Y., Hara, T., and Tsuzuki, S., 1994, *Oil Circulating System for Electric Vehicle*, Google Patents.

[246] Stockton, T. R., 1983, *Transmission Lubrication and Motor Cooling System*, Google Patents.

[247] Pettersson, A., 2007, “High-Performance Base Fluids for Environmentally Adapted Lubricants,” Tribol. Int., **40**(4), pp. 638–645.

[248] Boncompain, R., Fillon, M., and Frene, J., 1986, “Analysis of Thermal Effects in Hydrodynamic Bearings,” J. Tribol., **108**(2), pp. 219–224.

[249] Hamrock, B. J., and Dowson, D., 1976, “Isothermal Elastohydrodynamic Lubrication of Point Contacts: Part 1—Theoretical Formulation,” J. Lubr. Technol., **98**(2), pp. 223–228.

[250] Larsson, R., and Andersson, O., 2000, “Lubricant Thermal Conductivity and Heat Capacity under High Pressure,” Proc. Inst. Mech. Eng. Part J J. Eng. Tribol., **214**(4), pp. 337–342.

[251] Nagasaka, Y., and Nagashima, A., 1981, “Simultaneous Measurement of the Thermal Conductivity and the Thermal Diffusivity of Liquids by the Transient Hot-wire Method,” Rev. Sci. Instrum., **52**(2), pp. 229–232.

[252] Vozár, L., and Hohenauer, W., 2004, “Flash Method of Measuring the Thermal Diffusivity. A Review,” High Temp.-High Press., **36**(3), pp. 253–264.

[253] Greenwood, J. A., 1966, “Constriction Resistance and the Real Area of Contact,” Br. J. Appl. Phys., **17**(12), pp. 1621–1632.

[254] Chen, Y., and Liang, H., 2019, “Tribological Evaluation of Electrical Resistance of Lubricated Contacts,” J. Tribol., pp. 1–9.

[255] Guyer, J. E., Wheeler, D., and Warren, J. A., 2009, “FiPy: Partial Differential Equations with Python,” Comput. Sci. Eng., **11**(3), pp. 6–15.

[256] Gedde, U. L. F., 1995, *Polymer Physics*, Springer Science & Business Media.

[257] Larsson, R., Larsson, P. O., Eriksson, E., Sjöberg, M., and Höglund, E., 2000, “Lubricant Properties for Input to Hydrodynamic and Elastohydrodynamic Lubrication Analyses,” Proc. Inst. Mech. Eng. Part J J. Eng. Tribol., **214**(1), pp. 17–27.

[258] Sharp, M. K., 1993, “Shear-Augmented Dispersion in Non-Newtonian Fluids,” Ann. Biomed. Eng., **21**(4), pp. 407–415.

[259] Kumar, A., and Mishra, S. S., 1996, “Stability of a Rigid Rotor in Turbulent Hydrodynamic Worn Journal Bearings,” Wear, **193**(1), pp. 25–30.

[260] Muley, A., and Manglik, R. M., 1999, “Experimental Study of Turbulent Flow Heat Transfer and Pressure Drop in a Plate Heat Exchanger With Chevron Plates,” J. Heat Transf., **121**(1), pp. 110–117.

[261] Tsubouchi, T., and Shinoda, J., 2010, “Characterization of Oily High Bulk Modulus Fluid,” Tribol. Online, **5**(5), pp. 230–234.

[262] Bird, R. B., 2002, “Transport Phenomena,” Appl Mech Rev, **55**(1), pp. R1–R4.

[263] Spikes, H., 2004, “The History and Mechanisms of ZDDP,” Tribol. Lett., **17**(3), pp. 469–489.

[264] Fein, R. S., and Kreuz, K. L., 1965, “Chemistry of Boundary Lubrication of Steel by Hydrocarbons,” ASLE Trans., **8**(1), pp. 29–38.

[265] Li, J., Zhang, C., and Luo, J., 2013, “Superlubricity Achieved with Mixtures of Polyhydroxy Alcohols and Acids,” Langmuir, **29**(17), pp. 5239–5245.

[266] Ge, X., Li, J., Zhang, C., and Luo, J., 2018, “Liquid Superlubricity of Polyethylene Glycol Aqueous Solution Achieved with Boric Acid Additive,” Langmuir, **34**(12), pp. 3578–3587.

[267] Nygaard, E. M., and Oberright, E. A., 1963, *Lubricating Oil Containing Zinc Carboxylate-Coordinated Zinc Dithiophosphates*, Google Patents.

[268] Taylor, L., Dratva, A., and Spikes, H. A., 2000, "Friction and Wear Behavior of Zinc Dialkyldithiophosphate Additive," Tribol. Trans., **43**(3), pp. 469–479.

[269] Yamamoto, Y., and Gondo, S., 1989, "Friction and Wear Characteristics of Molybdenum Dithiocarbamate and Molybdenum Dithiophosphate," Tribol. Trans., **32**(2), pp. 251–257.

[270] Wu, Y., He, Z., Zeng, X., Ren, T., de Vries, E., and van der Heide, E., 2017, "Tribological Properties and Tribochemistry Mechanism of Sulfur-Containing Triazine Derivatives in Water-Glycol," Tribol. Int., **109**, pp. 140–151.

[271] Callen, H. B., 1985, "Thermodynamics and an Introduction to Thermostatistics," tait, p. 512.

[272] Mosey, N. J., and Woo, T. K., 2004, "A Quantum Chemical Study of the Unimolecular Decomposition Mechanisms of Zinc Dialkyldithiophosphate Antiwear Additives," J. Phys. Chem. A, **108**(28), pp. 6001–6016.

[273] Yue, D.-C., Ma, T.-B., Hu, Y.-Z., Yeon, J., van Duin, A. C. T., Wang, H., and Luo, J., 2013, "Tribochemistry of Phosphoric Acid Sheared between Quartz Surfaces: A Reactive Molecular Dynamics Study," J. Phys. Chem. C, **117**(48), pp. 25604–25614.

[274] Sherwood, B. A., and Bernard, W. H., 1984, "Work and Heat Transfer in the Presence of Sliding Friction," Am. J. Phys., **52**(11), pp. 1001–1007.

[275] Kennedy, F. E., 1984, "Thermal and Thermomechanical Effects in Dry Sliding," Wear, **100**(1), pp. 453–476.

[276] Liu, G., and Wang, Q., 2000, "Thermoelastic Asperity Contacts, Frictional Shear, and Parameter Correlations," J. Tribol., **122**(1), pp. 300–307.

[277] Khonsari, M. M., and Hua, D. Y., 1994, "Thermal Elastohydrodynamic Analysis Using a Generalized Non-Newtonian Formulation With Application to Bair-Winer Constitutive Equation," J. Tribol., **116**(1), pp. 37–46.

[278] Bresme, F., Lervik, A., Bedeaux, D., and Kjelstrup, S., 2008, "Water Polarization under Thermal Gradients," Phys. Rev. Lett., **101**(2), p. 020602.

[279] Jou, D., Casas-Vázquez, J., and Criado-Sancho, M., 2010, *Thermodynamics of Fluids under Flow*, Springer Science & Business Media.

[280] Nakayama, K., and Hashimoto, H., 1991, "Triboemission from Various Materials in Atmosphere," Wear, **147**(2), pp. 335–343.

[281] Kajdas, C. K., 2005, "Importance of the Triboemission Process for Tribochemical Reaction," Tribol. Int., **38**(3), pp. 337–353.

[282] Kajdas, C., Kulczycki, A., and Ozimina, D., 2017, "A New Concept of the Mechanism of Tribocatalytic Reactions Induced by Mechanical Forces," Tribol. Int., **107**, pp. 144–151.

[283] Nakayama, K., and Hashimoto, H., 1996, "Triboemission, Tribochemical Reaction, and Friction and Wear in Ceramics under Various n-Butane Gas Pressures," Tribol. Int., **29**(5), pp. 385–393.

[284] Wiita, A. P., Ainavarapu, S. R. K., Huang, H. H., and Fernandez, J. M., 2006, "Force-Dependent Chemical Kinetics of Disulfide Bond Reduction Observed with Single-Molecule Techniques," Proc. Natl. Acad. Sci., **103**(19), pp. 7222–7227.

[285] Adams, H. L., Garvey, M. T., Ramasamy, U. S., Ye, Z., Martini, A., and Tysoe, W. T., 2015, "Shear-Induced Mechanochemistry: Pushing Molecules Around," J. Phys. Chem. C, **119**(13), pp. 7115–7123.

[286] Liang, J., and Fernández, J. M., 2011, "Kinetic Measurements on Single-Molecule Disulfide Bond Cleavage," J. Am. Chem. Soc., **133**(10), pp. 3528–3534.

[287] Yeon, J., He, X., Martini, A., and Kim, S. H., 2017, "Mechanochemistry at Solid Surfaces: Polymerization of Adsorbed Molecules by Mechanical Shear at Tribological Interfaces," ACS Appl. Mater. Interfaces, **9**(3), pp. 3142–3148.

[288] Khajeh, A., He, X., Yeon, J., Kim, S. H., and Martini, A., 2018, "Mechanochemical Association Reaction of Interfacial Molecules Driven by Shear," Langmuir, **34**(21), pp. 5971–5977.

[289] Akchurin, A., and Bosman, R., 2017, "A Deterministic Stress-Activated Model for Tribo-Film Growth and Wear Simulation," Tribol. Lett., **65**(2), p. 59.

[290] Zhang, J., and Spikes, H., 2016, "On the Mechanism of ZDDP Antiwear Film Formation," Tribol. Lett., **63**(2), p. 24.

[291] Gosvami, N. N., Bares, J. A., Mangolini, F., Konicek, A. R., Yablon, D. G., and Carpick, R. W., 2015, "Mechanisms of Antiwear Tribofilm Growth Revealed in Situ by Single-Asperity Sliding Contacts," Science, **348**(6230), pp. 102–106.

[292] Dorgham, A., Azam, A., Morina, A., and Neville, A., 2018, "On the Transient Decomposition and Reaction Kinetics of Zinc Dialkyldithiophosphate," ACS Appl. Mater. Interfaces, **10**(51), pp. 44803–44814.

[293] Dorgham, A., Parsaeian, P., Azam, A., Wang, C., Morina, A., and Neville, A., 2019, "Single-Asperity Study of the Reaction Kinetics of P-Based Triboreactive Films," Tribol. Int., **133**, pp. 288–296.

[294] Chen, Y., Renner, P., and Liang, H., 2019, "Dispersion of Nanoparticles in Lubricating Oil: A Critical Review," Lubricants, **7**(1), p. 7.

[295] Ratoi, M., Niste, V. B., Walker, J., and Zekonyte, J., 2013, "Mechanism of Action of WS2 Lubricant Nanoadditives in High-Pressure Contacts," Tribol. Lett., **52**(1), pp. 81–91.

[296] Wang, B., Hu, E., Tu, Z., David, K. D., Hu, K., Hu, X., Yang, W., Guo, J., Cai, W., Qian, W., and Zhang, H., 2018, "Characterization and Tribological Properties of Rice Husk Carbon Nanoparticles Co-Doped with Sulfur and Nitrogen," Appl. Surf. Sci., **462**, pp. 944–954.

[297] Zhang, G., Xu, Y., Xiang, X., Zheng, G., Zeng, X., Li, Z., Ren, T., and Zhang, Y., 2018, "Tribological Performances of Highly Dispersed Graphene Oxide Derivatives in Vegetable Oil," Tribol. Int., **126**, pp. 39–48.

[298] Wang, L., Wang, B., Wang, X., and Liu, W., 2007, "Tribological Investigation of CaF2 Nanocrystals as Grease Additives," Tribol. Int., **40**(7), pp. 1179–1185.

[299] Chen, Y., Wang, X., Clearfield, A., and Liang, H., 2018, "Anti-Galling Effects of α-Zirconium Phosphate Nanoparticles as Grease Additives," J. Tribol., **141**(3), pp. 031801-031801–6.

[300] Dai, W., Kheireddin, B., Gao, H., Kan, Y., Clearfield, A., and Liang, H., 2016, "Formation of Anti-Wear Tribofilms via α-ZrP Nanoplatelet as Lubricant Additives," Lubricants, **4**(3), p. 28.

[301] He, X., Xiao, H., Choi, H., Díaz, A., Mosby, B., Clearfield, A., and Liang, H., 2014, "α-Zirconium Phosphate Nanoplatelets as Lubricant Additives," Colloids Surf. Physicochem. Eng. Asp., **452**, pp. 32–38.

[302] Zhang, R., Xiong, L., Pu, J., Lu, Z., Zhang, G., and He, Z., 2019, "Interface-Sliding-Induced Graphene Quantum Dots Transferring to Fullerene-Like Quantum Dots and Their Extraordinary Tribological Behavior," Adv. Mater. Interfaces, **6**(24), p. 1901386.

[303] Liu, W., and Chen, S., 2000, "An Investigation of the Tribological Behaviour of Surface-Modified ZnS Nanoparticles in Liquid Paraffin," Wear, **238**(2), pp. 120–124.

[304] Berman, D., Mutyala, K. C., Srinivasan, S., Sankaranarayanan, S. K. R. S., Erdemir, A., Shevchenko, E. V., and Sumant, A. V., 2019, "Iron-Nanoparticle Driven Tribochemistry Leading to Superlubric Sliding Interfaces," Adv. Mater. Interfaces, **6**(23), p. 1901416.

[305] Berman, D., Narayanan, B., Cherukara, M. J., Sankaranarayanan, S. K. R. S., Erdemir, A., Zinovev, A., and Sumant, A. V., 2018, "Operando Tribochemical Formation of Onion-like-Carbon Leads to Macroscale Superlubricity," Nat. Commun., **9**(1), p. 1164.

[306] Berman, D., Deshmukh, S. A., Sankaranarayanan, S. K., Erdemir, A., and Sumant, A. V., 2015, "Macroscale Superlubricity Enabled by Graphene Nanoscroll Formation," Science, **348**(6239), pp. 1118–1122.

[307] Wang, X., 2016, "Engineered 2D Nanoplates for Pickering Emulsification and Functional Materials."

[308] Wang, X., Zeng, M., Yu, Y.-H., Wang, H., Mannan, M. S., and Cheng, Z., 2017, "Thermosensitive ZrP-PNIPAM Pickering Emulsifier and the Controlled-Release Behavior," ACS Appl. Mater. Interfaces, **9**(8), pp. 7852–7858.

[309] Horsley, S. E., Nowell, D. V., and Stewart, D. T., 1974, "The Infrared and Raman Spectra of α-Zirconium Phosphate," Spectrochim. Acta Part Mol. Spectrosc., **30**(2), pp. 535–541.

[310] Orendorff, C. J., Ducey, M. W., and Pemberton, J. E., 2002, "Quantitative Correlation of Raman Spectral Indicators in Determining Conformational Order in Alkyl Chains," J. Phys. Chem. A, **106**(30), pp. 6991–6998.

[311] Busca, G., Lorenzelli, V., Galli, P., Ginestra, A. L., and Patrono, P., 1987, "A Fourier-Transform Infrared and Catalytic Study of the Evolution of the Surface Acidity of Zirconium Phosphate Following Heat Treatment," J. Chem. Soc. Faraday Trans. 1 Phys. Chem. Condens. Phases, **83**(3), pp. 853–864.

[312] Ali, A. A. M., and Zaki, M. I., 2002, "HT-XRD, IR and Raman Characterization Studies of Metastable Phases Emerging in the Thermal Genesis Course of Monoclinic Zirconia via Amorphous Zirconium Hydroxide: Impacts of Sulfate and Phosphate Additives," Thermochim. Acta, **387**(1), pp. 29–38.

[313] Mekhemer, G. A. H., 1998, "Characterization of Phosphated Zirconia by XRD, Raman and IR Spectroscopy," Colloids Surf. Physicochem. Eng. Asp., **141**(2), pp. 227–235.

[314] Willermet, P. A., Dailey, D. P., Carter, R. O., Schmitz, P. J., and Zhu, W., 1995, “Mechanism of Formation of Antiwear Films from Zinc Dialkyldithiophosphates,” Tribol. Int., **28**(3), pp. 177–187.

[315] Guo, W., Zhou, Y., Sang, X., Leonard, D. N., Qu, J., and Poplawsky, J. D., 2017, “Atom Probe Tomography Unveils Formation Mechanisms of Wear-Protective Tribofilms by ZDDP, Ionic Liquid, and Their Combination,” ACS Appl. Mater. Interfaces, **9**(27), pp. 23152–23163.

[316] Costantino, U., and La Ginestra, A., 1982, “On the Existence of Pyrophosphates of Tetravalent Metals Having a Layered Structure,” Thermochim. Acta, **58**(2), pp. 179–189.

[317] Wang, X., Zhao, D., Nava Medina, I. B., Diaz, A., Wang, H., Clearfield, A., Sam Mannan, M., and Cheng, Z., 2016, “Surface Modification of Layered Zirconium Phosphate with PNIPAM,” Chem. Commun., **52**(26), pp. 4832–4835.

[318] Sun, L., J. Boo, W., Sue, H.-J., and Clearfield, A., 2007, “Preparation of α-Zirconium Phosphate Nanoplatelets with Wide Variations in Aspect Ratios,” New J. Chem., **31**(1), pp. 39–43.

[319] Saller, G., and Aigner, H., 2004, “High Nitrogen Alloyed Steels for Nonmagnetic Drill Collars. Standard Steel Grades and Latest Developments,” Mater. Manuf. Process., **19**(1), pp. 41–49.

[320] Zamani, S. M., Hassanzadeh-Tabrizi, S. A., and Sharifi, H., 2016, “Failure Analysis of Drill Pipe: A Review,” Eng. Fail. Anal., **59**, pp. 605–623.

[321] Zia-Ebrahimi, F., and Krauss, G., 1984, “Mechanisms of Tempered Martensite Embrittlement in Medium-Carbon Steels,” Acta Metall., **32**(10), pp. 1767–1778.

[322] Troup, J. M., and Clearfield, A., 1977, “Mechanism of Ion Exchange in Zirconium Phosphates. 20. Refinement of the Crystal Structure of .Alpha.-Zirconium Phosphate,” Inorg. Chem., **16**(12), pp. 3311–3314.

[323] Harsha, A. P., Limaye, P. K., Tyagi, R., and Gupta, A., 2016, “Effect of Temperature on Galling Behavior of SS 316, 316 L and 416 Under Self-Mated Condition,” J. Mater. Eng. Perform., **25**(11), pp. 4980–4987.

[324] Li, H., Wang, X., Chen, Y., and Cheng, Z., 2014, “Temperature-Dependent Isotropic-to-Nematic Transition of Charged Nanoplates,” Phys. Rev. E, **90**(2), p. 020504.

[325] Dai, W., Chen, Y., Lee, K., Sinyukov, A. M., Alkahtani, M., Hemmer, P. R., and Liang, H., 2017, “In Situ Investigation of the Growth of a Tribofilm Consisting of NaYF4 Fluorescent Nanoparticles,” Tribol. Trans., pp. 1–10.

[326] Dai, W., Lee, K., Sinyukov, A. M., and Liang, H., 2017, “Effects of Vanadium Oxide Nanoparticles on Friction and Wear Reduction,” J. Tribol., **139**(6), p. 061607.

[327] Xiao, H., Dai, W., Kan, Y., Clearfield, A., and Liang, H., 2015, “Amine-Intercalated α-Zirconium Phosphates as Lubricant Additives,” Appl. Surf. Sci., **329**(Supplement C), pp. 384–389.

[328] Clearfield, A., and Smith, S. D., 1968, “The Crystal Structure of Zirconium Phosphate and the Mechanism of Its Ion Exchange Behavior,” J. Colloid Interface Sci., **28**(2), pp. 325–330.

[329] Yeni, Y. N., and Fyhrie, D. P., 2003, "A Rate-Dependent Microcrack-Bridging Model That Can Explain the Strain Rate Dependency of Cortical Bone Apparent Yield Strength," J. Biomech., **36**(9), pp. 1343–1353.

[330] Chen, Y., Sanchez, C., Yue, Y., González, J. M., Parkinson, D. Y., and Liang, H., 2016, "Observation of Two-Dimensional Yttrium Oxide Nanoparticles in Mealworm Beetles (Tenebrio Molitor)," J. Synchrotron Radiat., **23**(5), pp. 1197–1201.

[331] Chen, Y., Sanchez, C., Yue, Y., de Almeida, M., González, J. M., Parkinson, D. Y., and Liang, H., 2016, "Observation of Yttrium Oxide Nanoparticles in Cabbage (Brassica Oleracea) through Dual Energy K-Edge Subtraction Imaging," J. Nanobiotechnology, **14**(1), p. 23.

[332] Chen, Y., Sanchez, C., Parkinson, D. Y., and Liang, H., 2016, "Direct Observation of Lubricant Additives Using Tomography Techniques," Appl. Phys. Lett., **109**(4), p. 041603.

[333] Hasegawa, M., Akiho, Y., and Kanda, Y., "Mechanochemical Polymerization of Methyl Methacrylate Initiated by the Grinding of Inorganic Compounds," J. Appl. Polym. Sci., **55**(2), pp. 297–304.

[334] Hasegawa, M., Kimata, M., and Kobayashi, S.-I., "Mechanochemical Copolymerization of Methyl Methacrylate and Styrene Initiated by the Grinding of Quartz," J. Appl. Polym. Sci., **84**(11), pp. 2011–2017.

[335] Craig, S. L., 2012, "Mechanochemistry: A Tour of Force," Nature, **487**(7406), pp. 176–177.